UNIVERSIDADE FEDERAL DE SÃO CARLOS
CENTRO DE CIÊNCIAS EXATAS E DE TECNOLOGIA
DEPARTAMENTO DE QUÍMICA
PROGRAMA DE PÓS-GRADUAÇÃO EM QUÍMICA

"CONTRIBUTION OF HOMOGENEOUS AND HETEROGENEOUS PROCESSES TO THE ACTIVATION OF PEROXYMONOSULFATE USING COBALT MAGNETIC FERRITE"

Yoisel Bueno Broterson*

Thesis presented as part of the requirements to obtain the title of DOCTOR IN SCIENCES, concentration area: CHEMISTRY

Advisor: Prof. Dr. José Mario de Aquino

*** Scholarship Holder of CAPES *(Coordination of Superior Level Staff Improvement)***

São Carlos - SP

2024

UNIVERSIDADE FEDERAL DE SÃO CARLOS

Centro de Ciências Exatas e de Tecnologia
Programa de Pós-Graduação em Química

Folha de Aprovação

Defesa de Tese de Doutorado do candidato Yoisel Bueno Broterson, realizada em 29/04/2024.

Comissão Julgadora:

Prof. Dr. José Mario de Aquino (UFSCar)

Profa. Dra. Fernanda de Lourdes Souza (IQSC/USP)

Prof. Dr. Diogo Paschoalini Volanti (UNESP)

Profa. Dra. Elaine Cristina Paris (EMBRAPA)

Prof. Dr. Francisco Guilherme Esteves Nogueira (UFSCar)

O Relatório de Defesa assinado pelos membros da Comissão Julgadora encontra-se arquivado junto ao Programa de Pós-Graduação em Química.

“Hacer es la mejor manera de decir”

José Martí

To my lovely family

ACKNOWLEDGMENTS

Firstly, I would like to thank my family, especially my mother Maritza, my sister Yarisel, and my late uncle Roberto (RIP). ***THANK YOU VERY MUCH*** for your unconditional support throughout these years and for being present in my life.

To GOD, for his blessings and for teaching me the way to move forward against all adversities, giving me peace, patience, health and strength to achieve this goal.

I want to thank Katia, for her patience, affection, and for being with me at this stage of my life.

I would also like to express my gratitude to my advisor, Professor José Mario de Aquino, for the opportunity he gave me to develop this research and also for his support, patience, contributions and dedication throughout these four years of studies.

Furthermore, I would like to thank all my friends at UFSCar, especially Yeison for his support and friendship, and the professors and colleagues at the Laboratório de Pesquisas em Eletroquímica (LaPE).

Finally, my sincere thanks to the ***Coordenação de Aperfeiçoamento de Pessoal de Nível Superior – CAPES,*** which provided the scholarship for my PhD study at UFSCar. I also express my gratitude to the following Brazilian funding agencies for their financial support: ***Conselho Nacional de Desenvolvimento Científico e Tecnológico – CNPq, Fundação de Amparo à Pesquisa do Estado de São Paulo – FAPESP, and Financiadora de Estudos e Projetos – Finep.***

MUITO OBRIGADO!!!

LIST OF ABBREVIATIONS

AsP – As-prepared samples without *in situ* chemical activation using oxidizer

Cpt 400 ºC/1 h – $CoFe_2O_4$ magnetic ferrite prepared by the co-precipitation method and thermally treated at 400 ºC for 1 h

Cpt 700 ºC/1 h – $CoFe_2O_4$ magnetic ferrite prepared by the co-precipitation method and thermally treated at 700 ºC for 1 h

CMF: cobalt magnetic ferrite

DMPO – 5,5-dimethyl-1-pyrroline *N*-oxide

ESR – electron spin resonance

EI – electrochemical impedance

HRTEM – high-resolution transmission electron microscopy

$HO^{\bullet}$ – hydroxyl radical

HPLC – high-performance liquid chromatography

ICP-OES – inductively coupled plasma optical emission spectrometry

IMD – Imidacloprid insecticide

IMD fraction – $100\times[IMD]_t/[IMD]_0$: [IMD] concentration at a specific time (t) and $t = 0$

ISCO – *in situ* chemical activation

MS/MS – tandem mass spectrometry

$^1O_2$ – singlet oxygen

PDS – peroxydisulfate

PMS – peroxymonosulfate

$SO_4^{\bullet-}$ – sulfate radical

SG 400 ºC/1 h – $CoFe_2O_4$ magnetic ferrite prepared by the sol-gel method and thermally treated at 400 ºC for 1 h

SG700 ºC/1 h – $CoFe_2O_4$ magnetic ferrite prepared by the sol-gel method and thermally treated at 700 ºC for 1 h

UHPLC-QToF MS – ultra-high performance liquid chromatography coupled to a time-of-flight mass analyzer

Us – Assayed samples for the *in situ* chemical activation of PMS to oxidize IMD

XRD – X-ray diffraction

XPS – X-ray photoelectron spectroscopy

LIST OF TABLES

LIST OF FIGURES

RESUMO

CONTRIBUIÇÃO DOS PROCESSOS HOMOGÊNEO E HETEROGÊNEO PARA A ATIVAÇÃO DO PEROXIMONOSULFATO UTILIZANDO FERRITA MAGNÉTICA DE COBALTO – O processo catalítico (c-POA), que utiliza óxidos metálicos (ou outro tipo de material) para a ativação de vários oxidantes como peróxido de hidrogênio (H_2O_2), peroxidisulfato (PDS, $S_2O_8^{2-}$) e peroximonosulfato (PMS, HSO_5^-), entre outros, constitui um dos processos oxidativos avançados (POA) que pode ser usado para o tratamento efetivo de águas superficiais e de abastecimento contaminadas por compostos orgânicos sintéticos. Particularmente, as ferritas magnéticas possuem a vantagem de serem reutilizadas e separadas com facilidade do meio reacional. Contudo, há uma grande lacuna na literatura no que se refere à participação/atuação dos íons lixiviados daqueles óxidos metálicos no processo de ativação dos oxidantes, bem como o estudo das modificações superficiais que ocorrem nos óxidos após serem utilizados. Desse modo, o objetivo do presente trabalho foi desvendar o papel da ferrita magnética de cobalto ($CoFe_2O_4$), e íons Co(II) adicionados à mistura de reação, na oxidação química *in situ* (ISCO da sigla em inglês) do inseticida imidacloprida (IMD) utilizando peroximonosulfato (PMS), bem como os efeitos superficiais na ferrita e decorrentes do processo ISCO. Para tanto, efetuou-se a síntese da $CoFe_2O_4$ por meio dos métodos sol-gel (SG) e coprecipitação (Cpt), seguida de sua calcinação em mufla (400 ºC e 700 ºC) por 1 h, e os materiais obtidos foram caraterizados como preparados (CP) e, após utilização nos ensaios de degradação do poluente (Us). A aplicação da $CoFe_2O_4$ para a ativação *in situ* do PMS envolveu o estudo da concentração do catalisador e do PMS, efeito do tampão fosfato e do pH, bem como de distintas matrizes aquosas. Com base nos resultados obtidos, baixas concentrações de $CoFe_2O_4$ (0.125 g L^{-1}) e de PMS (500 µmol L^{-1}) são suficientes para a completa oxidação da IMD. Além disso, constatou-se que pequenas concentrações (da ordem de µg L^{-1}) do íon Co(II) são suficientes para oxidar totalmente a IMD, corrigindo e monitorando-se o pH do meio reacional, o que auxiliou na explicação do porquê todos os materiais sintetizados conduzirem às mesmas taxas de oxidação da IMD. Algumas tentativas de se evitar a lixiviação de íons Co(II) foram conduzidas, porém, não foram bem sucedidas. Análises por cromatografia líquida acoplada à espectrometria de massas possibilitaram a identificação de apenas 5 intermediários, partindo-se da IMD, cujas principais modificações estruturais foram decorrentes de rupturas no anel imidazolidínico e/ou hidroxilações sucessivas. Como esperado, as principais espécies reativas de oxigênio identificadas foram os radicais hidroxila ($HO^{\bullet}$) e sulfato ($SO_4^{\bullet-}$), bem como a espécie não radicalar oxigênio singleto ($^1O_2$). As últimas espécies levaram a altos níveis de oxidação do IMD, mesmo em uma matriz aquosa complexa, como águas residuais municipais simuladas, às custas de uma diminuição de uma ordem de grandeza na taxa de oxidação do IMD. Finalmente, foi proposta uma rota de ativação do PMS pelo sólido e íons Co(II) com base nos materiais ensaiados e dados obtidos.

Palavras-chave: Processo de oxidação avançado; lixiviação de íons Co(II); catálise heterogênea; contaminantes emergentes; radicais hidroxila; processo homogêneo

ABSTRACT

CONTRIBUTION OF HOMOGENEOUS AND HETEROGENEOUS PROCESSES TO THE ACTIVATION OF PEROXYMONOSULFATE USING COBALT MAGNETIC FERRITE – The catalytic process (*c*-AOP), which utilizes metal oxides (or another type of material) to activate various oxidants such as hydrogen peroxide (H_2O_2), peroxydisulfate (PDS, $S_2O_8^{2-}$), and peroxymonosulfate (PMS, HSO_5^-), among others, constitutes one of the advanced oxidative processes (AOP) that can effectively treat surface and supply waters contaminated by synthetic organic compounds. In particular, magnetic ferrites have the advantage of being reusable and easily separated from the reaction medium. However, there is a significant gap in the literature regarding the participation/action of ions leached from those metal oxides in the oxidant activation process, as well as the study of the surface modifications that occur in the oxides after use. Therefore, the objective of the present work was to elucidate the role of cobalt magnetic ferrite ($CoFe_2O_4$), and Co(II) ions added to the reaction mixture, in the *in situ* chemical oxidation (ISCO) of the insecticide imidacloprid (IMD) using peroxymonosulfate (PMS), as well as the surface effects on ferrite resulting from the ISCO process. For this purpose, $CoFe_2O_4$ was synthesized using the sol-gel (SG) and co-precipitation (Cpt) methods, followed by calcination in a muffle furnace (400 ºC and 700 ºC) for 1 h, and the materials obtained were characterized as-prepared (AsP) and, after use in the pollutant degradation tests (Us). The application of $CoFe_2O_4$ for the *in situ* activation of PMS involved studying the catalyst dosage and PMS concentration, the effect of phosphate buffer and pH, as well as different aqueous matrices. Based on the results obtained, low concentrations of $CoFe_2O_4$ (0.125 g L^{-1}) and PMS (500 µmol L^{-1}) are sufficient for the complete oxidation of IMD. Furthermore, it was observed that even small concentrations (in the order of µg L^{-1}) of the Co(II) ion also resulted in the complete oxidation of the pollutant, with pH correction and monitoring of the reaction medium contributing to this process. This finding contributes to the understanding of why all synthesized materials exhibit similar rates of IMD oxidation. Some attempts to prevent the leaching of Co(II) ions were carried out; however, they were not successful. Analysis by liquid chromatography coupled to mass spectrometry allowed the identification of only 5 intermediates, starting from IMD, whose main structural modifications were due to ruptures in the imidazolidine ring and/or successive hydroxylation reactions. As expected, the main reactive oxygen species identified were hydroxyl ($HO^{\bullet}$) and sulfate ($SO_4^{\bullet-}$) radicals, and the non-radical singlet oxygen ($^1O_2$). The latter species led to high levels of IMD oxidation, even in a complex aqueous matrix such as simulated municipal wastewater (SMWW), albeit with an order of magnitude decrease in the rate of IMD oxidation. Finally, a mechanism for PMS activation by solid and Co(II) ions was proposed based on the materials tested and data obtained.

Keywords: Advanced oxidation process; Co(II) ion leaching; heterogeneous catalysis; emerging contaminants; hydroxyl radicals; homogeneous process

SUMMARY

PREAMBLE

This Doctoral Thesis is an adaptation of the article published: **"$CoFe_2O_4$ as a source of Co(II) ions for imidacloprid insecticide oxidation using peroxymonosulfate: Influence of process parameters and surface changes"** by **Yoisel B. Broterson**, Yeison Núnez-de la Rosa, Luis Guillermo Cuadrado Durango, Moacir Rossi Forim, Peter Hammer and José M. Aquino.

Available in: Chemosphere 352 (2024), 141278.

DOI: https://doi.org/10.1016/j.chemosphere.2024.141278

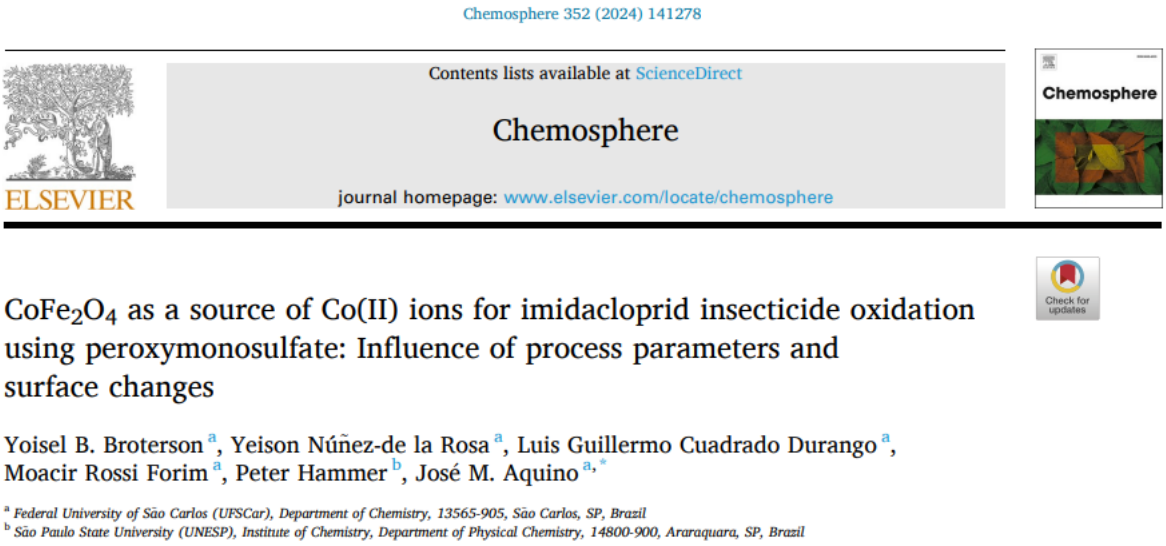

Chemosphere 352 (2024) 141278

Contents lists available at ScienceDirect

Chemosphere

journal homepage: www.elsevier.com/locate/chemosphere

$CoFe_2O_4$ as a source of Co(II) ions for imidacloprid insecticide oxidation using peroxymonosulfate: Influence of process parameters and surface changes

Yoisel B. Broterson [a], Yeison Núñez-de la Rosa [a], Luis Guillermo Cuadrado Durango [a], Moacir Rossi Forim [a], Peter Hammer [b], José M. Aquino [a,*]

[a] Federal University of São Carlos (UFSCar), Department of Chemistry, 13565-905, São Carlos, SP, Brazil
[b] São Paulo State University (UNESP), Institute of Chemistry, Department of Physical Chemistry, 14800-900, Araraquara, SP, Brazil

1. INTRODUCTION

Currently, large quantities of products are being produced and consumed around the world to improve human quality of life. The residues of these products often find their way into the environment through various routes and are not degraded by natural microorganisms due to their non-biodegradable nature. As a result, they contaminate surface and underground waters. This situation has become a global problem for modern society, given the scarcity of natural resources and the growing demand from the population.

Industrial activity, including mining, food processing, textile and tanning industries, as well as paper and cellulose production, constitutes the primary cause of water pollution. However, other sources of contamination such as agriculture, inadequate drinking water supply, and the absence or substandard quality of sewage and industrial effluent treatment facilities also contribute significantly.

In recent years, studies on water contamination have garnered increasing attention, as evidenced by the number of articles published between 2014 and 2023. According to data from the *Web of Science database*, the number of papers focusing on this theme (keyword: *water pollution*) has surged from 4,130 articles in 2014 to over 12,400 in 2023, totaling approximately 84,200 articles over the entire period, as shown in Figure 1.1. These results underscore the significant interest of the international scientific community in addressing this issue, which profoundly impacts the health of living organisms and marine ecosystems.

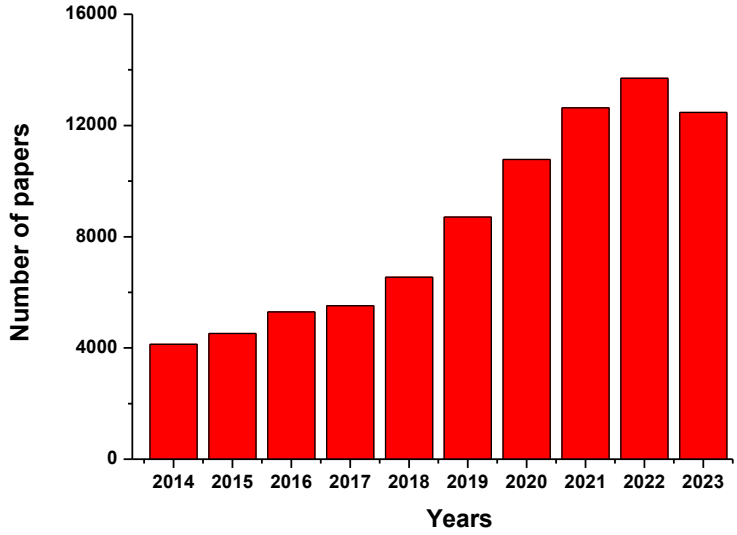

FIGURE 1.1 Number of articles published in the *Web of Science database* (keyword: *water pollution*) between 2014 and 2023. Accessed on 01/23/2024.

A report by the World Health Organization (*Drinking-water*) [1] revealed that in 2022, approximately 27% of the world's population lacked access to basic quality drinking water services, adversely affecting the health and economies of these countries. It is estimated that each year, approximately 505,000 deaths occur globally due to diarrhea and other preventable diseases such as cholera, dysentery, and typhoid, caused by consuming contaminated water, particularly in regions with lower levels of socioeconomic development.

Furthermore, data from the United Nations (*World Population Prospects 2022*) [2] indicated that the global population reached 8.00 billion in 2022, with projections suggesting an increase to 9.70 billion by 2050 due to rapid population growth. This trend is expected to lead to higher levels of production and consumption of raw materials, products, and services to meet growing needs. Consequently, there will be an increase in the generation of organic contaminants in the environment, particularly in water bodies worldwide.

Many of these compounds are classified as emerging pollutants [3], which refer to natural or man-made chemicals or materials that are not commonly

monitored but have been detected in water bodies at very low concentrations (nanograms or micrograms per liter). These pollutants possess toxicity or persistence characteristics that can significantly impact the metabolism of humans or aquatic animals [4-5]. Examples of emerging pollutants include pesticides, pharmaceutical and personal care products, hormones, textile dyes, illicit drugs, perfluorinated compounds, nanomaterials, and microplastics, among others [6-8].

Numerous emerging pollutants have been detected in various matrices and regions across the planet, as detailed in Table 1.1:

TABLE 1.1 Distribution of some emerging pollutants on the planet.

Reference	Emerging Pollutants	Matrix	Country	Geografical Area
[9]	Microplastics	Wastewater	Uruguay	South America
[10]		WWTP samples	USA	North America
[11]	20 types of pharmaceutical products.	Drinking water	Germany	Europe
[12]	26 active pharmaceutical components (APIs) and/or their metabolites.	Surface waters	USA	North America
[13]	33 pharmaceutical and personal care products (PPCPs) and 4 pesticides.	Ground water	Korea	Asia
[14]	14 pharmaceutical products and illicit drugs.	Wastewater	South Africa	Africa
[15]	A total of 102 pollutants were detected in water, 67 in sediment and 35 in fish tissue.	Surface water, lake sediments and fish.	USA	North America
[16]	58 compounds (14 pharmaceuticals and personal care products, 10 illicit drugs, 8 industrial compounds, 9 hormones and 17 pesticides.	Raw and treated sewage, surface and ground waters and drinking water.	Brazil	South America
[17]	15 pharmaceuticals and 25 pesticides.	Surface water	Brazil	South America

Microplastics represent a novel type of emerging contaminant that currently requires global investigation and monitoring due to the limited understanding of their distribution and environmental effects. In this context, Sierra *et al.*, [9] and Conley *et al.*, [10] detected various types of microplastics in wastewater samples, with concentrations ranging from 5.3 to 8.2×10^3 items per m^3 in Montevideo, Uruguay, and from 1 to 30 particles per liter in wastewater treatment plant (WWTP) samples in the United States, respectively. Sierra *et al.*, [9] identified cellulose fibers and various polymers such as polyethylene (PE), polypropylene (PP), polyethylene terephthalate (PET), and polyvinyl chloride (PVC) in their samples, with sizes ranging from 70 to 600 μm. However, Conley *et al.*, [10] found microplastics with smaller dimensions (20 to 300 μm), classified as fibers and particles in WWTP samples, demonstrating the high levels of removal efficiency in US effluent treatment plants (over 85%).

Houtman *et al.*, [11] demonstrated the presence of various pharmaceutical products in three drinking water production plants in Germany. Despite being detected at low concentrations (around 25 ng L^{-1}), the identified medications included stimulants, antidiuretics, antibiotics, analgesics, and antidepressants. Moreover, pharmaceuticals products and other pollutants such as hormones, industrial resides, illicit drugs, pesticides and personal care products, were found (with concentrations ranging from ng L^{-1} to mg L^{-1}) in various aqueous matrices, mainly surface waters and wastewater in other parts of the world. This was evidenced in the studies by Schwab *et al.*, [12]; Lee *et al.*, [13]; Archer *et al.*, [14] and Deere *et al.*, [15]. These findings indicate that water bodies are often contaminated not only by individual types of pollutants but also by a combination of various contaminants, potentially exacerbating the adverse effects on human health and the environment.

Brazil shares similarities with other countries worldwide, as it also faces a significant presence of emerging pollutants detected in various water bodies, as evidenced by studies conducted in different regions [16,17]. Montagner

et al., [16] identified 58 compounds, including pharmaceutical and personal care products, illicit drugs, hormones, pesticides, and other industrial products, with concentrations ranging from 10 to 10,000 ng L^{-1}, in surface and groundwater, drinking water, and untreated and treated wastewater from several cities in São Paulo state. The most frequently detected compounds were caffeine, bisphenol A, carbendazim, estrone, 17α-ethynylestradiol, 17β-estradiol, malathion, paracetamol, diclofenac, imidacloprid, and atrazine. The low levels of removal efficiency of effluent treatment processes (often below 50%) or direct discharge of untreated wastewater into surface water were identified as possible causes for their presence.

Perin *et al.*, [17] arrived at a similar conclusion, detecting 25 pesticides and 15 pharmaceuticals (with concentrations ranging from 6 to 580 ng L^{-1}), and various inorganic contaminants in water samples collected from Lake Guaíba in Rio Grande do Sul state. Pharmaceuticals detected included β-lactams, antibiotics, β-blockers, anesthetics, and non-steroidal anti-inflammatories, while the pesticides atrazine and simazine were consistently present in all samples, reflecting their common use in soybean crops in the region. Most of these organic compounds pose a potential risk to aquatic life, particularly algae, invertebrates, and fish, underscoring the importance of implementing measures to reduce and prevent their presence. Therefore, comprehensive monitoring analyses are essential for identifying and quantifying the main contaminants in each region, taking into account their level of economic and social development.

On the other hand, many of these contaminating substances are not easily removed by conventional effluent treatment plants, as indicated by the research conducted by Blackbeard, Díaz-Garduño and Subedi [18-20]. Consequently, they become persistent organic pollutants (POPs), a matter of concern within the global scientific community. Ingestion of water contaminated by POPs can lead to various health problems [7, 21-22], and their presence can also cause significant harm to aquatic ecosystems due to their bioaccumulative

nature. In response to these concerns, environmental organizations and the general population have been exerting consistent pressure to adopt strategies aimed at reducing water body pollution and controlling the emission and/or elimination of POPs [23-24]. Improving the quality of drinking water and sanitation is essential for fostering a more sustainable and environmentally-friendly society, as reflected in the *Sustainable Development Goals* outlined by the United Nations [25].

In this scenario, Schwarzenbach *et al.*, [26], described the main scientific challenges associated with water pollution caused by organic compounds. These challenges include: *i)* assessing the impact of these pollutants on public health and the environment; *ii)* identifying effective treatment methods; and *iii)* minimizing contaminated effluents or developing environmentally-friendly production processes. Consequently, there is an urgent need to explore and implement new technologies, preferably sustainable ones, for the efficient treatment of effluents containing organic pollutants. In this context, the development of advanced oxidation processes (AOPs) presents a promising alternative solution.

AOPs comprise a series of processes that generate free radicals, primarily hydroxyl (HO•) radical, through different means to degrade organic pollutants. According to Miklos *et al.*, [27], AOPs are generally categorized into five groups: *i)* O_3-based; *ii)* UV-based (ultra-violet); *iii)* physical (*f*-AOPs); *iv)* electrochemical (*e*-AOPs); and *v)* catalytic (*c*-AOPs). Specifically, catalytic oxidative processes (*c*-AOPs), where reactive species are generated *in situ* from the catalytic decomposition of various oxidants (primarily hydrogen peroxide (H_2O_2), peroxymonosulfate (PMS, HSO_5^-) and peroxydisulfate (PDS, $S_2O_8^{2-}$)) in the presence of catalysts, have garnered significant interest in recent years due to their simplicity, ease of operation, and versatility [28].

Oxidants are activated by heterogeneous catalysis through electron transfer reactions with transition metal (or another species), resulting in the

homolytic cleavage of the peroxide bond (–O-O–) and, consequently, the formation of hydroxyl (HO•) or/and sulfate ($SO_4^{\bullet-}$) radicals, according the Eqs. 1 to 3:

$$M^{n+} + H_2O_2 \rightarrow M^{(n+1)+} + HO\bullet + OH^- \quad (1)$$

$$M^{n+} + HSO_5^- \rightarrow M^{(n+1)+} + SO_4^{\bullet-} + OH^- \quad (2)$$

$$M^{n+} + S_2O_8^{2-} \rightarrow M^{(n+1)+} + SO_4^{\bullet-} + SO_4^{2-} \quad (3)$$

Hydroxyl radicals possess a high oxidation potential ($E°$ = 2.72 V/SCE) and a short half-life (~20 ns) [29]. On the other hand, the sulfate radical, derived from the activation of persulfate compounds such as peroxymonosulfate (PMS, HSO_5^-) and peroxydisulfate (PDS, $S_2O_8^{2-}$) [30] (see Eqs. 2 and 3), exhibits a comparable oxidation potential ($E°$ = 2.44 V/SCE), a longer half-life ($t_{1/2}$ ~ 40 µs), and greater selectivity compared to the hydroxyl radical [29]. Furthermore, these radicals display different reactivities depending on the reaction medium; for instance, HO• radicals prevail under neutral to alkaline conditions, whereas $SO_4^{\bullet-}$ radicals are generally predominant under neutral to acidic conditions [31].

In particular, the activation of the PMS oxidant can generate not only the $SO_4^{\bullet-}$ radical (see Eq. 2), but also other highly reactive species such as the HO• radical and the non-radical singlet oxygen ($^1O_2$). The latter is produced as a result of the reaction of the $SO_5^{\bullet-}$ species with H_2O, as shown below in Eqs. 4 to 6 [30]:

$$M^{n+} + HSO_5^- \rightarrow M^{(n+1)+} + SO_4^{2-} + HO\bullet \quad (4)$$

$$M^{(n+1)+} + HSO_5^- \rightarrow M^{n+} + SO_5^{\bullet-} + H^+ \quad (5)$$

$$2SO_5^{\bullet-} + H_2O \rightarrow 2HSO_4^- + 1.5\ {}^1O_2 \quad (6)$$

Furthermore, the $^1O_2$ species can also be formed by the self-decomposition of the oxidant PMS in a predominantly basic medium, as described by Eq. 7. This occurs when the pH of the solution exceeds the second pK_a (9.4) value of PMS [32].

$$HSO_5^- + SO_5^{2-} \rightarrow HSO_4^- + SO_4^{2-} + {}^1O_2 \quad (7)$$

Although the singlet oxygen is a weaker oxidant compared to hydroxyl and sulfate radicals [30], this non-radical species exhibits greater selectivity than the other (HO• and $SO_4^{\bullet-}$) radicals. Singlet oxygen exclusively reacts with persistent organic pollutants (POPs), unaffected by the wide variety of interferents commonly present in real aqueous matrices such as inorganic ions (Cl^-, Br^-, I^-, CO_3^{2-}, HCO_3^-, $H_2PO_4^-$, HPO_4^{2-}, etc.) and dissolved organic matter, which comprises a complex mixture of humic acids and other organic compounds containing aliphatic, aromatic, and olefinic moieties [30]. This unique property of singlet oxygen makes it particularly valuable for environmental chemistry applications.

The generation of all these highly reactive species facilitates the degradation of several organic pollutants, resulting in the formation of byproducts with lower toxicity. In some cases, complete mineralization is achieved, leading to their conversion into CO_2, H_2O, NO_3^-, etc., as shown in Eq. 8:

$$\text{Pollutant} + SO_4^{\bullet-} + HO\bullet + {}^1O_2 \rightarrow \text{Byproducts} + CO_2 + H_2O \quad (8)$$

The most commonly utilized materials as catalysts for activating oxidants and effectively removing numerous organic pollutants include metals and their mixtures (such as Co, Cu, and Fe), metal oxides (primarily derived from Fe and Mn), and carbon-derived compounds, among others [33-37]. Particularly noteworthy is the use of magnetic ferrites, which are metallic oxides, often in conjunction with other materials, to effectively activate oxidants and generate both radical and non-radical species. This approach has remained relevant in the

literature, primarily due to its high oxidation rates and the ease of recovering solids (enabling water or treated effluent separation) for future reuse [38-40].

Kakavandi *et al.*, [38] synthesized a ferrite composite through the chemical precipitation of cobalt with carbon nanotubes to activate the oxidants H_2O_2, PMS, and PDS, in the presence or absence of ultraviolet light at 254 nm. They achieved complete oxidation of bisphenol A compound within 60 min of treatment, with a 70% mineralization rate. The authors suggested a high degree of synergism of the composite for pollutant degradation, although this claim was not well supported by the data presented in the study, particularly when comparing the sum of individual effect values with the experimental value obtained. Additionally, irradiation with UVC-type light results in high homolysis rates of the oxidants used.

Y. Li *et al.*, [39] investigated the effect of different compositions of cobalt ferrite (Co:Fe molar ratio equal to 1:16, 1:8, 1:4, 1:2, and 3:4 and via chemical precipitation synthesis) on the activation of the PMS oxidant across a wide pH range (3 to 11) for degrading the antibiotic sulfamethoxazole (SMX). Although varying molar proportions affected the crystallinity and morphology of the material, the $CoFe_2O_4$ compound (with a Co:Fe molar ratio of 1:2) yielded the best results, achieving approximately 90% SMX oxidation within 10 min. This compound effectively activated PMS and generated reactive species (HO•, $SO_4^{\bullet-}$ and $^1O_2$) regardless of the solution's pH. However, the authors did not provide an explanation for why varying stoichiometric proportions did not impact the percentage of SMX oxidation or PMS activation.

In both presented studies, the deleterious effect of the presence of inorganic ions on the oxidation rates of organic pollutants was observed. However, according to Y. Li *et al.*, [39], the effect of leached ions (Co(II) and Fe(III)) was not significant concerning SMX degradation or PMS activation. In this context, Fontecha-Cámara *et al.*, [40] investigated the effect of mixed Fe

oxides (specifically $CuFe_2O_4$, Fe_2O_3 and $FeTiO_3$, obtained commercially) on the oxidation and mineralization of gallic acid via activation of the H_2O_2 oxidant. Despite achieving complete oxidation and mineralization of gallic acid within 30 min of the experiment, the authors observed a significant leaching of Fe(III) and Cu(II) species into the solution, at a concentration of a few mg L^{-1}. Additionally, they noted that the effect produced on the oxidation and mineralization of the target compound, due to the presence of dissolved ions, was substantial. In other words, the effects of homogeneous and heterogeneous catalysis overlapped. According to the authors [40], the high leaching of the constituent ions of the compounds could be attributed to the pH of the medium, the type of pollutant treated, and the organic intermediates produced. These last two aspects are likely due to the complexation and stabilization of the metal ion in solution. Considering these factors, it would be beneficial to explore the effect of the type of metal ion in solution and the catalyst's synthesis method.

The catalytic effect of dissolved ions is indeed of paramount importance and has not received significant attention in the literature, as investigated by Anipsitakis and Dionysiou [41] for Co(II) species in solution. Their work revealed that extremely low concentrations of Co(II) in solution (in the range of mg L^{-1}) are sufficient for rapid oxidation (within 1 min) of 2,4-dichlorophenol via activation of the PMS oxidant in a buffered phosphate medium. On the other hand, several studies utilizing $CoFe_2O_4$ magnetic ferrite (CMF) reported a low contribution (in the μg L^{-1} range) of leached Co(II) ions to oxidize various emerging organic pollutants, as indicated in Table 1.2 for selected papers.

TABLE 1.2 Some reference papers that utilize $CoFe_2O_4$ and PMS, as oxidizer, to examine the concentration and role of Co(II) ions that have leached into the assayed solution.

Reference	Compound	Experimental conditions highlights	Co(II) ion leaching issue
[43]	Magnetic $CoFe_2O_4$ nanoparticles supported on titanate nanotubes ($CoFe_2O_4$/TNTs)	- Hydrothermal synthesis of TNTs. -$CoFe_2O_4$/TNTs composite synthesized by impregnation + calcination. - Rhodamine B and phenol; catalyst dosage: 10 mg to 21 mg; Oxone = 4 g L^{-1}	The composite led to significant reduction of Co(II) ion leaching (from 928 μg L^{-1} to 662 μg L^{-1}).
[44]	$CoFe_2O_4$@Graphene hybrid aerogels	- Hybrid aerogels synthesized by freeze-drying. - Flowing experiments: 25 to 100 mg L^{-1} organic (indigo carmine, methyl orange, orange II, malachite green, phenol and norfloxacin), PMS solution (0.2 – 0.6 g L^{-1}), flow rates of 60, 90, or 120 mL h^{-1}	All experimental conditions led to Co(II) ion leaching lower than 1 mg L^{-1}.
[42]	Co_3Fe_7–$CoFe_2O_4$ composite	- Salt precursor + 2-methylimidazole followed by pyrolysis under N_2 atmosphere. - 2,4-Dichlorophenol (2,4-DCP: 50 mg L^{-1}, 200 mL) + catalyst (0.05 g L^{-1}) + PMS (1.25 g L^{-1}) - Optimum pH: 7.7	The detected concentration of Co and Fe ions were 0.052 and 0.036 mg L^{-1}, respectively. Low 2,4-DCP oxidation (20% in 30 min) was reported for the homogeneous reaction.

TABLE 1.2 *(continuation)* Some reference papers that utilize $CoFe_2O_4$ and PMS, as oxidizer, to examine the concentration and role of Co(II) ions that have leached into the assayed solution.

Reference	Compound	Experimental conditions highlights	Co(II) ion leaching issue
[45]	Expanded graphite (EG) loaded with $CoFe_2O_4$	- Co-precipitation using salt precursors + EG (700 ºC/1 min) thermally treated at 400 ºC/2 h Sulfamethoxazole (SMX) at 10 mg L^{-1}: investigation of EG/$CoFe_2O_4$ mass ratio, catalyst dose (0 – 0.8 g L^{-1}), PMS concentration (0 – 0.4 mM), initial pH (3 – 11), SMX initial concentration (2.5 – 15 mg L^{-1}), and interfering ions (Cl^-, HCO_3^-, and HPO_4^{2-})	Co and Fe leaching equal to 0.129 mg L^{-1} and 0.025 mg L^{-1}, respectively, without investigation of homogeneous reactions.
[39]	$Co_xFe_{3-x}O_4$ with different molar ratios of Co:Fe (1:16, 1:8, 1:4, 1:2, and 3:4)	- Co-precipitation using salt precursors + heat treatment at 600 ºC/1 h - SMX (10 mg L^{-1}): investigation of catalyst dose (0.05, 0.1, and 0.2 g L^{-1}), PMS concentration (0.2, 0.4, 0.6, and 0.8 g L^{-1}), solution pH (3.0, 5.0, 7.0, 9.0, and 11.0), interfering ions (Cl^-, HCO_3^-, NO_3^-, and SO_4^{2-})	The Fe and Co concentration were 0.32 and 0.43 mg L^{-1}, respectively, after the 5th cycle. Only a small contribution from homogeneous reactions (17% – solution pH unknown) was observed. Co ion concentration also ranged from 0.2 to 0.7 mg L^{-1} depending on the solution pH.

TABLE 1.2 *(continuation)* Some reference papers that utilize $CoFe_2O_4$ and PMS, as oxidizer, to examine the concentration and role of Co(II) ions that have leached into the assayed solution.

Reference	Compound	Experimental conditions highlights	Co(II) ion leaching issue
[46]	$CoFe_2P_x$ synthesized by phosphorization of $CoFe_2O_4$	- Hydrothermal synthesis of $CoFe_2O_4$ followed by its low temperature phosphorization using NaH_2PO_2 - Sulphachloropyridazine sodium (SCP) as target pollutant: investigation of distinctly prepared compounds and oxidants, pH values, PMS concentration, and catalyst dosage.	The reported leached Co ions during the recycling test (5 cycles) were very low and equal to 0.082, 0.053, 0.027, 0.024, and 0.023 mg L^{-1}. No homogeneous experiments were carried out.
[47]	Core-shell Fe_2O_3@$CoFe_2O_4$ hybrids microspheres	- Ion exchange calcination method. - Phenol (10 mg L^{-1}) as target pollutant: investigation of catalyst dosage (5, 10, 20, 30 mg L^{-1}), PMS concentration (1, 2, 3, 4 mM), initial pH (3, 5, 7, 9), solution temperature (25, 35, 45, 55 ºC), and interfering ion (SO_4^{2-}, Cl^-)	The reported Co ion leached after the first cycle (during the recycling test) was 0.0198 mg L^{-1}. Further measurements were below the detection limit. No homogeneous experiment was carried out.

TABLE 1.2 *(continuation)* Some reference papers that utilize $CoFe_2O_4$ and PMS, as oxidizer, to examine the concentration and role of Co(II) ions that have leached into the assayed solution.

Reference	Compound	Experimental conditions highlights	Co(II) ion leaching issue
[48]	$CoFe_2O_4$ supported on three-dimensional graphene aerogels ($CoFe_2O_4$@3DG)	- Hydrothermal synthesis of $CoFe_2O_4$ from salt precursors and graphene oxide. - Benzotriazole (BTA: 100 mg L^{-1} for 100 mL): investigation of the $CoFe_2O_4$ composite ($CoFe_2O_4$@3DG, $CoFe_2O_4$@rGO, $CoFe_2O_4$, 3DG), pH (3, 5, 7, 9, 11), PMS concentration (4 – 16 mM)	The amount of Co ion leached ranged from 0.18 mg L^{-1} to 0.35 mg L^{-1} after the 7th cycle during the stability test of $CoFe_2O_4$@3DG.
[49]	CoFe bimetallic composite (CoFe@FS)	- Solvothermal synthesis of CoFe@FS. - Ciprofloxacin (100 mL at 10 mg L^{-1}): investigation of catalyst load (0.05, 0.1, 0.2, and 0.3 g L^{-1}), PMS concentration (1, 1.5, 2, 2.5 mM), initial CIP concentration (5, 10, 20, 50 mg L^{-1}), initial pH (2.99, 5.09, 7.02, 9.01), temperature (5, 15, 25, 35 ºC), inorganic (Cl^-, NO_3^-, SO_4^{2-} and HCO_3^-) and organic (humic acid) interferents.	Up to 0.7 mg L^{-1} of Co ions was detected. Homogeneous experiments were carried out, but led to a lower oxidation rate and level with respect to the CoFe@FS.

TABLE 1.2 *(continuation)* Some reference papers that utilize $CoFe_2O_4$ and PMS, as oxidizer, to examine the concentration and role of Co(II) ions that have leached into the assayed solution.

Reference	Compound	Experimental conditions highlights	Co(II) ion leaching issue
[50]	$CoFe_2O_4$ nanoparticles dispersed in an oil sludge carbon (OSC), previously activated – $CoFe_2O_4$/OSC	- Oil sludge activation mixed with Co and Fe salt precursor and followed by heat treatment. - Norfloxacin (30 µM) as target pollutant: investigation of initial pH (3.2, 4.5, 5.9, 7, 8.4), PMS concentration (0.2, 0.4, 0.6, 0.8, 1 mM), catalyst dosage (0.125, 0.25, 0.5, 1 g L^{-1}), temperature, and cycles of catalyst (10 experiments)	The amount of Co ion leaching increased with the recycling experiments (from ~10 µg L^{-1} to 50 µg L^{-1}). Acidic solutions also led to higher Co ion amounts. No homogeneous experiment was carried out.

As observed, the use of $CoFe_2O_4$ and other compounds derived from magnetic ferrites can indeed result in the liberation of significant amounts of metallic ions into the reaction mixture. However, since the catalytic effect of these species is often underestimated or misunderstood, an in-depth investigation is recommended to clarify this issue.

Considering the above, the objective of this Doctoral Thesis is to: ***investigate the contribution of homogeneous and heterogeneous processes, using a $CoFe_2O_4$ magnetic ferrite (CMF) and metal ions in low concentrations, for the activation of the PMS oxidant (HSO_5^-) and degradation of the insecticide imidacloprid (IMD)***. The primary hypothesis is to determine whether the solid oxide (CMF) is necessary or if the dissolved metal ions alone are sufficient to activate the PMS oxidant and degrade the organic contaminant IMD (see chemical formula in Figure 1.2). Addressing this question will provide valuable insights that may guide future research in the correct development of catalysts.

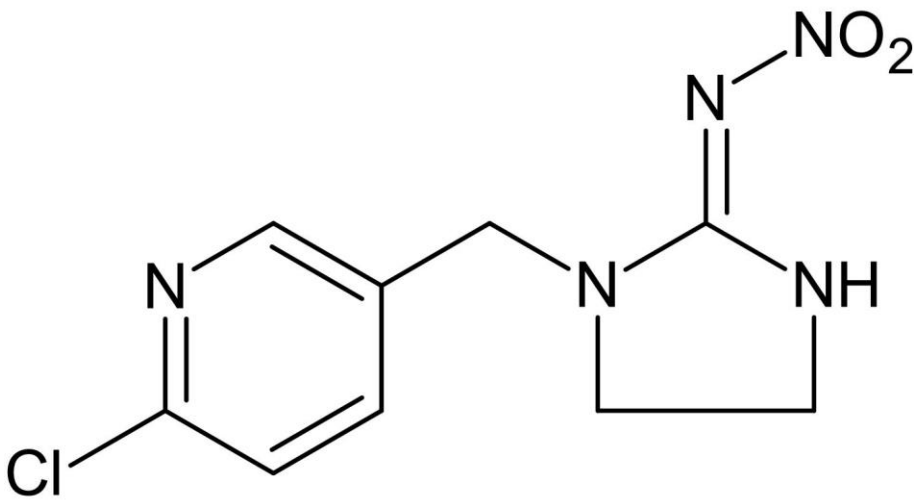

FIGURE 1.2 Chemical structure of imidacloprid (IMD) insecticide – $C_9H_{10}ClN_5O_2$ and MW: 255.6615486 g mol^{-1}.

Thus, $CoFe_2O_4$ nanoparticles were synthesized using the sol-gel (SG) and co-precipitation (Cpt) methods. The activation of PMS through homogeneous or heterogeneous processes were investigated with and without a buffer solution at neutral conditions (~ pH 7), employing different concentrations of $CoFe_2O_4$, Co(II) ions, and PMS to assess the structural and electrochemical changes occurring during the catalytic process (mainly on the solid material), including the effect of the CMF synthesis procedure. All materials were characterized for their morphology, crystalline structure, surface oxidation state, and electrochemical parameters. This characterization involved techniques such as high-resolution transmission electron microscopy (HRTEM), X-ray diffraction (XRD), Fourier transform infrared spectroscopy (FTIR), X-ray photoelectron spectroscopy (XPS), and electrochemical measurements, both before and after use in the IMD degradation experiments. The main organic intermediates and working oxidants were identified using liquid chromatography coupled to high-resolution mass spectrometry (UHPLC-QToF MS).

Further details about additional tests that were carried out, as well as the analytical techniques applied, will be described in the Materials and Methods section of this research work. Then, all obtained results and main conclusions will be discussed in the Results and Discussion and Conclusion sections, respectively.

The primary societal implication of this research is to elucidate the activation mechanism of the peroxymonosulfate oxidant. This process generates potent radicals capable of oxidizing organic pollutants frequently found in effluent streams.

2. MATERIALS AND METHODS

2.1 Chemical reagents

The chemical reagents, including IMD (Imidacloprid, Milenia Agrociencias S/A), $Fe(NO_3)_3•9H_2O$ and $Co(NO_3)_2•6H_2O$ (analytical grade reagent – a.r., Acros Organics), NaOH (a.r., Panreac), Ethanol (absolute grade, Sigma Aldrich), PVA (Polyvinylalcohol, a.r., available as Mowiol® 18-88, Sigma Aldrich), PVDF (polyvinylidene fluoride, a.r., Sigma Aldrich), K_2HPO_4 (a.r., Sigma Aldrich), H_2SO_4 (a.r., Merck), $Na_2S_2O_3•5H_2O$ (a.r., Synth), PMS (Potassium peroxymonosulfate, a.r., available as Oxone®, Sigma Aldrich), KI (a.r., Synth), $NaHCO_3$ (a.r., Sigma Aldrich), isopropyl alcohol (99.8%, Panreac), tert-butyl alcohol (99.7%, Neon), furfuryl alcohol (a.r., Sigma Aldrich), L-histidine (a.r., Sigma Aldrich), 9,10-anthracenediyl-bis(methylene) dimalonic acid (ABDA: a.r., CaymanChem), DMPO (5,5-dimethyl-1-pyrroline N-oxide, a.r., CaymanChem), HCOOH (a.r., J.T.Baker), $Na_2S_2O_3$ (a.r. Synth), CH_3OH (HPLC grade, JTBaker) were used as received without prior treatment. All solutions were prepared using deionized water (Millipore Milli-Q Direct-Q® 5 UV system, $r \geq 18.2$ MΩ cm).

2.2 Synthesis of $CoFe_2O_4$ magnetic ferrite (CMF) nanoparticles

$CoFe_2O_4$ nanoparticles were synthesized by the SG and Cpt methods as reported in literature (Srinivasa Rao *et al.*, [51]; Basak *et al.*, [52]). Briefly, in the first case, 0.5 g of polyvinyl alcohol (PVA) was dissolved in 100 mL of water at 90 °C, followed by the addition of precursor salts, $Co(NO_3)_2•6H_2O$ (0.01 mol) and $Fe(NO_3)_3•9H_2O$ (0.02 mol). After complete water evaporation, the resulting powder was collected and thermally treated in a muffle furnace (400 °C or 700 °C for 1 h at a heating rate of 20 °C min^{-1}) at air conditions. In the second case, the same amount of the precursor salts was dissolved in absolute ethanol under magnetic stirring, followed by the dropwise addition (32 mL) of a concentrated

NaOH solution (3 M). The resulting mixture was kept under constant stirring for 30 min under ambient conditions. Next, the resulting solid material was centrifuged and washed several times with absolute ethanol and deionized water (until the washing water reached pH 7) and finally dried at 60 °C for 24 h. After this step, heat treatment was carried out in a muffle, as described above.

2.3 CMF characterization

X-ray diffraction (XRD) experiments were performed using a D8 Advanced ECO instrument (Bruker) in the reflection mode (Cu-Kα_1 radiation of 1.54 Å, 40 kV, and 25 mA) at a scanning rate of 1° min^{-1} from 5° to 90° (2θ). High-resolution transmission electron microscopy (HRTEM) was used to analyze the surface morphology of particles using a TECNAI G^2 F20 (FEI) instrument.

The surface analysis of $CoFe_2O_4$ (nominal composition) was carried out by XPS using a commercial spectrometer K-alpha XPS (Thermo Scientific). The Al Ka line (*hn* = 1.486 eV) was used as the ionization source and the pass energy of the analyzer was set to 50 eV for the high-resolution spectra. Other parameters kept constant were spot size (300 μm), energy step size (0.10 eV), dwell time (50 ms), and number of scans (10). The inelastic background of the C 1s, O 1s, Co $2p_{3/2}$ and Fe $2p_{3/2}$ high-resolution spectra was subtracted using the Shirley method. The composition was determined by the relative proportions of the peak areas corrected by the Scofield's atomic sensitivity factors with an accuracy of ±10%. The deconvolution of the experimental spectra was performed using a Voigtian type function, with Gaussian (70%) and Lorentzian (30%) combinations. The width at half height varied between 1.0 and 2.0 eV and the position of the peaks was determined with an accuracy of ±0.1 eV with respect to the hydrocarbon peak located at 294.9 eV.

The surface functional groups were determined by using Fourier transform infrared spectroscopy (FTIR) measurements. Samples were analyzed

using the IR-Prestige 21 spectrometer (Shimadzu), operating from 4200 to 240 cm^{-1}.

Inductively coupled plasma optical emission spectrometry (ICP-OES) was carried out using a Thermo ICP OES iCAP 6000 (from Thermo Fischer Scientific). The instrumental parameters optimized during analyses are described in Table A1.

Electrochemical impedance (EI: ±10 mV perturbation, 5 kHz – 0.5 mHz) and open circuit potential measurements (OCP in presence or absence of PMS and/or IMD) were performed in 0.5 M Na_2SO_4 solution (at pH 7) at ambient conditions using a conventional three-electrode cell with a Pt foil and an Ag/AgCl (3 M KCl) as a counter and reference electrode, respectively. The working electrode was composed of a carbon paper substrate on which a slurry containing a mixture of $CoFe_2O_4$ (75% *m*/*m*) was placed. The slurry was prepared at different treatment times using 20% *m*/*m* Ketjen CB 600 (Nouryon) and 5% *m*/*m* PVDF was deposited by drop coating and left at 60 ºC for 12 h for solvent evaporation. The slurry was previously mashed in an agate mortar and dispersed in 500 μL of N-methyl pyrrolidone. All measurements were carried out in the dark.

The measurements were carried out for the as-prepared CMF samples (SG and Cpt) and after 2 h of treatment. For this purpose, the catalyst samples were collected, filtered, washed three times with deionized water, and dried under vacuum in a desiccator for at least 12 h.

2.4 IMD oxidation and analysis of treated solutions

The *in situ* chemical activation of PMS using CMF for the oxidation of IMD (50 mg L^{-1}) was carried out in a water jacket glass vessel (400 mL) under constant stirring in the dark. Firstly, 150 mL of a buffered solution (10 mM de KH_2PO_4 at pH 7) was added to the reaction vessel followed by the solid CMF. A neutral solution was chosen as previously reported by X. Li *et al.*, [53] and Zhou *et al.*, [42] (see Figure A1 for the evolution of the zeta potential values as a

function of the solution pH for the CMF sample). Then, the system was left under constant stirring for adsorption during 2 h. Subsequently, solid PMS was also added to start the oxidation reaction. The effect of different parameters such as the CMF dosage (0.125, 0.250, 0.500 and 1.0 g L^{-1}), PMS concentration (250, 500, and 1000 µM), synthesis method (SG and Cpt), and thermal treatment (400 ºC and 700 ºC) was studied. The solution pH was continuously monitored and manually adjusted by adding concentrated/diluted H_2SO_4 or NaOH solutions. Other operational variables, such as treatment time, solution temperature, and stirring were kept constant at 120 min, 25 °C, and 600 rpm, respectively. The samples were analyzed after being collected from the reaction mixture at predetermined time intervals, filtered through a 0.22 µm cellulose acetate cartridge, and quenched with excess $Na_2S_2O_3$ (1.0 M), except when residual oxidant was quantified. A recycling test (5 consecutive degradation experiments) was also carried out after optimization of the above conditions. For this purpose, after each run, the CMF catalyst was recovered by magnetic separation, washed thoroughly with deionized water, and dried under vacuum before further use.

After initial optimization using deionized water, tap water and a simulated municipal effluent wastewater (SMWW) were tested (see Table A2 and A3 and Text A1 for characterization and composition of such water matrices of the Appendix section) to assess the influence of common inorganic and organic interferences in real situations.

The evolution of the IMD concentration was monitored by high-performance liquid chromatography (HPLC, Shimadzu 20A) at 270 nm using a core-shell C-18 reversed-phase column as the stationary phase (150 mm × 4.6 mm i.d., 5 µm particle size, 100 Å pore size, from Phenomenex®). A mixture of aqueous 0.1% (*V/V*) formic acid (eluent A) and methanol (eluent B) was used as the mobile phase in a gradient elution mode (from 20% to 90% of B in 8 min and then, back to 20% after 2 min and keeping this condition for 2 min before further analyses). The flow rate, injection volume, and temperature of the column were

kept fixed at 1.0 mL min^{-1}, 25 µL, and 24 °C, respectively. When required, the amount of residual oxidant was determined using the spectrophotometric method adapted from the work of Liang *et al.*, [54].

Ultra-high performance liquid chromatography coupled to a time-of-flight mass analyzer (UHPLC-QToF MS) was used in the optimized conditions to analyze intermediates formed during the IMD oxidation process, according to a methodology described in Text A2 and Table A4. UHPLC-QToF MS and ESR analyses were also used to identify the main working oxidant species (mainly $HO^{\bullet}$) using a DMPO solution as spin probe. Experimental details can be seen in Text A3 in the Appendix.

Experiments in the presence of commonly known scavengers (0.1 M to assure complete reaction between radical/nonradical species with scavenger), such as isopropyl alcohol, tert-butyl alcohol, furfuryl alcohol, and L-histidine were used to assess the effect of $HO^{\bullet}$ and $SO_4^{\bullet-}$ radicals and $^1O_2$. To get further evidence on the role of $^1O_2$, PMS activation using $CoFe_2O_4$ and Co(II) in the presence of ABDA [55] was carried out, as described in Text A4. ABDA was considered to be a specific compound to react with $^1O_2$. Finally, the dissolved oxygen concentration was measured using a Visiferm DO type sensor.

The chromatographic procedures to determine carboxylic acids and inorganic ions can be seen in Text A5 of the Appendix section.

3. RESULTS AND DISCUSSION

3.1 Characterization of the as-prepared $CoFe_2O_4$ magnetic ferrite (CMF)

Figure 3.1 (a to d) shows TEM images of the as-prepared cobalt magnetic ferrite (CMF) material synthesized by SG and Cpt methods. The morphology of the nanoparticles exhibited a globular structure with many agglomerates for both synthesized conditions. As expected, the mean particle size was about 10 nm and larger than 20 nm of samples heat treated at 400 ºC and 700 ºC, respectively – see Figure A2 and Table A5 of histograms and mean particle sizes, respectively. The SG 700 ºC/1 h compound showed an unusual size (86 nm), which was larger than the mean size of the remaining conditions. The crystallinity of CMF nanoparticles was confirmed by HRTEM micrographs, as shown in Figure 3.2. The lattice fringe spacing was close to 4.7 Å (SG 700 ºC/1 h, Cpt 400 ºC/1 h, and Cpt 700 ºC/1 h samples) and 2.9 Å (SG 400 ºC/1 h), corresponding to the (111) and (022) diffraction planes of CMF, respectively. As demonstrated below, the lattice fringe spacing, which corresponds to the most pronounced diffraction peak at approximately 35º (attributable to the (113) plane), was not discernible in the transmission electron micrographs that were analyzed.

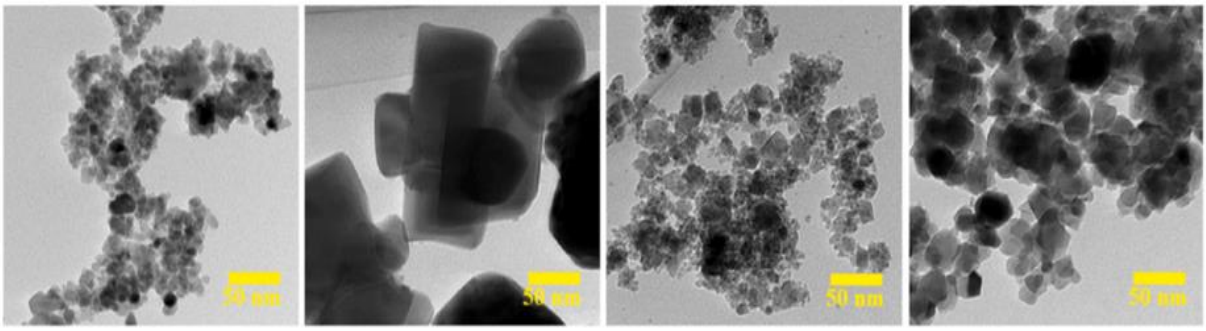

a) **b)** **c)** **d)**

FIGURE 3.1 Transmission electron microscope (TEM) images of the $CoFe_2O_4$ magnetic ferrite (CMF) nanoparticles prepared by the sol-gel (SG: **a** and **b**) and co-precipitation (Cpt: **c** and **d**) methods and thermally treated at 400 ºC (**a** and **c**) and 700 ºC (**b** and **d**).

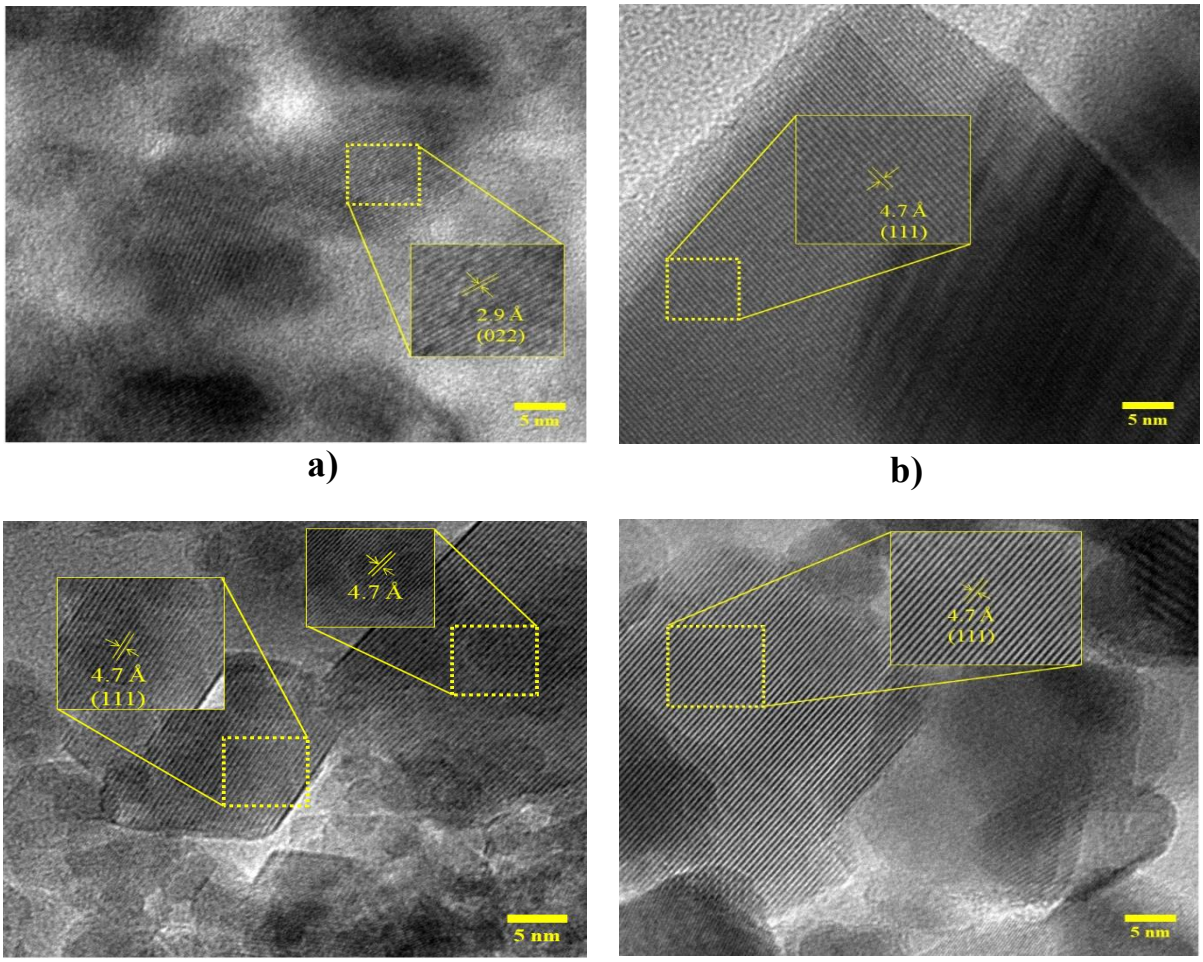

FIGURE 3.2 High-resolution transmission electron micrography (HRTEM) images of the as-prepared **a)** SG 400 ºC/1 h, **b)** SG 700 ºC/1 h, **c)** Cpt 400 ºC/1 h, and **d)** Cpt 700 ºC/1 h samples.

Figure 3.3 shows the XRD of the as-prepared magnetic material and for distinct synthesis and thermal treatment. The diffraction pattern of all tested materials can be indexed to the ICSD card number 98-010-9045 of $CoFe_2O_4$. As expected, high temperatures led to more defined diffraction peaks without impurities in the XRD pattern.

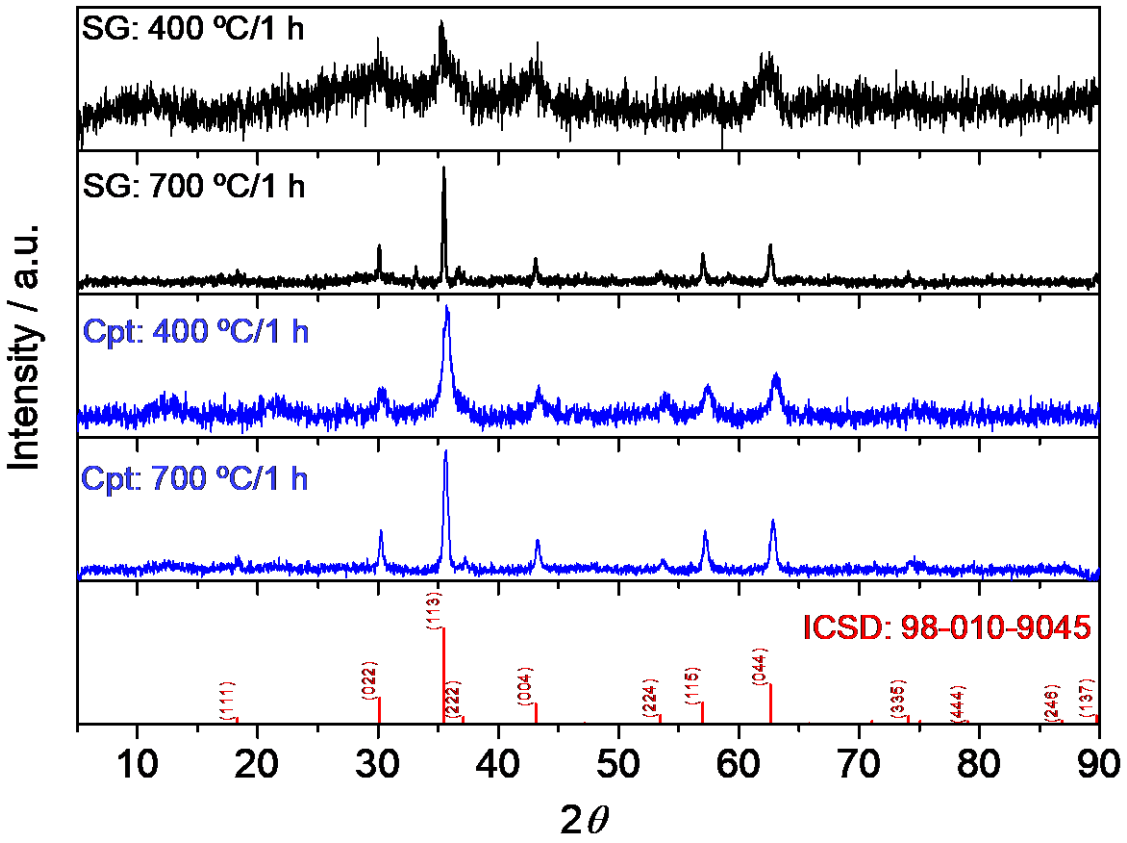

FIGURE 3.3 X-ray diffraction (XRD) patterns of the as-prepared $CoFe_2O_4$ magnetic ferrite at distinct experimental conditions: SG and Cpt refer to the sol-gel and co-precipitation synthesis procedure, respectively, followed by thermal treatment at 400 ºC or 700 ºC for 1 h. Diffraction peaks were in accordance with the ICSD card Nº 98-010-9045 of $CoFe_2O_4$.

FTIR spectra of the AsP magnetic compound are showed in Figure 3.4. In general, some common features can be noticed, *i.e.*, *i*) a weak band around 3500 cm^{-1} (more intense for the SG 400 ºC/1 h sample) due to the O-H bond stretching, which can be related by the surface terminations because of exposure to the environment (and consequent adsorption of moisture) or, in the case of sol-gel synthesis, to traces of polyvinyl alcohol; *ii*) O=C=O stretching vibrations because of atmospheric CO_2 at *ca*. 2350 cm^{-1} ; *iii*) C=O stretching *ca*. 1700 cm^{-1}; and *iv*) Fe-O and Co-O bond vibration bands at *ca*. 560 to *ca*. 400 cm^{-1}, respectively.

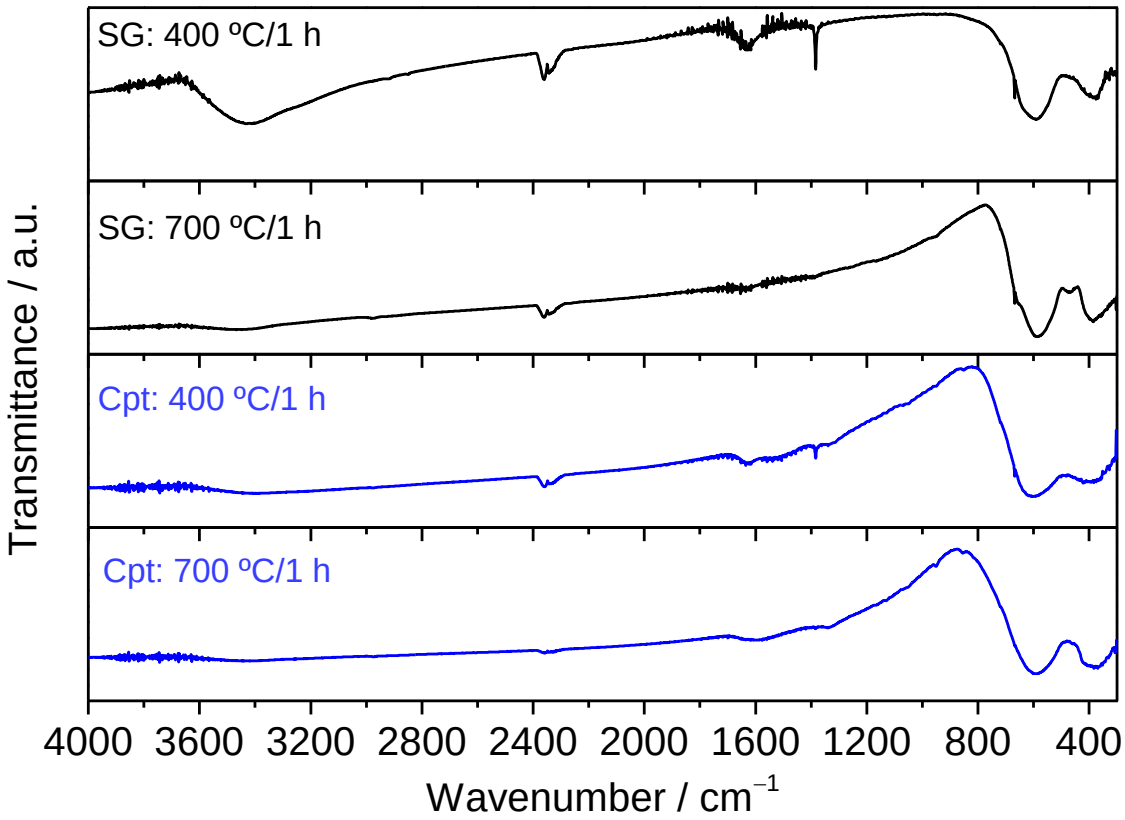

FIGURE 3.4 FTIR spectra the as-prepared $CoFe_2O_4$ magnetic ferrite at distinct experimental conditions: SG and Cpt refer to the sol-gel and co-precipitation synthesis procedure, respectively, followed by thermal treatment at 400 ºC or 700 ºC for 1 h.

The surface composition and bonding states of the AsP CMF nanoparticles were investigated by *ex situ* XPS measurements. As can be noted in Figure 3.5, the O 1s core-level spectra were deconvoluted into four peaks. The main components of all spectra are related to O-Metal (O^{-2}) bonds at 530.0 eV, hydroxyl groups (HO-Metal) at 531.2 eV, O-C and O-C=O type bonds of surface contamination (adventitious carbon) at about 532.0 and 533.0 eV, respectively [56]. The main difference among these spectra is a higher contribution of oxygenated groups of adventitious carbon and a higher intensity of the O-H bonds due to traces of PVA observed in the SG 400 °C/1 h sample, in agreement with infrared results. The Co $2p_{3/2}$ high-resolution spectra were deconvoluted into five peaks, three of them shake-up satellites. The most intense components refer to

$CoFe_2O_4$ (and/or Co_3O_4) at 779.7 eV and $Co(OH)_2$ surface groups at 781.4 eV [56], as shown in Figure 3.6. Clearly, for samples prepared by the sol-gel method, the Co-OH peak intensities are higher due to the PVA precursor. The Fe $2p_{3/2}$ spectra, highlighted in Figure 3.7, were fitted by four components and attributed to FeO at 709.5 eV, the most intense to $CoFe_2O_4$ at 710.8 eV, and FeOOH at 712.3 eV. In general, all deconvoluted spectra are similar, confirming the presence of the $CoFe_2O_4$ phase, except for the sol-gel samples where traces of PVA were detected. Finally, as can be observed in Figure 3.8, the C 1s spectra were deconvoluted into four peaks related to hydrocarbons (C-H) at 284.9 eV and oxygenated groups of alcohol/ether (C-O type at 286.3 eV), carbonyl (C=O at 287.7 eV, except for the Cpt samples), and carboxyl (-O-C=O at 289.4 eV) and mainly because of carbon contamination of the surface and synthesis conditions.

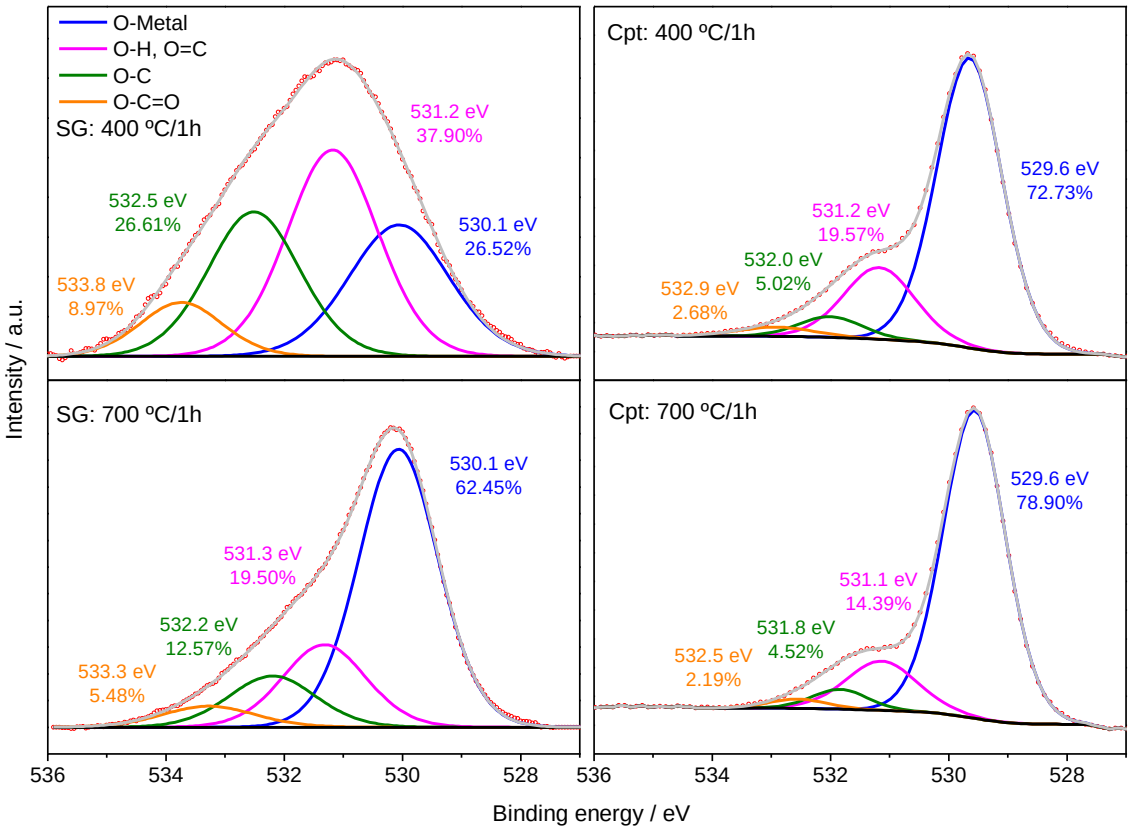

FIGURE 3.5 High-resolution spectra of O 1s for the as-prepared $CoFe_2O_4$ magnetic ferrite at distinct experimental conditions: SG and Cpt refer to the sol-gel and co-precipitation synthesis procedure, respectively, followed by thermal treatment at 400 ºC or 700 ºC for 1 h.

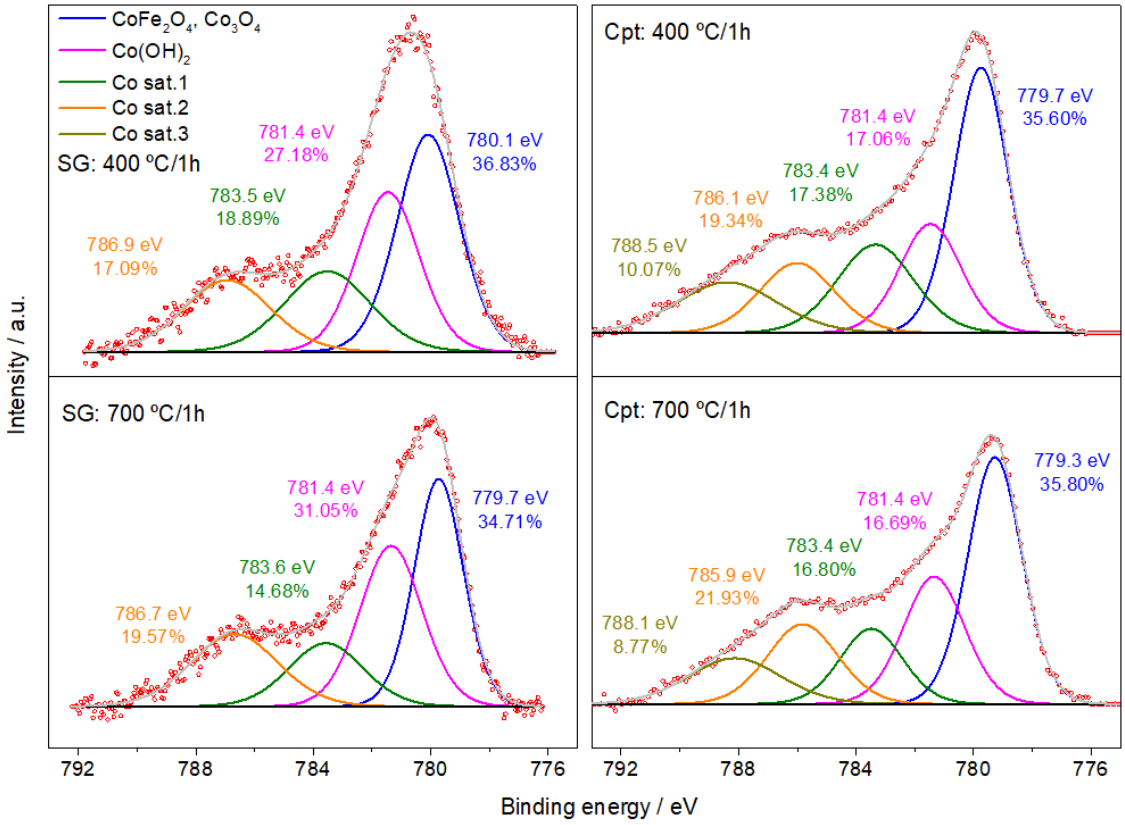

FIGURE 3.6 High-resolution spectra of Co $2p_{3/2}$ for the as-prepared $CoFe_2O_4$ magnetic ferrite at distinct experimental conditions: SG and Cpt refer to the sol-gel and co-precipitation synthesis procedure, respectively, followed by thermal treatment at 400 ºC or 700 ºC for 1 h.

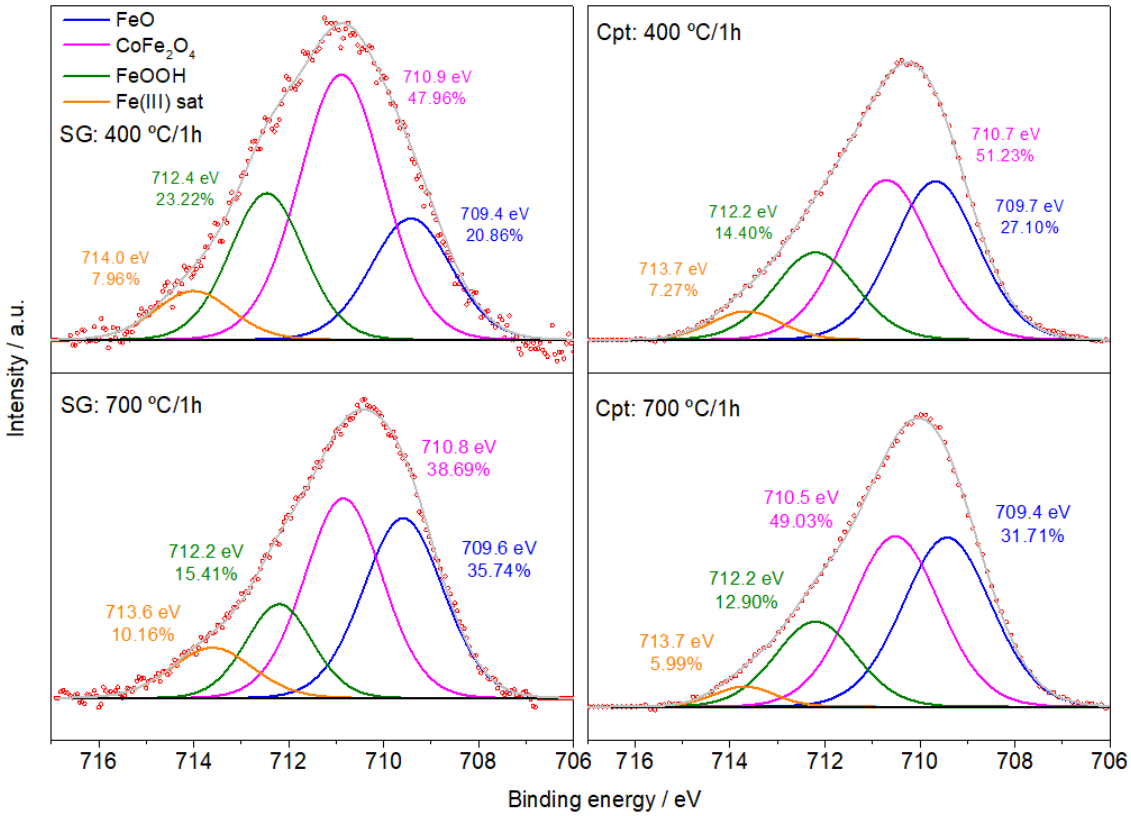

FIGURE 3.7 High-resolution spectra of Fe $2p_{3/2}$ for the as-prepared $CoFe_2O_4$ magnetic ferrite at distinct experimental conditions: SG and Cpt refer to the sol-gel and co-precipitation synthesis procedure, respectively, followed by thermal treatment at 400 ºC or 700 ºC for 1 h.

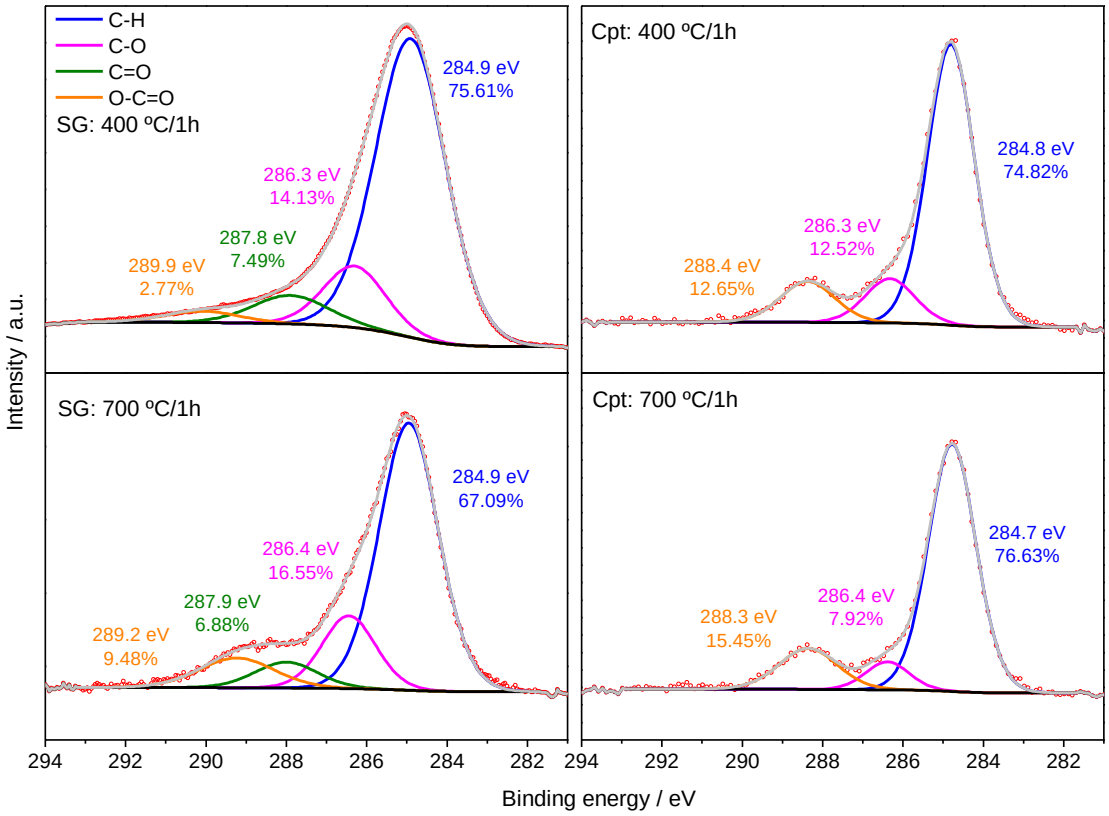

FIGURE 3.8 High-resolution spectra of C 1s for the as-prepared $CoFe_2O_4$ magnetic ferrite at distinct experimental conditions: SG and Cpt refer to the sol-gel and co-precipitation synthesis procedure, respectively, followed by thermal treatment at 400 ºC or 700 ºC for 1 h.

3.2 Catalytic performance evaluation: heterogeneous vs. homogeneous processes

3.2.1 PMS activation by $CoFe_2O_4$ for IMD oxidation: effect of [$CoFe_2O_4$] and [PMS]

Figure 3.9 shows the evolution of the remaining fraction of IMD and PMS consumption as a function of treatment time using 500 µM of PMS at pH 7. As noted in Figure 3.9a for the SG 400 ºC/1 h sample, there is a clear synergism between CMF and PMS showing a fast decrease in the IMD concentration. This can be seen when comparing the summation curve (dashed line in Figure 3.9a) from experiments without catalyst and PMS (0.125 g L^{-1} of CMF), being well above the curves when using a mixture of catalyst and oxidant. Concerning the

oxidation rate, no significant difference of the IMD degradation curves was observed for CMF concentrations, tested in the range of 0.125 to 1.00 g L^{-1}. All these points indicate that *i*) PMS is being activated to produce $HO^{\bullet}$ radical species (see discussion in section 3.3); and *ii*) low amounts of CMF are sufficient for a complete IMD oxidation. The unexpected low PMS consumption when using high amounts of CMF is due to its agglomeration in solution (Figure 3.9b) leading to a decrease in the available surface sites [57-58]. Consequently, 0.125 g L^{-1} of CMF is enough to assure complete oxidation of IMD and total PMS consumption. Lower values of CMF were not assessed due to experimental limitations.

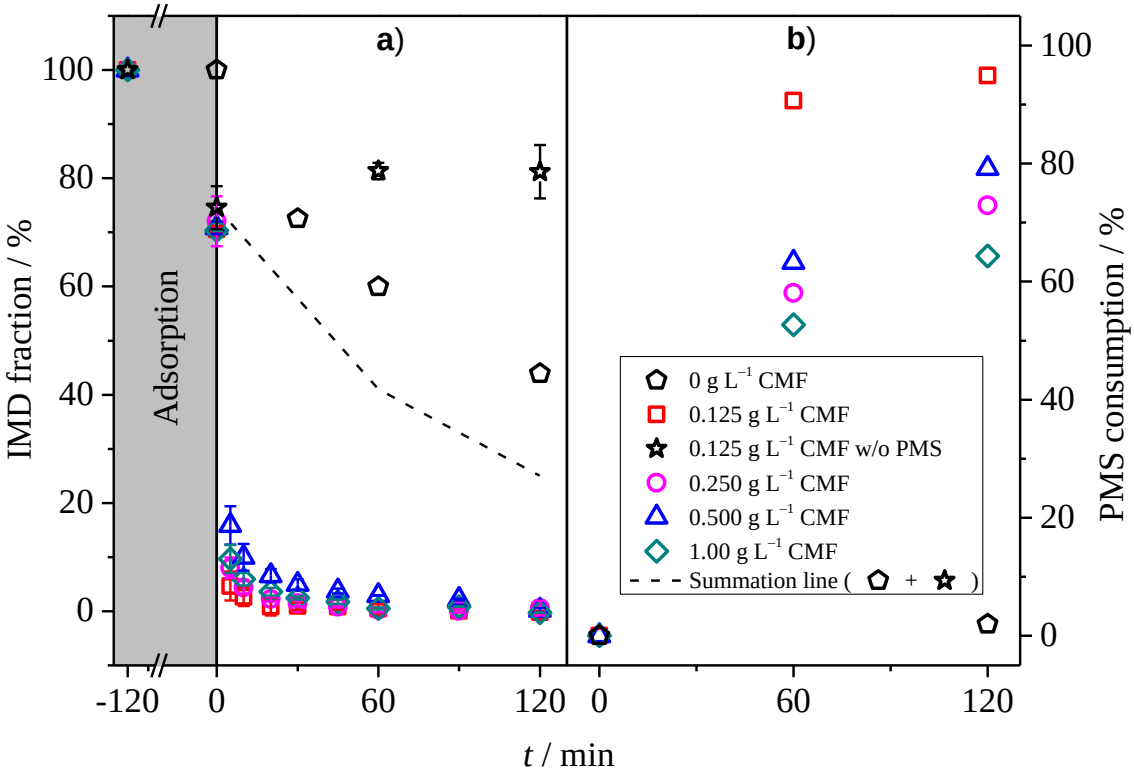

FIGURE 3.9 **a)** Remaining fraction of IMD (IMD fraction) and **b)** PMS consumption as a function of treatment time (t) using distinct amounts of $CoFe_2O_4$ (obtained by the sol-gel method and thermally treated at 400 °C for 1 h – SG 400 °C/1 h). **Conditions:** 500 μM PMS, pH 7.0, 10 mM KH_2PO_4, 150 mL of treating solution with 50 mg L^{-1} IMD at 25 °C. Error bars refer to two repetitions, except for the oxidant consumption. All experiments were carried out in the dark. w/o = without.

The evolution of the IMD fraction and PMS consumption as a function of time when using distinct concentrations of PMS (from 0 to1000 µM) and 0.125 g L^{-1} of CMF at pH 7 can be seen in Figure 3.10a. For PMS concentration values higher than 250 µM, complete oxidation of IMD is achieved after 30 min. In all experiments, PMS is completely consumed within 60 min of experiment (see Figure 3.11a); however, the initial amount of PMS seems to be insufficient to completely oxidize IMD when using 250 µM of PMS. Similar experiments were also carried out in the absence of the CMF material to assess the influence of PMS to solely oxidize IMD. As can be seen in Figure 3.10b, complete oxidation was only reached after 2 h of experiment when using 1000 µM of PMS (less than 50% of PMS consumption – see Figure 3.11b). For lower concentrations, more than 6 h is required to oxidize IMD (to *ca*. 90%).

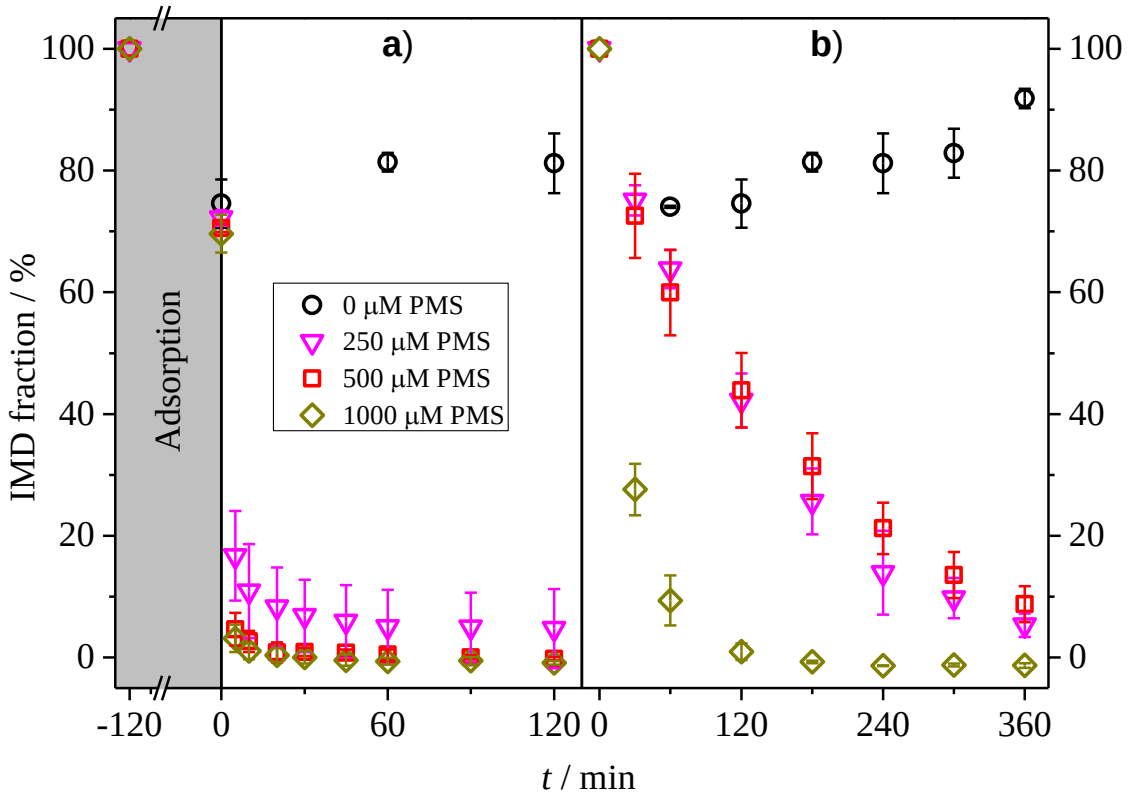

FIGURE 3.10 Remaining fraction of IMD (IMD fraction) as a function of treatment time (t) using distinct concentrations of PMS (see inset) **a)** in the presence and **b)** absence (control experiments) of 0.125 g L^{-1} CMF (SG 400 °C/1 h sample). **Conditions:** pH 7.0, 10 mM KH_2PO_4, 150 mL of treating solution with 50 mg L^{-1} IMD at 25 °C. Error bars refer to two repetitions. All experiments were carried out in the dark.

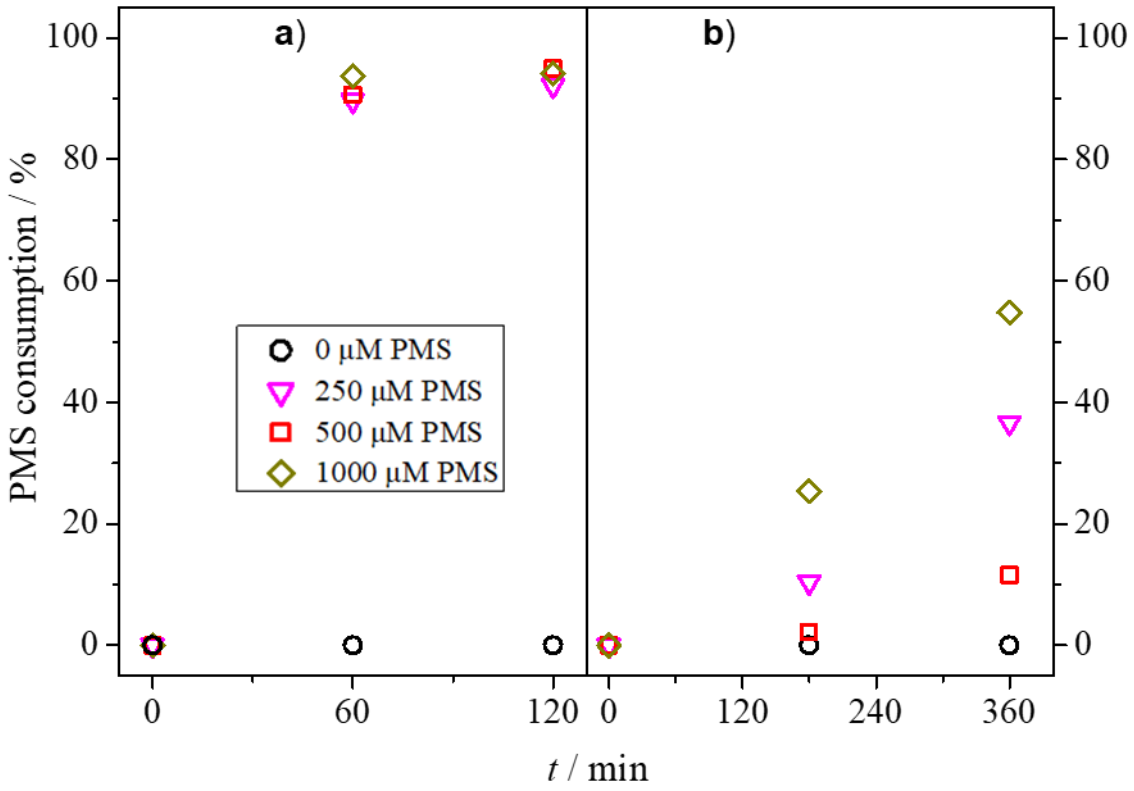

FIGURE 3.11 PMS consumption as a function of treatment time (*t*) using distinct PMS concentration values (see inset) **a)** in the presence and **b)** absence (control experiments) of 0.125 g L^{-1} CMF (SG 400 ºC/1 h sample). **Conditions:** 50 mg L^{-1} IMD, pH 7.0, 10 mM KH_2PO_4, 150 mL of treating solution at 25 ºC.

After this initial optimization concerning the catalyst load (0.125 g L^{-1}) and PMS concentration (500 µM) at neutral conditions, new experiments were carried out to compare the performance of the different synthesized materials, *i.e.*, SG 400 °C/1, SG 700 °C/1 h, Cpt 400 °C/1 h, and Cpt 700 °C/1 h, as shown in Figure 3.12a. For all prepared materials, the oxidation rate (close to 0.5 min^{-1}) and levels as well as the oxidant consumption were similar independently of the synthesis conditions and particle size. This was an unexpected behavior and may address to some uncontrolled variables, such as Co(II) ion leaching or even the use of buffered solution. In the latter case, as shown in Figure 3.12b and Table A6, for a complete oxidation (~30 min) only a small decrease in the IMD oxidation rate (0.53 min^{-1}) was observed when compared to the condition without buffer (0.14 min^{-1}). As the amount of PMS

was high enough, no further deleterious effects on the oxidation rate and level of IMD were observed. In the absence of buffer and with no pH control, the IMD oxidation rate dropped one order of magnitude (0.020 min^{-1}) with 90% oxidation in 120 min. In addition, a high consumption of PMS is observed when phosphate buffer was used (see Figure 3.13). Such behavior is due to the scavenging effect of $H_2PO_4^-$ ions [59] on produced reactive oxygen species. Undoubtedly, pH monitoring and control (see the pH evolution without buffer in Figure 3.13c) is of paramount importance as well as the use of buffer (type and concentration) [60] and PMS concentration.

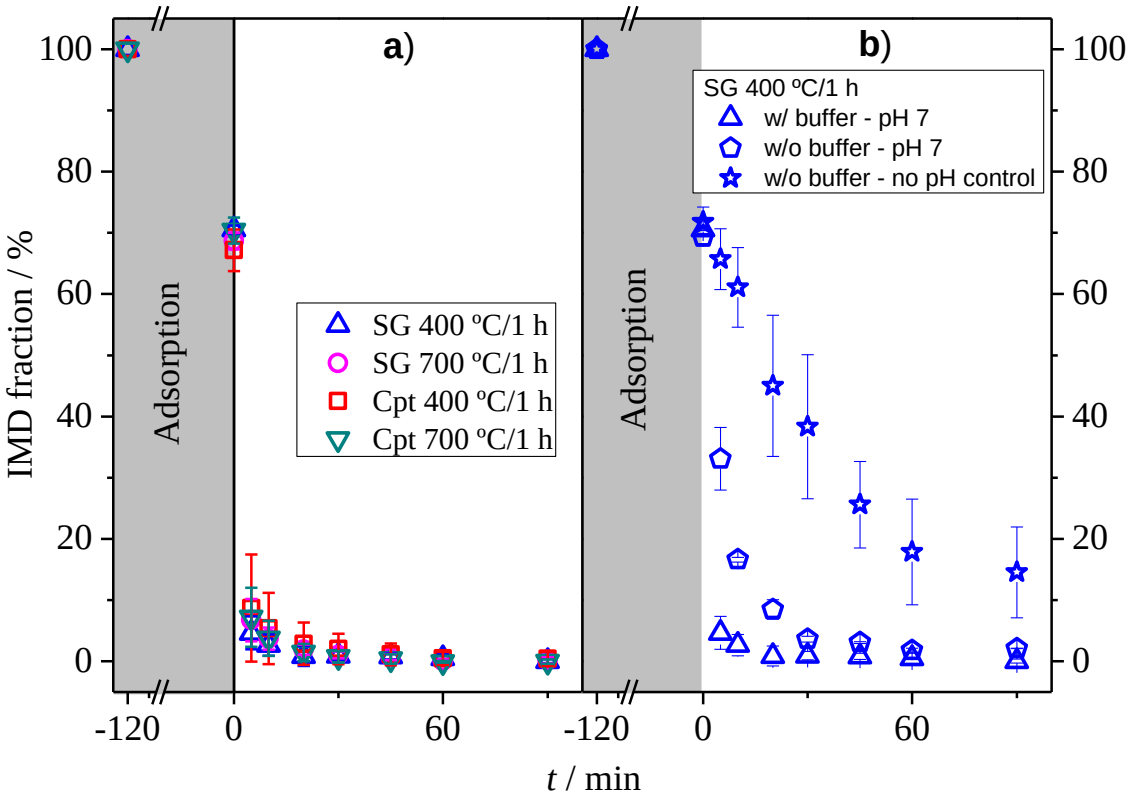

FIGURE 3.12 Remaining fraction of IMD (IMD fraction) as a function of treatment time (t) using **a)** CMF (cobalt magnetic ferrite) catalysts prepared at different conditions (see inset) and **b)** in the presence (w/= with) or absence (w/o = without) of a phosphate buffer solution (see inset) using the CMF material prepared by the sol-gel method and thermally treated at 400 ºC for 1 h (SG 400 ºC/1 h). **Conditions:** 0.125 g L^{-1} CMF, 500 µM PMS, pH 7.0, 10 mM KH_2PO_4, 150 mL of treating solution with 50 mg L^{-1} IMD at 25 ºC. Error bars refer to two repetitions. All experiments were carried out in the dark.

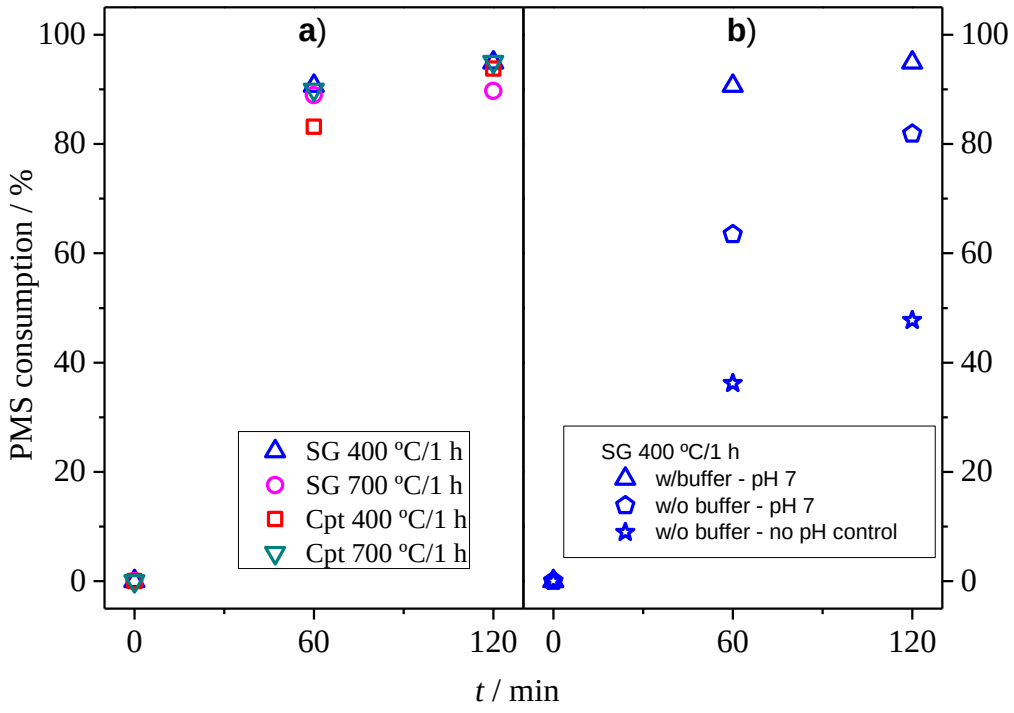

FIGURE 3.13 PMS consumption as a function of treatment time (t) using **a)** CMF (cobalt magnetic ferrite) catalysts prepared at different conditions (see inset), **b)** in the presence (w/ = with) or absence (w/o = without) of a phosphate buffer solution (see inset) using the CMF (cobalt magnetic ferrite) material prepared by the sol-gel method and thermally treated at 400 ºC for 1 h (SG 400 ºC/1 h), and **c)** pH evolution (for the condition with no pH control) as a function of treatment time (t). **Conditions:** 0.125 g L^{-1} CMF, 500 μM PMS, pH 7.0, 10 mM KH_2PO_4, 150 mL of treating solution at 25 °C. Error bars refer to two repetitions, except for the oxidant consumption. All experiments were carried out in the dark with manual pH corrections.

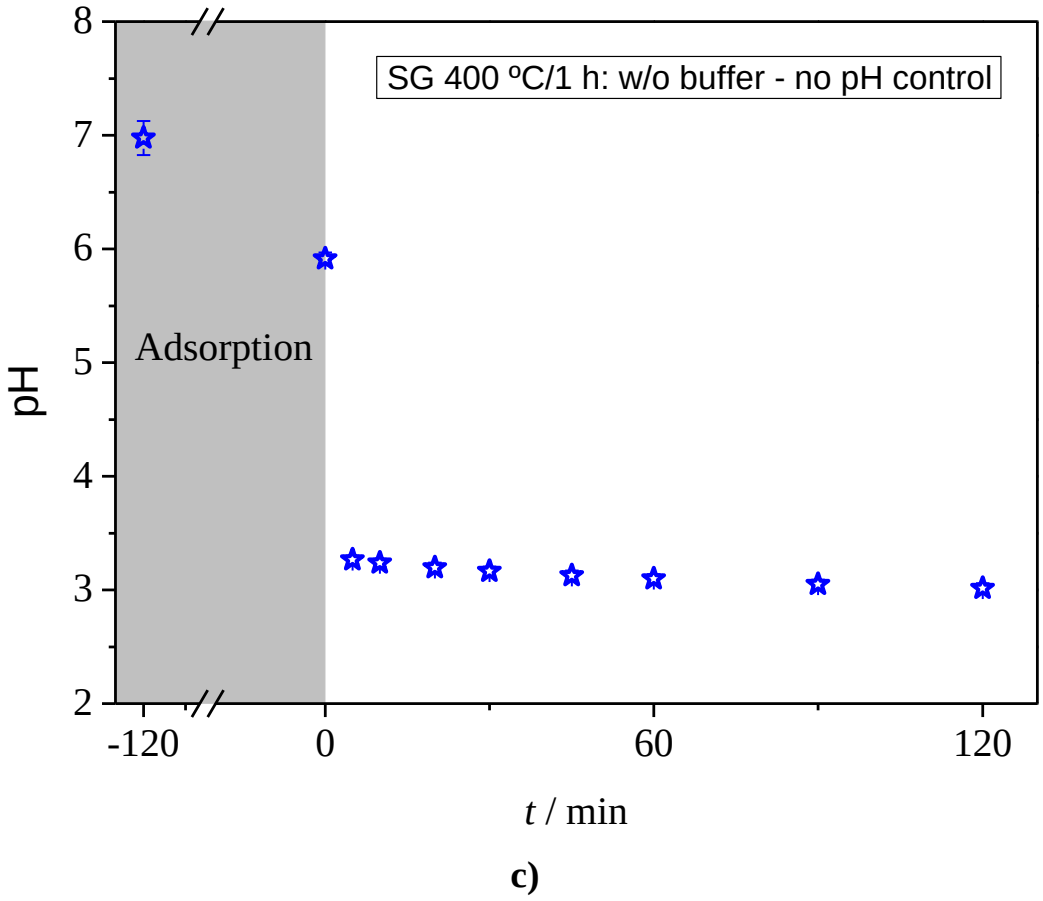

c)

FIGURE 3.13 *(continuation)* PMS consumption as a function of treatment time (*t*) using **a)** CMF (cobalt magnetic ferrite) catalysts prepared at different conditions (see inset), **b)** in the presence (w/ = with) or absence (w/o = without) of a phosphate buffer solution (see inset) using the CMF (cobalt magnetic ferrite) material prepared by the sol-gel method and thermally treated at 400 ºC for 1 h (SG 400 ºC/1 h), and **c)** pH evolution (for the condition with no pH control) as a function of treatment time (*t*). **Conditions:** 0.125 g L^{-1} CMF, 500 μM PMS, pH 7.0, 10 mM KH_2PO_4, 150 mL of treating solution at 25 °C. Error bars refer to two repetitions, except for the oxidant consumption. All experiments were carried out in the dark with manual pH corrections.

Considering Co(II) ion leaching, ICP-OES measurements were carried out as shown in Table A7. In all experiments shown in Figure 3.12, Co (from 170 to 49 μg L^{-1}) and Fe (from 300 to 32 μg L^{-1}) ions were detected, but without interferences in the CMF oxidation performance towards IMD. Unfortunately, the World Health Organization has not established a specific allowable limit for Co(II) ions in potable water. To verify a possible influence of these ions on IMD oxidation, an additional experiment was performed concerning the addition of Co(II) and Fe(III) ions in the absence of the CMF nanomaterial. As can be seen in Figure 3.14, the use of 200 or 20 μg L^{-1} of Co(II) ions led to a prompt oxidation of IMD in less than 30 min with almost complete PMS consumption after 1 h and 2 h, respectively. This result was very similar to that when the CMF nanoparticles (see red square) were used. On the other hand, the use of 50 μg L^{-1} of Fe(III) ions led to 80% of IMD oxidation after 2 h with only 10% PMS consumption after 2 h.

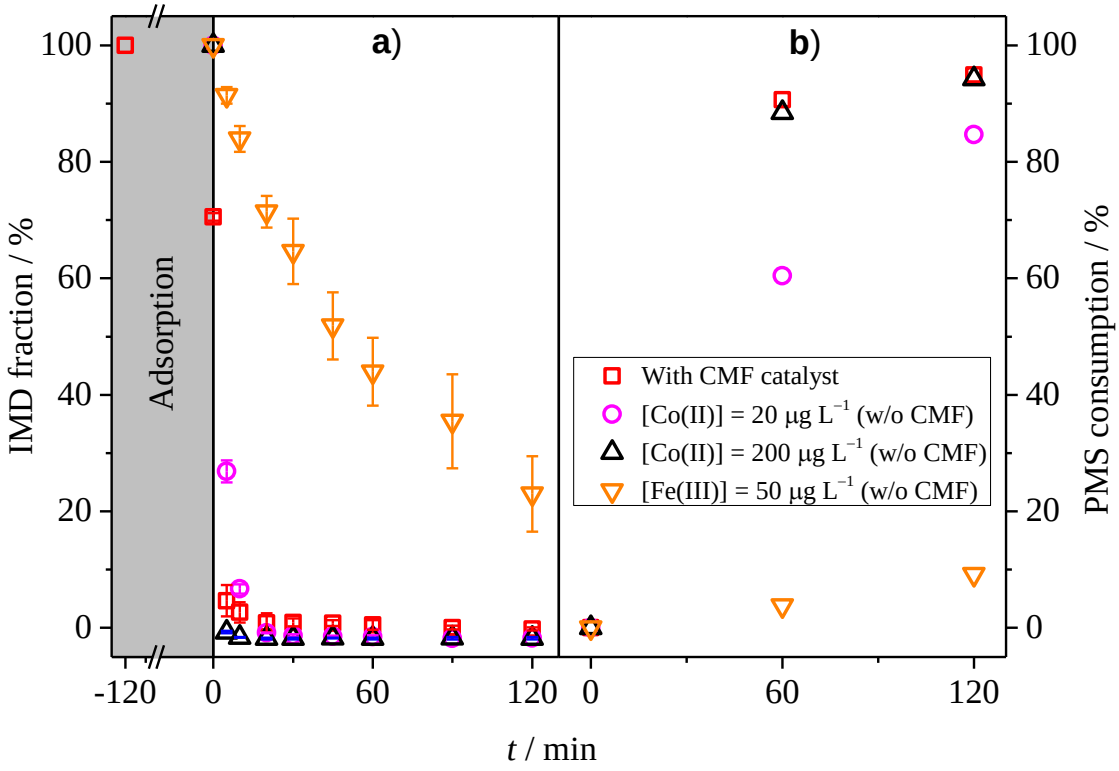

FIGURE 3.14 **a)** Remaining fraction of IMD (IMD fraction) and **b)** PMS consumption as a function of treatment time (t) using distinct concentration values of Co(II) and Fe(III) ions (see inset). **Conditions:** 0.125 g L^{-1} CMF, 500 µM PMS, pH 7.0, 10 mM KH_2PO_4, 150 mL of treating solution with 50 mg L^{-1} IMD at 25 ºC. Error bars refer to two repetitions, except for the oxidant consumption. All experiments were carried out in the dark.

Other experiments were carried out using decreasing amounts of Co(II) ions, as shown in Figure 3.15. For Co(II) ion concentration higher than 15.6 µg L^{-1}, complete oxidation of IMD was achieved in less than 30 min, whereas 7.8 and 3.9 µg L^{-1} required *ca*. 1 h of reaction. Currently, and although some studies do not address the effect of PMS activation upon Co(II) ion leaching (see Table 1.2), only a marginal influence is claimed on Co(II) ions, *i.e.*, only a small contribution of homogeneous reaction. To fully address this issue, experiments with Co(II) addition were performed without phosphate buffer (with or without pH control by manual additions of diluted H_2SO_4 and/or NaOH solutions). As seen in Figure 3.16, no deleterious effect on IMD oxidation level or rate (see Table

A6) was observed for the homogeneous process in the presence or absence of buffer if pH was kept at ~7. When solution pH was left varying in the absence of buffer (Figure 3.16c) a significant decrease in the IMD oxidation rate (one order of magnitude: 0.039 min^{-1}) and complete oxidation after 60 min were observed after the solution pH dropped to 3 (after addition of PMS) and then remained constant during the entire experiment. Once again, the key difference among tested conditions was the highest PMS consumption (Figure 3.16b) in the presence of phosphate buffer (~100% compared to less than 40%) due to quenching promoted by $H_2PO_4^-$ ions.

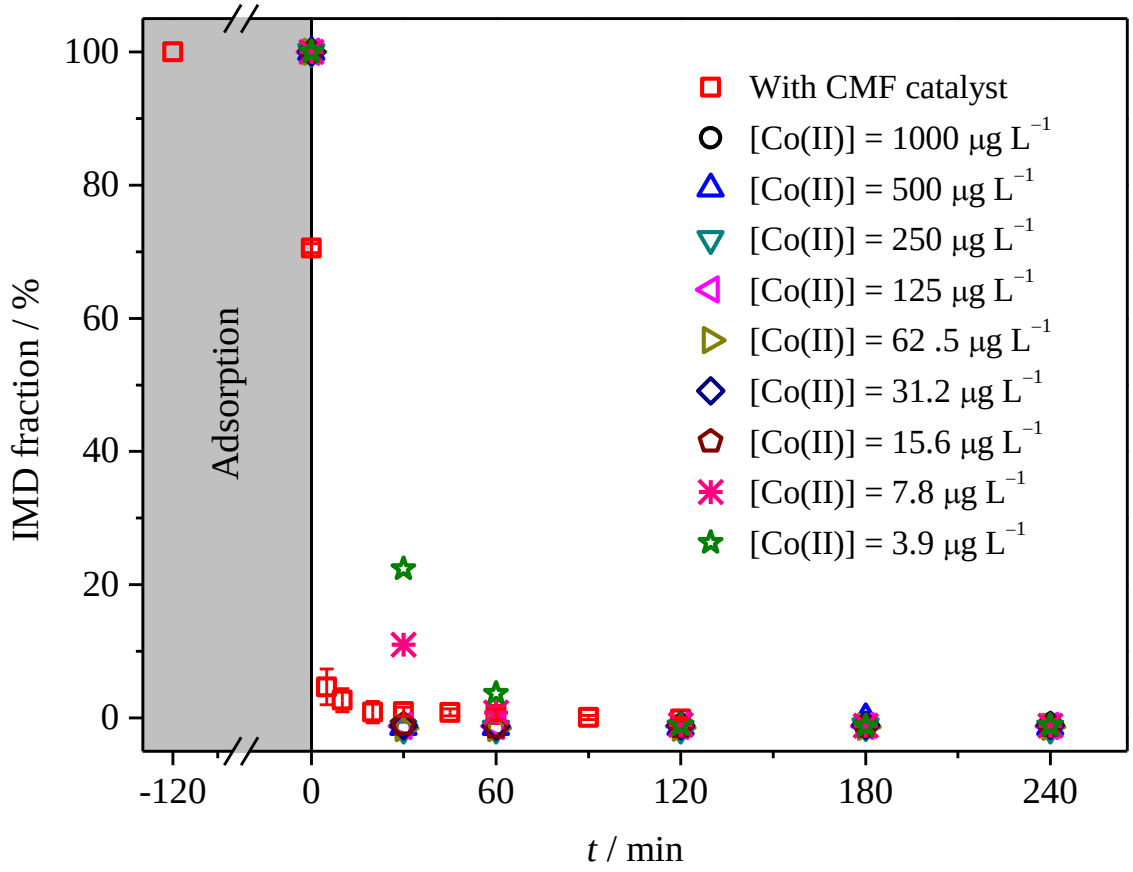

FIGURE 3.15 Remaining fraction of IMD (IMD fraction) as a function of treatment time (*t*) using distinct Co(II) ion concentration values (see inset – dilution factor of 2). **Conditions:** 50 mg L^{-1} IMD, 500 µM PMS, pH 7.0, 10 mM KH_2PO_4, 25 °C and 0.125 g L^{-1} CMF when SG 400 ºC/1 h compound was used. No repetitions were carried out. CMF = cobalt magnetic ferrite ($CoFe_2O_4$).

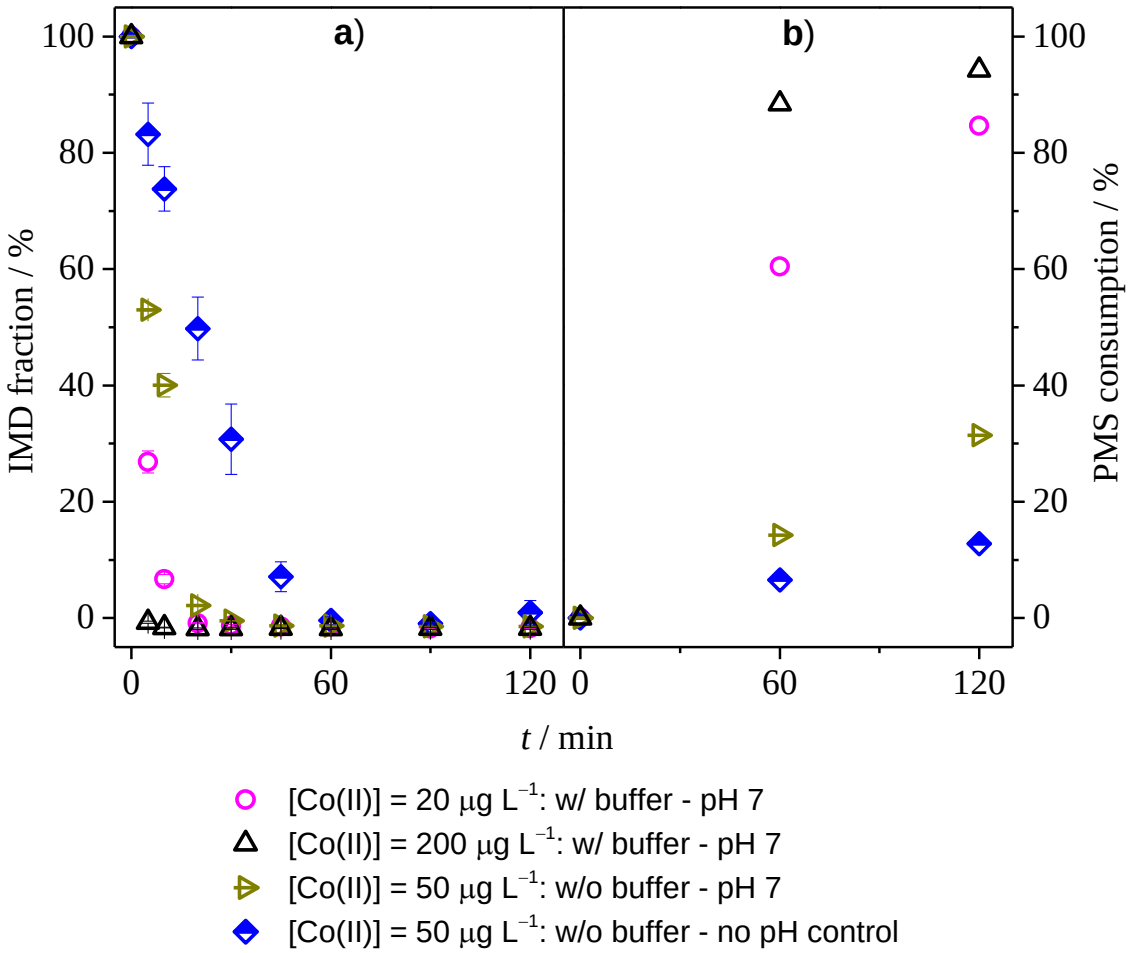

FIGURE 3.16 **a)** Remaining fraction of IMD (IMD fraction), **b)** PMS consumption, and **c)** pH monitoring as a function of treatment time (*t*) in the presence (w/ = with) or absence (w/o = without) of a buffer solution using distinct Co(II) ion concentration values (see inset). **Conditions:** 50 mg L^{-1} IMD, 500 μM PMS, pH 7.0 (see inset), 10 mM KH_2PO_4 (see inset) and 25 °C. Error bars refer to two repetitions, except for the oxidant consumption. All experiments were carried out in the dark with manual pH corrections.

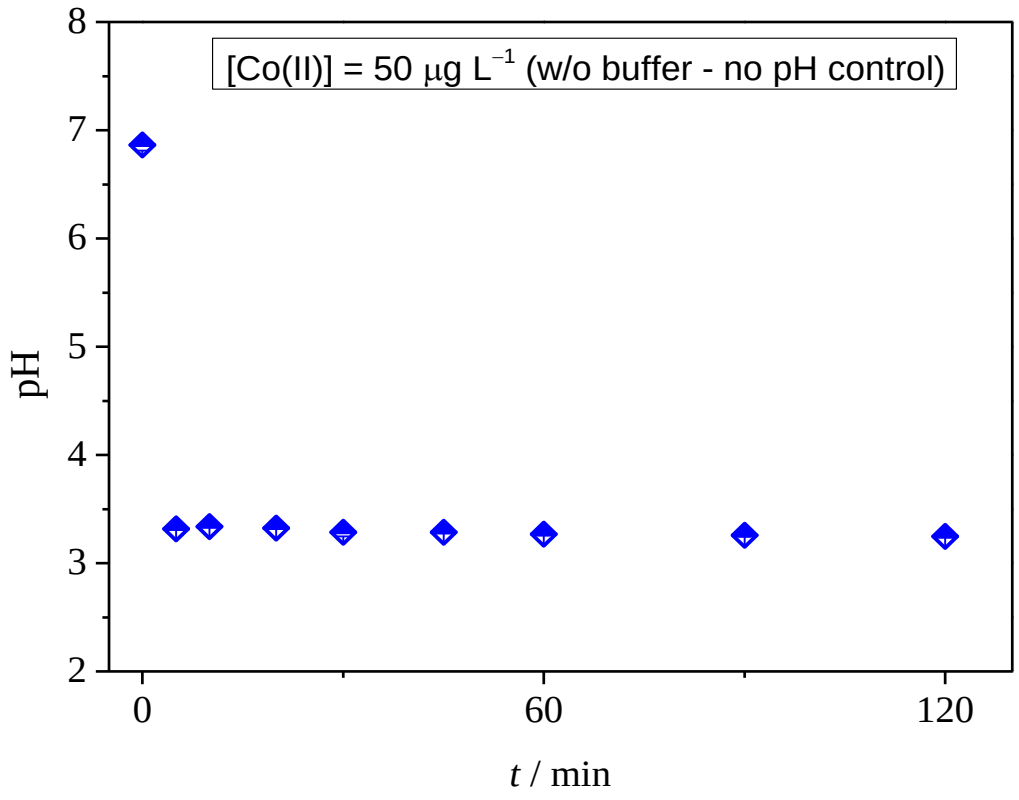

c)

FIGURE 3.16 *(continuation)* **a)** Remaining fraction of IMD (IMD fraction), **b)** PMS consumption, and **c)** pH monitoring as a function of treatment time (*t*) in the presence (w/ = with) or absence (w/o = without) of a buffer solution using distinct Co(II) ion concentration values (see inset). **Conditions:** 50 mg L^{-1} IMD, 500 μM PMS, pH 7.0 (see inset), 10 mM KH_2PO_4 (see inset) and 25 °C. Error bars refer to two repetitions, except for the oxidant consumption. All experiments were carried out in the dark with manual pH corrections.

Based on the results of the experiments with Co(II) ions and CMF material at different conditions, the oxidation of IMD seems to be mediated by Co(II) ions leaching from the magnetic ferrite particles. In fact, ***the solid material act as a Co(II) ion source, which efficiently activates PMS if pH is kept under neutral conditions (pH 7*)**. Therefore, correction and monitoring of solution pH is highly recommended.

To tackle the issue of Co(II) leaching from CMF, two strategies were applied (see Text A6): *i*) carbonization of the CMF nanoparticles obtained by the Cpt method at 700 ºC/1 h (no interferences from PVA) using glucose; and *ii*) carbonization of the resulting products from the sol-gel synthesis at 400 ºC (SG 400 ºC/1 h @C) and 700 ºC (SG 700 ºC/1 h @C) for 1 h. Both strategies aimed to coat CMF nanoparticles with a carbon layer using a tube furnace at anoxic conditions (N_2 gas). As can be seen in Figures 3.17 and 3.18, the oxidation rate and levels remained equal to those previously obtained without carbonization, *i.e.*, the IMD molecule was promptly oxidized in less than 30 min. The only observed difference refers to the PMS consumption rate (see Figure 3.18b). The amount of Co and Fe ions detected in experiments of Figures 3.17 and 3.18 is presented in Table A8. Under all analysis conditions, Co and Fe ions were detected at unexpected high values, particularly for the surface modification carried out using glucose. Low values of Co and Fe ions were only observed for the SG 700 ºC/1 h@C samples, *i.e.*, tens of micrograms per liter. The detected quantities of Co ions explain the extraordinarily high values of IMD oxidation rate and levels shown in Figures 3.17 and 3.18. The reason for that lies in the non-uniform carbon particle passivation, which enabled ion leaching, as shown by the HRTEM images in Figure A3. Nevertheless, more research is needed to address the metal ion leaching issue from metallic oxide compounds.

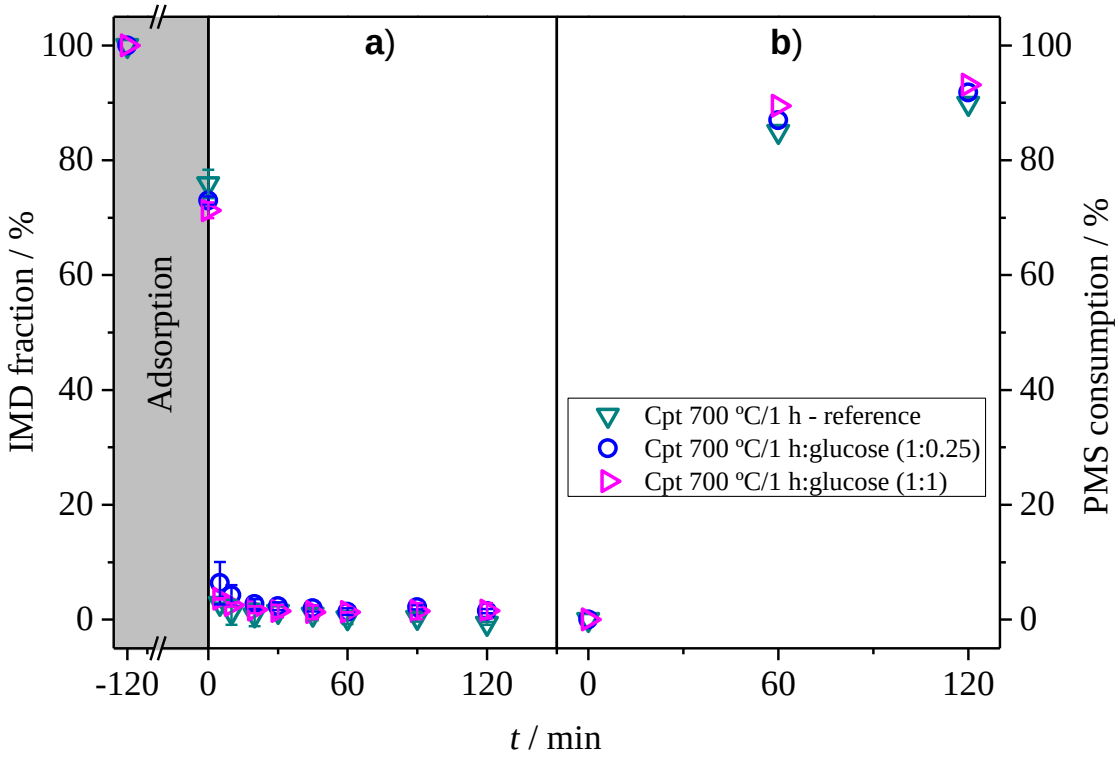

FIGURE 3.17 **a)** Remaining fraction of IMD (IMD fraction) and **b)** PMS consumption as a function of treatment time (*t*) using CMF nanoparticles previously obtained from the Cpt method (Cpt 700 ºC/1 h) and carbonized in an anoxic atmosphere (N_2 gas). The carbon source was glucose at a mass ratio of 1:0.25 (Cpt: 700 ºC/1 h : glucose (1:0.25)) and 1:1 (Cpt: 700 ºC/1 h : glucose (1:1)). **Conditions:** 50 mg L^{-1} IMD, 500 µM PMS, pH 7.0, 10 mM KH_2PO_4, 25 °C and 0.125 g L^{-1} of CMF. Error bars refer to two repetitions, except for the oxidant consumption. The Cpt 700 ºC/1 h data was included for comparison purposes. CMF = cobalt magnetic ferrite ($CoFe_2O_4$).

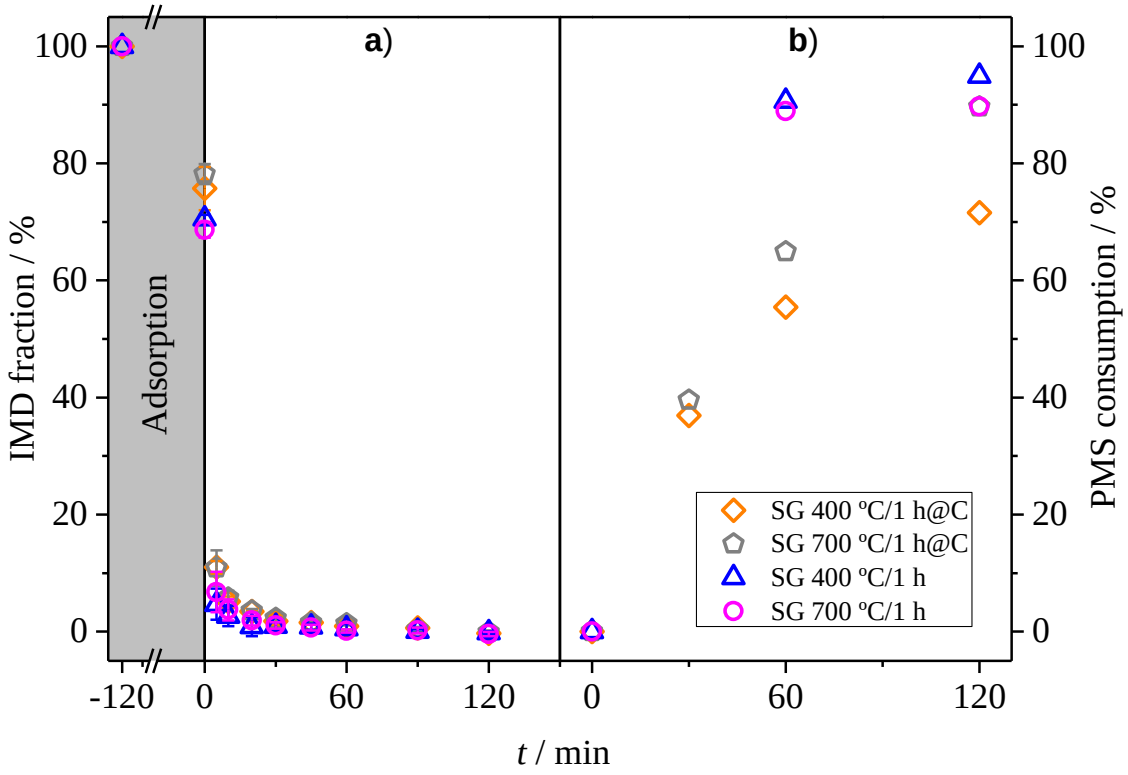

FIGURE 3.18 **a)** Remaining fraction of IMD (IMD fraction) and **b)** PMS consumption as a function of treatment time (*t*) using CMF nanoparticles previously obtained from the SG synthesis and carbonized in an anoxic atmosphere (N_2 gas). The carbon source was the resulting powder of the SG synthesis that was carbonized at 400 ºC (SG 400 ºC/1 h@C) and 700 ºC (SG 700 ºC/1 h@C) for 1 h. **Conditions:** 50 mg L^{-1} IMD, 500 µM PMS, pH 7.0, 10 mM KH_2PO_4, 25 °C and 0.125 g L^{-1} of the solid materials. Error bars refer to two repetitions, except for the oxidant consumption. CMF = cobalt magnetic ferrite ($CoFe_2O_4$).

Thus, for experiments with tap water and simulated municipal wastewater (SMWW), the oxidation performance of IMD was evaluated using the CMF SG 700 ºC/1 h@C sample as heterogenous and Co(II) (38 µg L^{-1}: the same value reported in Table A8) as homogenous catalyst.

3.2.2 PMS activation by modified $CoFe_2O_4$ and Co(II) ions for IMD oxidation in a SMWW and tap water

The activation of oxidants in real water matrices is challenging due to the scavenging effect promoted by inorganic ions (such as HCO_3^-, CO_3^{2-}, Cl^-, etc.) and organic matter, such as humic acid. SMWW and tap water matrices, detailed in Tables A2 and A3 and Text A1, were used to access the oxidation performance of the SG 700 ºC/1 h@C sample towards the IMD insecticide. To compare this process with the *in situ* chemical activation of PMS using dissolved Co(II) ions, the same experiments were carried out using 38 µg L^{-1} of Co(II) ions. As can be seen in Figure 3.19a (see Figure 3.20a for the PMS consumption), the use of SG 700 ºC/1 h@C and Co(II) ions led to 70% and 85% IMD oxidation in SMWW, respectively, after 120 min. As expected, the oxidation rate (*ca*. 2×10^{-2} min^{-1} for SG 700 ºC/1 h@C and Co(II) ions) in the simulated effluent decreased due to the presence of inorganic and organic species that consumed the generated $HO^{\bullet}$ radical species. The latter behavior is significant and might indicate different oxidizing species [30], such as $^1O_2$, rather than $HO^{\bullet}$ and/or $SO_4^{\bullet-}$ (see discussion below). The distinct oxidation levels of IMD achieved for Co(II) ions and solid CMF might be due to complete PMS consumption. As expected, in the experiments using tap water (see Figure 3.19b and Figure 3.20b for the PMS consumption), the oxidation rate was higher than those using SMWW due to a lower content of inorganic ions and dissolved organic matter. Compared to experiments with ultrapure H_2O the oxidation rate decreased only slightly (*ca*. 0.3 min^{-1} for SG 700 ºC/1 h@C and Co(II) ions). Nevertheless, from the results of PMS consumption, it's possible to assure that the oxidant is being activated by Co(II) ions (compare the low chemical oxidation ability of PMS in Figure 3.19 and its low consumption in Figure 3.20 – magenta circles). Clearly, the presence of organic matter and inorganic ions dropped the oxidation ability (by providing more organic moieties to scavenge radicals) of non-selective $HO^{\bullet}$ and/or $SO_4^{\bullet-}$ in

SMWW, as also described in literature [61-62], compared to tap water (most inorganic species to scavenge radicals) and ultrapure water.

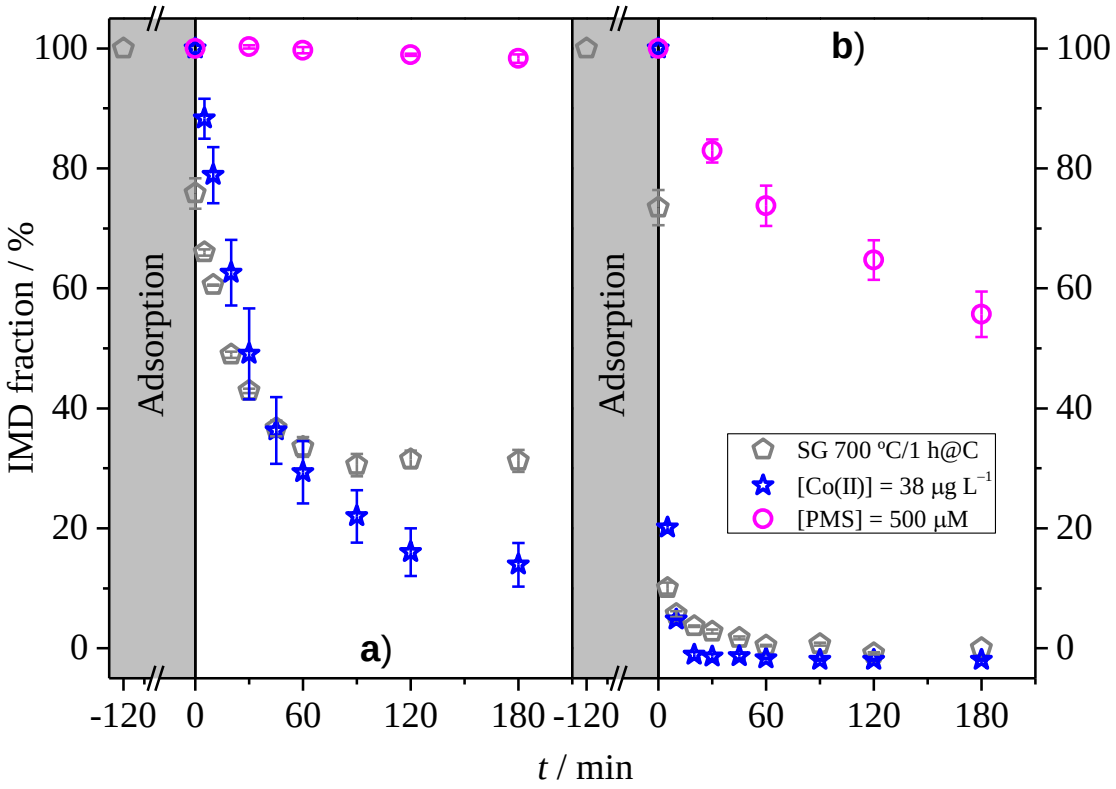

FIGURE 3.19 Remaining fraction of IMD (IMD fraction) in **a)** a simulated municipal wastewater model effluent matrix and **b)** tap water as a function of treatment time (t) using Co(II) ions and CMF nanoparticles previously obtained from the sol-gel synthesis and carbonized at 700 ºC for 1 h (SG 700 ºC/1 h@C) in an anoxic atmosphere (N_2 gas). **Conditions:** 50 mg L^{-1} IMD, 500 µM PMS, pH 7.0, 10 mM KH_2PO_4, 25 ºC, and 0.125 g L^{-1} of the SG 700 ºC/1 h@C sample. Error bars refer to two repetitions.

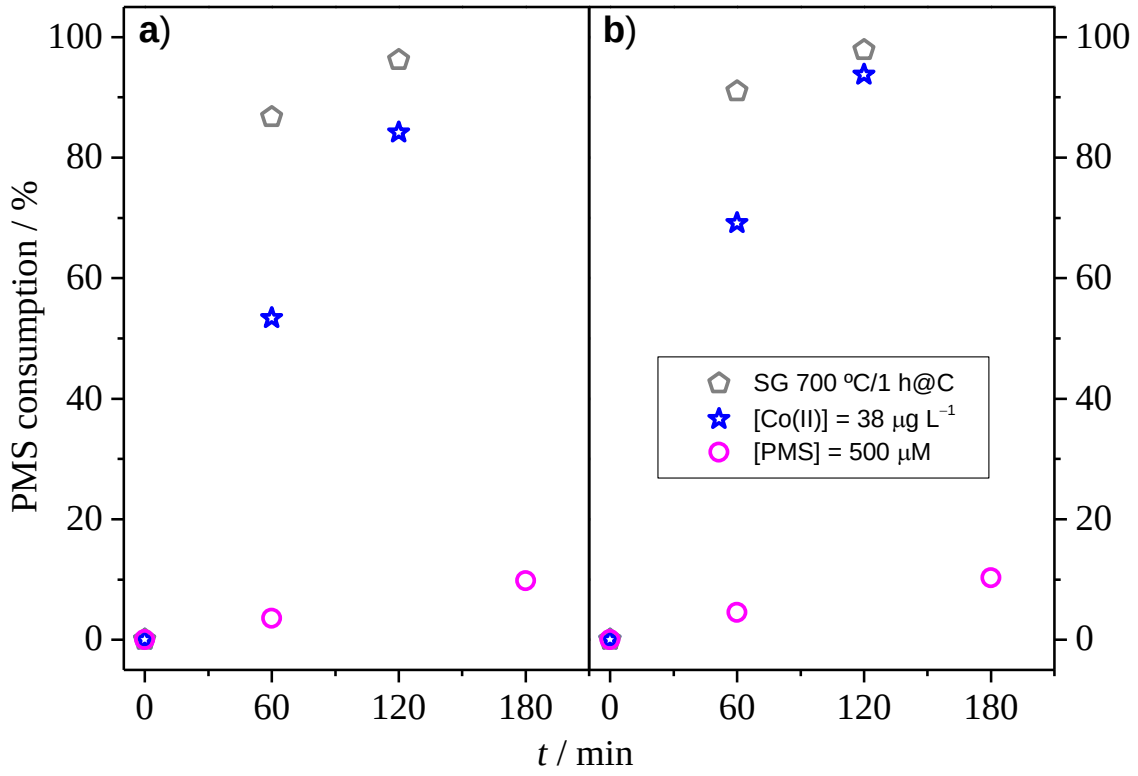

FIGURE 3.20 PMS consumption in **a)** a simulated municipal wastewater model effluent matrix and **b)** tap water as a function of treatment time (*t*) using Co(II) ions and CMF nanoparticles previously obtained from the SG synthesis and carbonized at 700 ºC for 1 h (SG 700 ºC/1 h@C) in an anoxic atmosphere (N_2 gas). **Conditions:** 50 mg L^{-1} IMD, 500 µM PMS, pH 7.0, 10 mM KH_2PO_4, 25 °C, and 0.125 g L^{-1} of the SG 700 ºC/1 h@C sample. Error bars refer to two repetitions, except for the oxidant consumption.

3.3 UHPLC-QToF MS and carboxylic acid determinations: IMD degradation byproducts and pathways

For the UHPLC-QToF MS experiments, only five intermediates were detected when using the optimized conditions (0.125 g L^{-1} catalyst, 500 µM PMS and pH 7.0) for the SG 400 ºC/1 h compound. The latter was chosen due to the similarities observed among the assayed compounds (see Figures 3.12 and 3.18). The extracted ion chromatogram and tandem mass spectrometry (MS/MS) analyses of IMD and its byproducts can be seen in Figures 3.21 and A4, respectively.

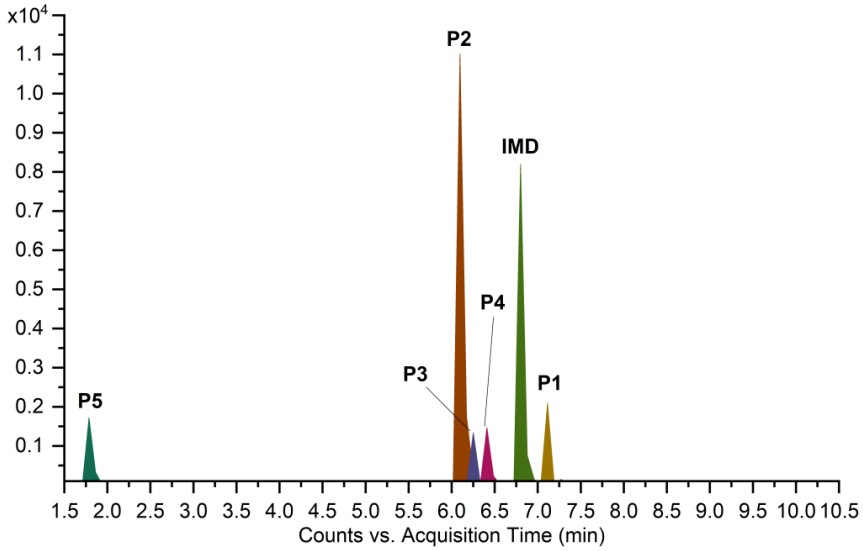

FIGURE 3.21 Extracted ion chromatogram (EIC) of the main detected byproducts (5 in total) resulting from IMD oxidation by radical species resulting from PMS activation by $CoFe_2O_4$ (SG 400 ºC/1 h sample). **Conditions:** 50 mg L^{-1} IMD, 500 µM PMS, pH 7.0, 10 mM KH_2PO_4, 25 °C and 0.125 g L^{-1} of the SG 400 ºC/1 h sample.

Figure 3.22 shows the intermediates and proposed degradation route, which is in agreement with that reported by Bourgin *et al.*, [63]. More information regarding the retention time and main ionic fragments as well as the proposed fragmentation route of the main intermediates can be seen in Table A9 and Figure A5.

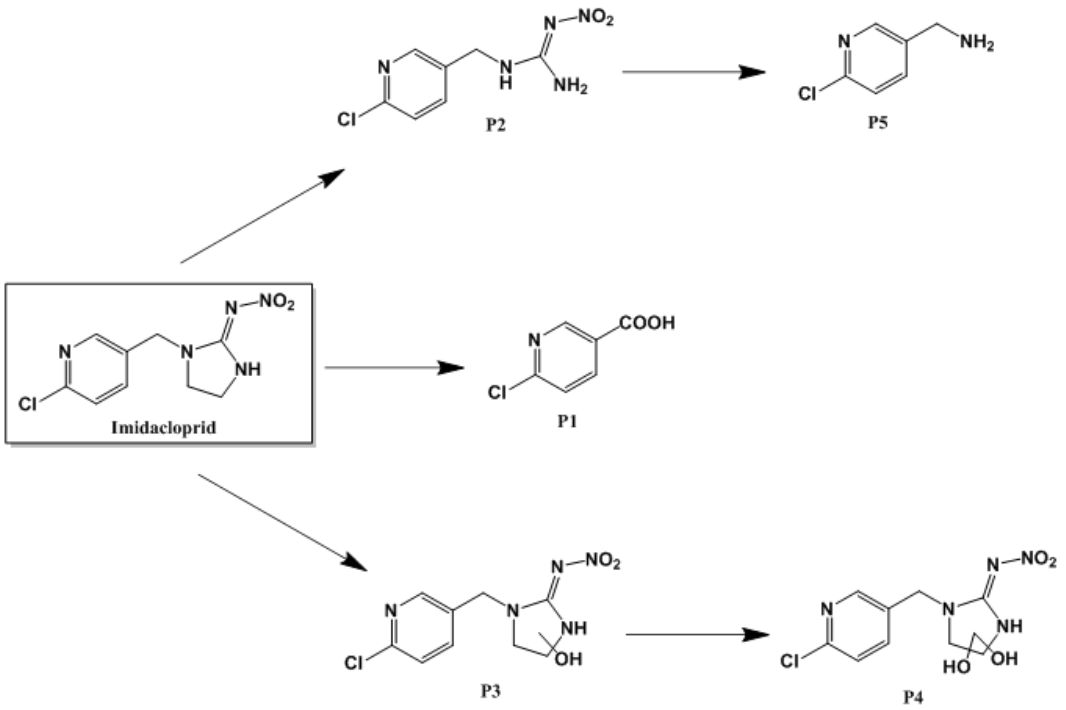

FIGURE 3.22 Proposed degradation pathways of IMD using the SG 400 ºC/1 h compound to the *in situ* chemical activation of PMS. **Conditions:** 0.125 g L^{-1} CMF, 500 μM PMS, pH 7.0, 10 mM KH_2PO_4, 150 mL of treating solution with 50 mg L^{-1} IMD at 25 ºC. CMF = cobalt magnetic ferrite ($CoFe_2O_4$).

As observed, all oxidation steps occur on the imidazolidine ring, mediated by $HO^{\bullet}$ in consecutive oxidation steps, (see byproducts **P3** and **P4**) or even $SO_4^{\bullet-}$ radicals (followed by hydrolysis reaction for the latter) and to a less extent by $^1O_2$. Three intermediates (**P1**, **P2**, and **P5**) exhibited a rupture or loss of the imidazolidine ring. All proposed chemical structures of intermediates agree with those previously reported [63-66]. Although a low number of intermediates was detected, all of them were organochlorine byproducts and persistent, mainly **P2** and **P1** as well as IMD until 120 min of treatment, as shown in the extracted ion chromatograms of Figure A6. In the final stages of the oxidation process, only three carboxylic acids (see Figure A7) were detected at concentrations as low as 1 mg L^{-1} and close to the quantification limit. Inorganic ions resulting from IMD oxidation (*i.e.*, NO_3^- and Cl^-) were not detected by ion chromatography because

of interferences in conductivity of the baseline promoted by the PMS salt precursor.

3.4 Determination of the main working oxidants

To confirm the main produced byproducts resulting from DMPO oxidation by $HO^{\bullet}$ radicals, UHPLC-QToF MS measurements were carried out as described in Text A3. An overview of the main detected DMPO byproducts can be seen upon analyses of the total and extracted ion chromatograms of Figure 3.23. Independently of the activation agent ($CoFe_2O_4$ and Co(II) ions) used, the obtained profile and detected species were the same and mainly due to $HO^{\bullet}$ addition reactions or H abstractions (typically promoted by $HO^{\bullet}$ as the $SO_4^{\bullet-}$ radicals are predominant under acidic conditions) [67-68], *i.e.*, DMPO/2OH, DMPO$^{\bullet}$/2OH, DMPO$^{\bullet}$/O, DMPO/OH, 2DMPO/-OH, 2DMPO/O-3H, 2DMPO/-H e DMPO/-3H. The MS/MS spectra of previous intermediates is showed in Figure A8. As expected, because of the low stability of DMPO-SO_4 [69] and solution pH, no intermediates resulting from $SO_4^{\bullet-}$ addition reactions were detected. The proposed fragmentation route of the main reported DMPO intermediate species can be seen in Figure A9, which is in agreement with that previously reported by Núñez-de la Rosa *et al.*, [70] considering the DMPO/OH, DMPO/2OH, DMPO$^{\bullet}$/2OH and DMPO$^{\bullet}$/O intermediates. Electron spin resonance measurements were also performed to elucidate DMPO-OH patterns, but they led to inconclusive results (see Figure A10).

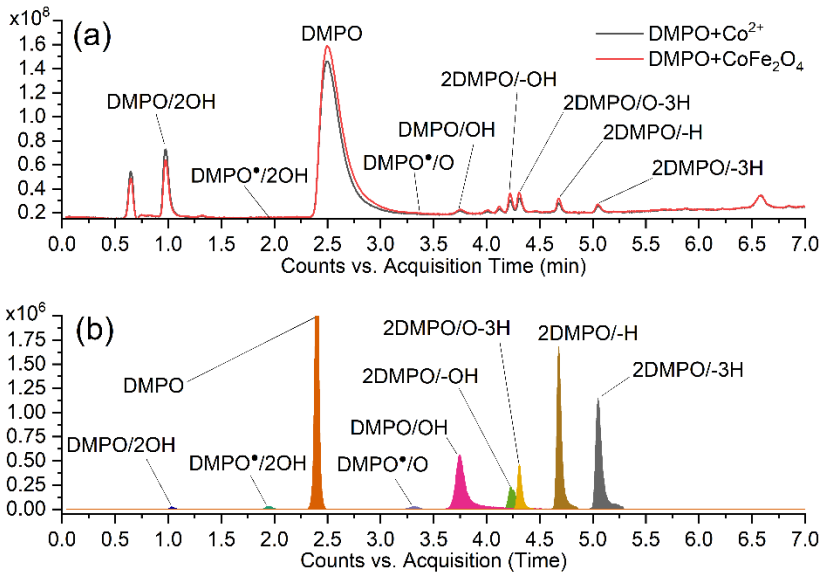

FIGURE 3.23 **a)** Total ion chromatogram (TIC) and **b)** Extracted ion chromatogram (EIC) of the main detected byproducts resulting from reaction between DMPO and oxygen radical species (produced by the reaction between $CoFe_2O_4$/Co(II) ions with PMS oxidant – see Text A4). CMF = cobalt magnetic ferrite ($CoFe_2O_4$ – SG 400 °C/1 h sample).

The scavenging experiments using isopropyl alcohol, tert-butyl alcohol, furfuryl alcohol, and L-histidine can be seen in Figure 3.24a. As expected, IMD oxidation was completely inhibited in the presence of isopropyl alcohol due to its prompt reaction with $HO^{\bullet}$ and $SO_4^{\bullet-}$ species (similar second-order rate constants: 2.8×10^9 L mol^{-1} s^{-1} for $HO^{\bullet}$ and 6×10^7 L mol^{-1} s^{-1} for $SO_4^{\bullet-}$) [71]. However, when tert-butyl alcohol was used, commonly known as a more selective scavenger for $HO^{\bullet}$ radical than $SO_4^{\bullet-}$ (second-order rate constant of 3.8 – 7.6×10^8 L mol^{-1} s^{-1}, compared to 4 – 9.1×10^5 L mol^{-1} s^{-1} for the reaction with the $SO_4^{\bullet-}$ radical – due to the faster hydrogen abstraction) [71], IMD was completely oxidized. Clearly, that behavior suggests that $HO^{\bullet}$ and $SO_4^{\bullet-}$ radicals participate in the IMD oxidation. When analyzing the deleterious effects of furfuryl alcohol (1.2×10^8 L mol^{-1} s^{-1} for the reaction with PMS) [72] and L-histidine (2 – 3×10^{10} L mol^{-1} s^{-1}) [73] on IMD oxidation, the role of $^1O_2$ is readily corroborated. To get further evidence on the production of $^1O_2$ since controversy

on the use of furfuryl alcohol as scavenger exists [74-75], experiments were carried out using ABDA, which is a specific compound to react with $^1O_2$ [55] as can be seen in Figures 3.24b through 3.24e. For both tested processes, *i.e.*, using $CoFe_2O_4$ (Figures 3.24b and c) and Co(II) ions (Figures 3.24d and e), the UV vis signal of ABDA was depleted after 5 min reaction, implying a prompt addition of $^1O_2$ compound to the intermediate aromatic ring of ABDA (see Figure 3.24f) and with cessation of the π-conjugated system. The role of $HO^{\bullet}$ and $SO_4^{\bullet-}$ was eliminated by conducting the same measurements in the presence of methanol (0.1 M). In addition to this, a significant increase in the level of dissolved oxygen (see Figure 3.25) was observed. No side reactions between PMS and ABDA were observed (see Figure 3.26). Thus, considering the reported tests, IMD oxidation by PMS activation using $CoFe_2O_4$ and Co(II) ions led to radical ($HO^{\bullet}$ and $SO_4^{\bullet-}$) and non-radical ($^1O_2$) species.

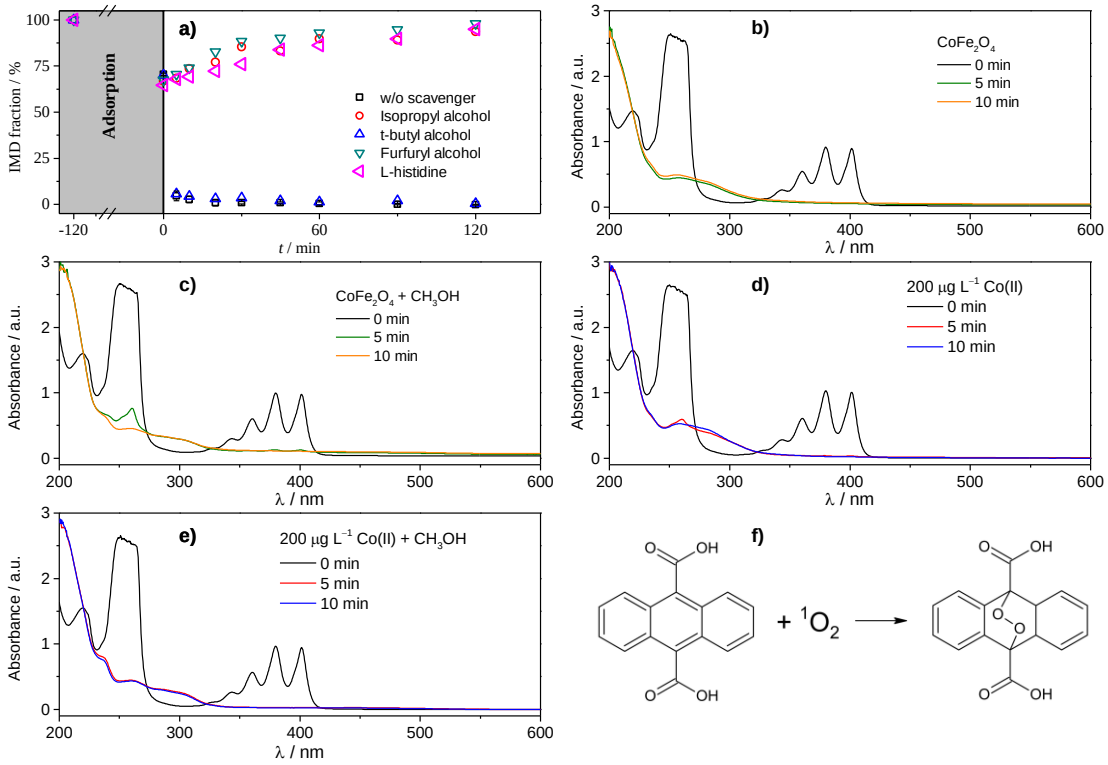

FIGURE 3.24 **a)** Remaining fraction of IMD (IMD fraction) as a function of treatment time (t) using distinct compounds (isopropyl alcohol, t-butyl alcohol, furfuryl alcohol, and L-histidine) as scavengers and evolution of UV vis spectra for the 9,10-anthracenediyl-bis(methylene)dimalonic acid (ABDA) compound using the CMF compound (in the presence and absence of methanol – see **b** and **c**, respectively) and Co(II) ions (in the presence and absence of methanol – see **d** and **e**, respectively) to activate peroxymonosulfate without imidacloprid, and **f)** the specific reaction between ABDA and $^1O_2$. **Conditions: a)** 0.125 g L^{-1} CMF (SG 400 ºC/1 h sample), 500 μM PMS, pH 7.0, 10 mM KH_2PO_4, 150 mL of treating solution with 50 mg L^{-1} IMD at 25 ºC and **b)** through **e)** pH ~7 and without buffer – see Text A4 for further details.

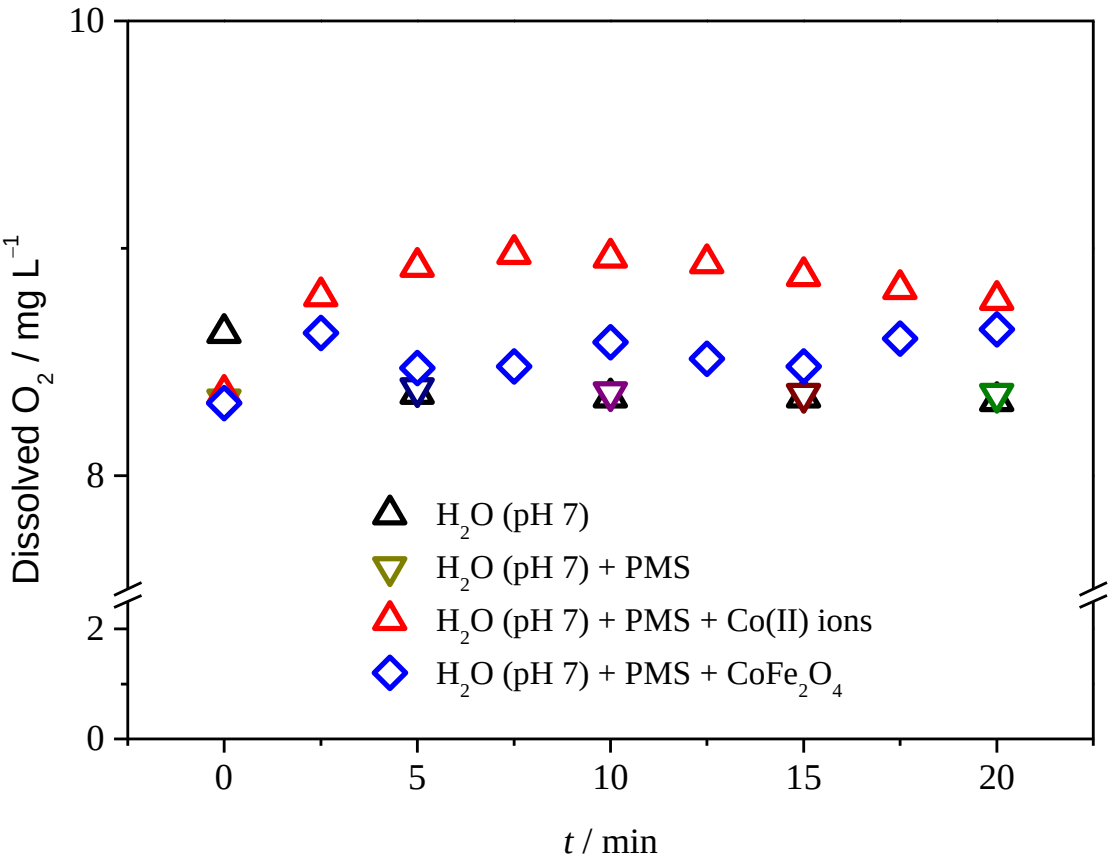

FIGURE 3.25 Evolution of dissolved oxygen as a function of time (*t*) using CMF nanoparticles (0.125 g L^{-1} of the SG 400 ºC/1 h sample) and 200 µg L^{-1} of Co(II) in the presence of PMS (500 µM). **Conditions:** No IMD addition, pH 7.0, 10 mM KH_2PO_4 at 25 °C.

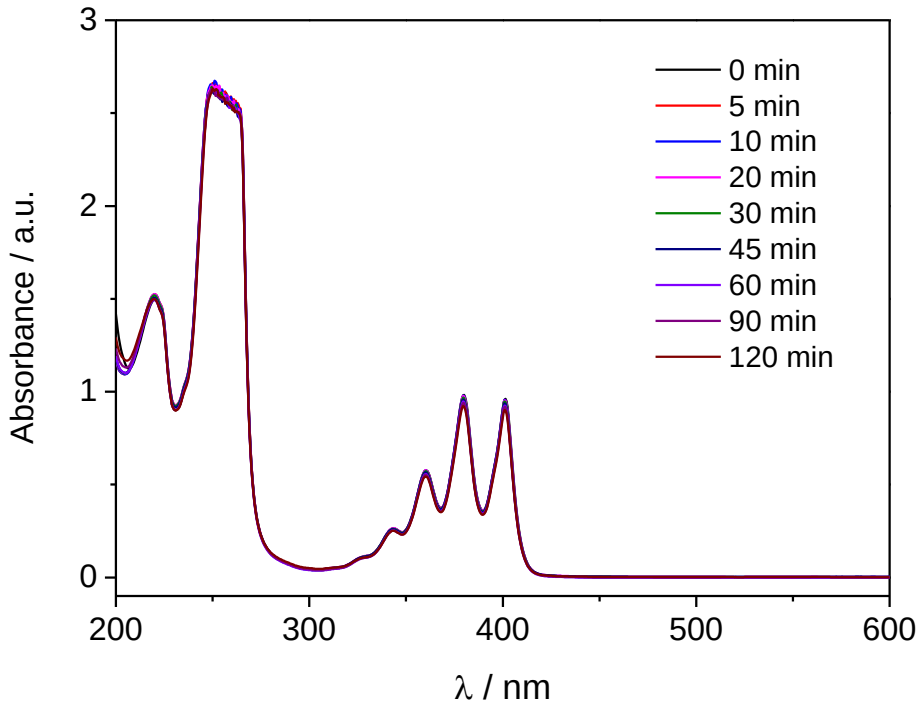

FIGURE 3.26 Evolution of the UV vis spectra for the 9,10-anthracenediyl-bis(methylene)dimalonic acid (ABDA) compound in the presence of PMS (500 µM) and without CMF or Co(II) ions. **Conditions:** No IMD addition, pH ~7 and without buffer – see Text A4 for further details.

3.5 Recycling test, time evolution changes of the CMF compound and proposed PMS activation mechanism

Five consecutive tests were carried out using the SG 400 ºC/1 h compound in the optimized conditions (0.125 g L^{-1} catalyst, 500 µM PMS and pH 7.0) as shown in Figure 3.27. As expected and due to leaching of Co(II) ions, the performance of the SG 400 ºC/1 h compound was not altered during consecutive experiments. The average mass percentage recovery for the recycling test remained close to 69% (see values on Table A10 for each experiment), when using a neodymium magnet.

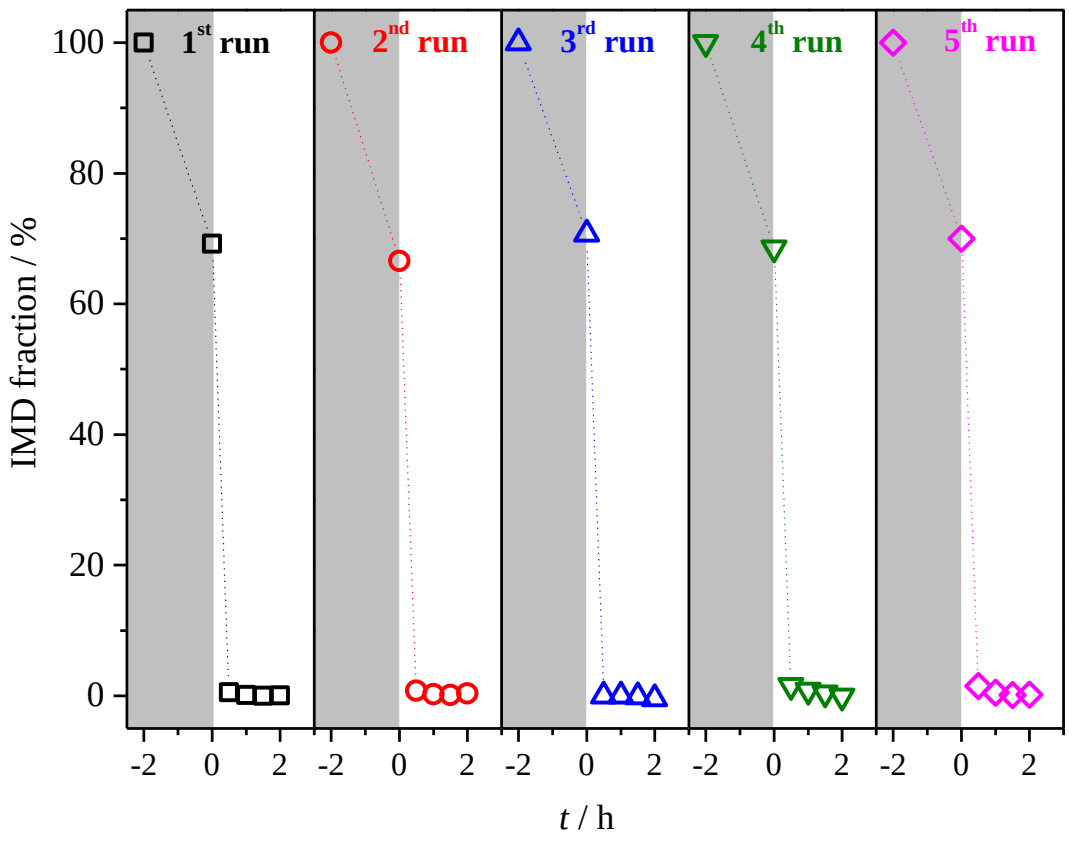

FIGURE 3.27 Remaining fraction of IMD (IMD fraction) as a function of treatment time (*t*) using CMF (cobalt magnetic ferrite) prepared by the sol-gel method and thermally treated at 400 ºC during 1 h (SG 400 ºC/1 h) for the recycling test. **Conditions:** 0.125 g L^{-1} CMF, 50 mg L^{-1} IMD, 500 µM PMS, pH 7.0, 10 mM KH_2PO_4, 1000 mL of treating solution at 25 °C. All experiments were carried out in the dark.

To verify possible modifications on the crystalline integrity, surface morphology, surface chemical groups and charge transfer resistance of the CMF compounds, TEM, XRD, XPS, and electrochemical impedance measurements were carried out in all samples after their use in the IMD oxidation. The studied powders resulted from the experiments reported in Figure 3.12. As can be seen in Figures 3.28a and 3.28b, no structural (see Figure 3.29 for the Cpt samples) or morphological changes (similar particle sizes – see Table A5 and Figure 3.28a for the histogram) were observed after the *in situ* chemical activation of PMS and degradation of the IMD insecticide.

Concerning the XPS, used to analyze the evolution of near-surface layer, no pronounced changes (see Figure 3.28c for the O 1s) were observed as shown in the deconvoluted high-resolution spectra of Figures A11 to A14. To simplify the visualization of XPS results, the evolution of the peak area percentage of the surface chemical states was compiled in bar graphs and displayed in Figures 3.30 to 3.32. The main differences observed between the as-prepared (AsP) and used (Us) samples are: *i*) appearance of K 2p peaks on the C 1s spectra for the Cpt samples after their use, a contamination which comes from the PMS salt (K^+ ion source); *ii*) an increase in hydroxyl groups, as observed in the O 1s, Co $2p_{3/2}$, and Fe $2p_{3/2}$ spectra, and a decrease in the lattice oxygen (O 1s O-Metal peak at ~530 eV) observed for the SG samples due to the presence of oxygenated hydrocarbons, as reported by X. Li *et al.*, [48]; and *iii*) evident decrease of Co(II) (~780 eV) and Fe(III) (~711 eV) species for both SG and Cpt samples, indicating the occurrence of leaching of these species. The Fe(II) component exhibited a distinct behavior, namely a reduction in the SG samples with an increase in Cpt sample. The absence of IMD adsorption and its oxidized byproducts on the surface of the material were also confirmed before and after testing by FTIR measurements (data not shown). The spectra showed no changes before and after the reaction, indicating that the initially absorbed IMD molecules were transferred into the solution.

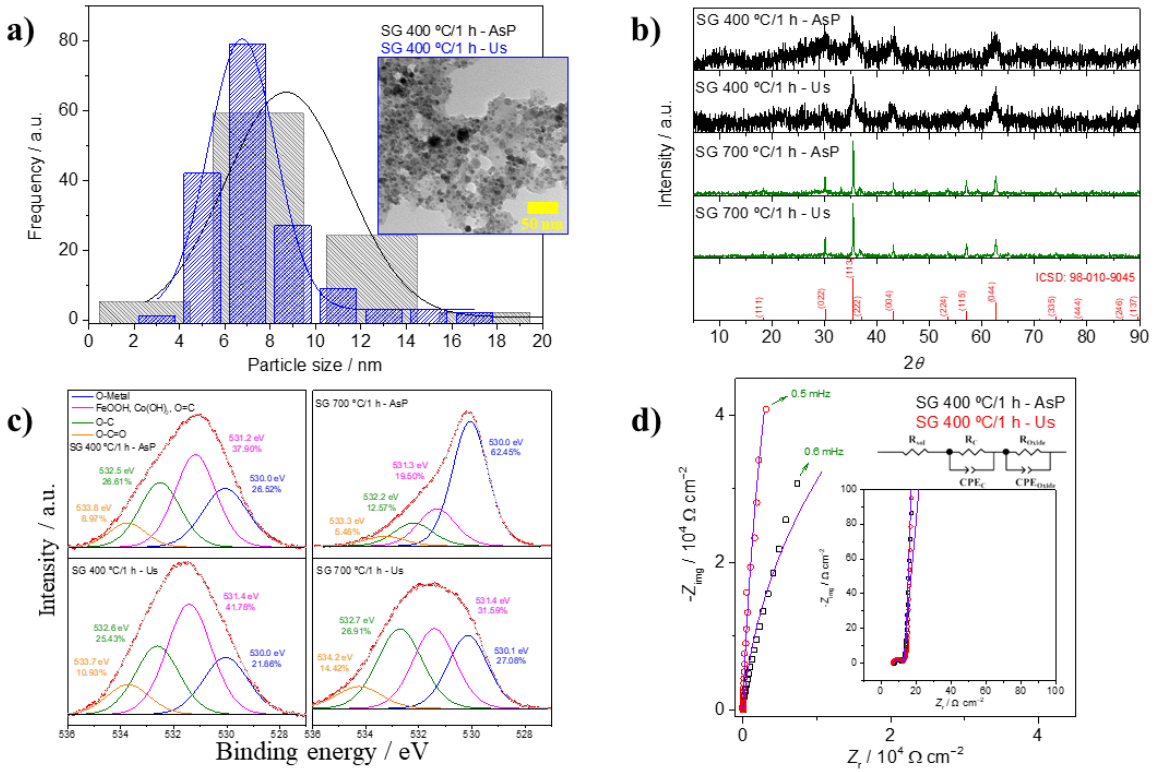

FIGURE 3.28 **a)** TEM and histogram of CMF nanoparticle size, **b)** X-ray diffraction (XRD) patterns, **c)** XPS spectra of O 1s, and **d)** EI complex plane for the as-prepared (AsP) and after use (Us) CMF synthesized by the sol-gel (SG) method and thermally treated at 400 °C and 700 °C for 1 h, *i.e.*, SG 400 °C/1 h and SG 700 °C/1 h (see inset).

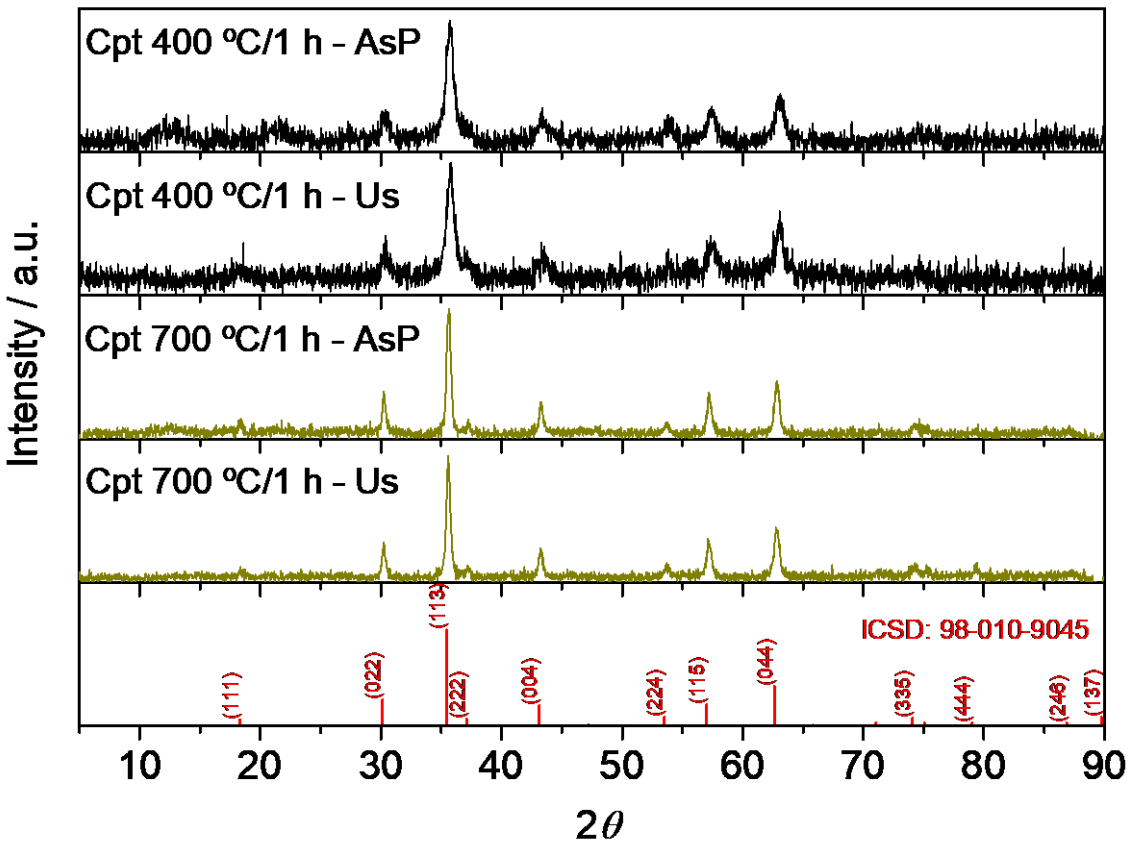

FIGURE 3.29 X-ray diffraction (XRD) patterns of the as-prepared (AsP) and after use (Us) $CoFe_2O_4$ magnetic ferrite synthesized by the co-precipitation (Cpt) method and thermally treated at 400 ºC or 700 ºC for 1 h, *i.e.*, Cpt 400 ºC/1 h and Cpt 700 ºC/1 h (see inset), respectively. Diffraction peaks were in accordance with the ICSD card Nº 98-010-9045.

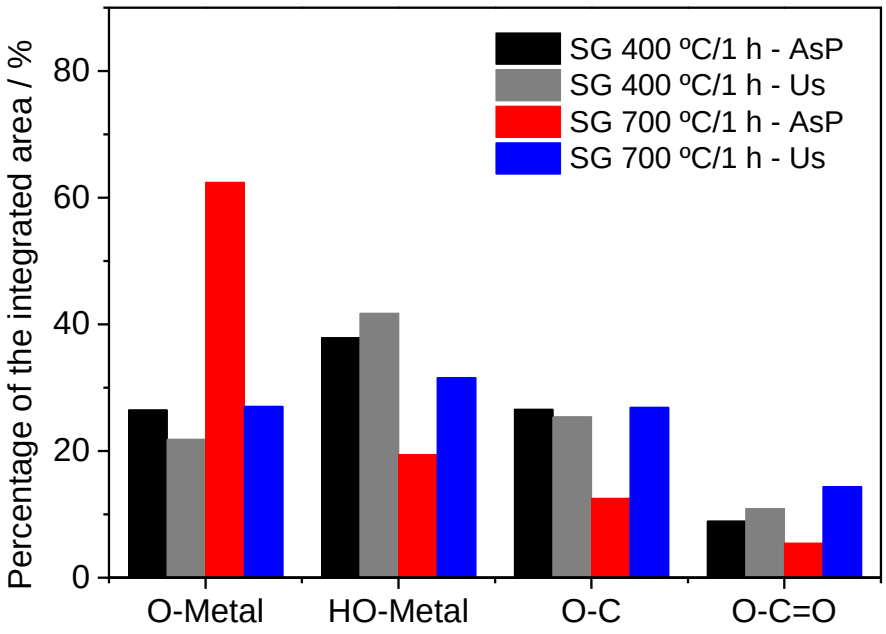

a)

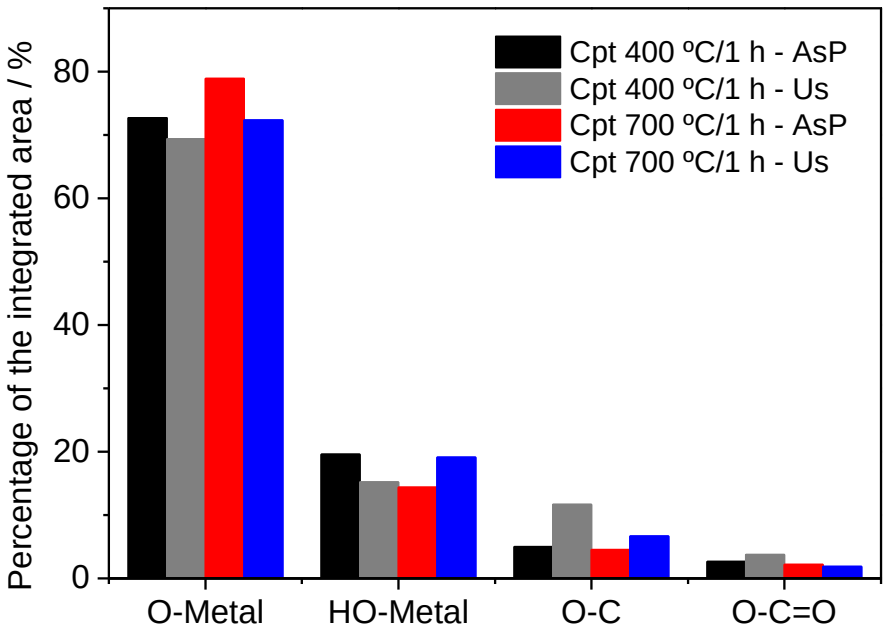

b)

FIGURE 3.30 Peak areas of the surface bonding states obtained from the O 1s spectra (see Figure A12) using the **a)** sol-gel (SG) and **b)** co-precipitation (Cpt) samples that were thermally treated at 400 ºC or 700 ºC for 1 h.

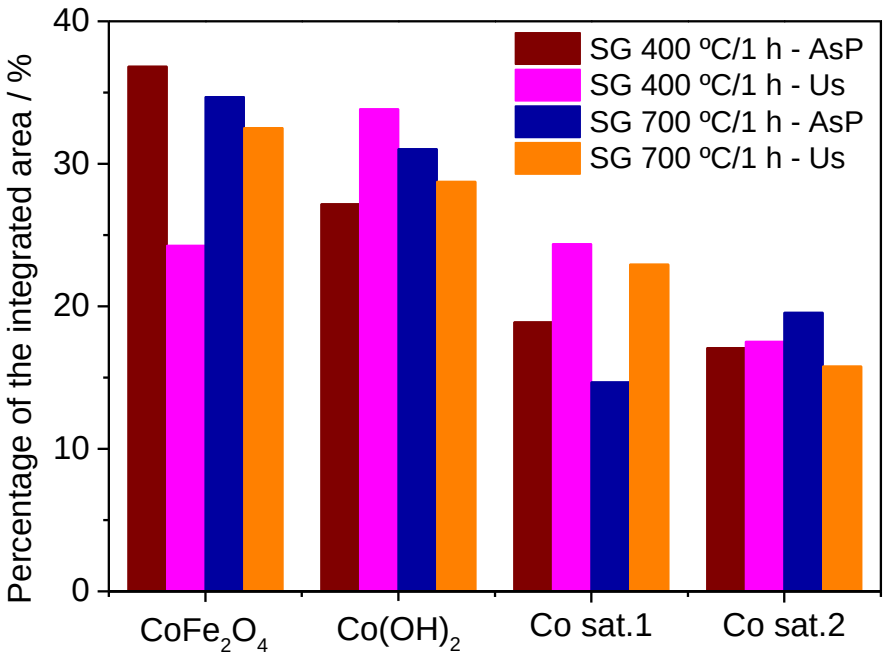

a)

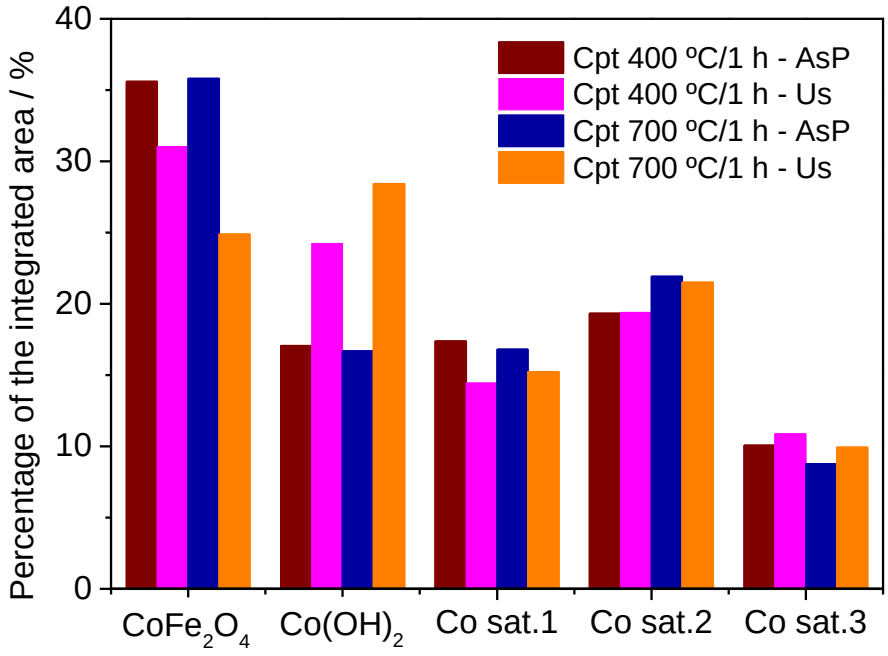

b)

FIGURE 3.31 Peak areas of the surface bonding states obtained from the Co $2p_{3/2}$ spectra (see Figure A13) using the **a)** sol-gel (SG) and **b)** co-precipitation (Cpt) samples that were thermally treated at 400 ºC or 700 ºC for 1 h.

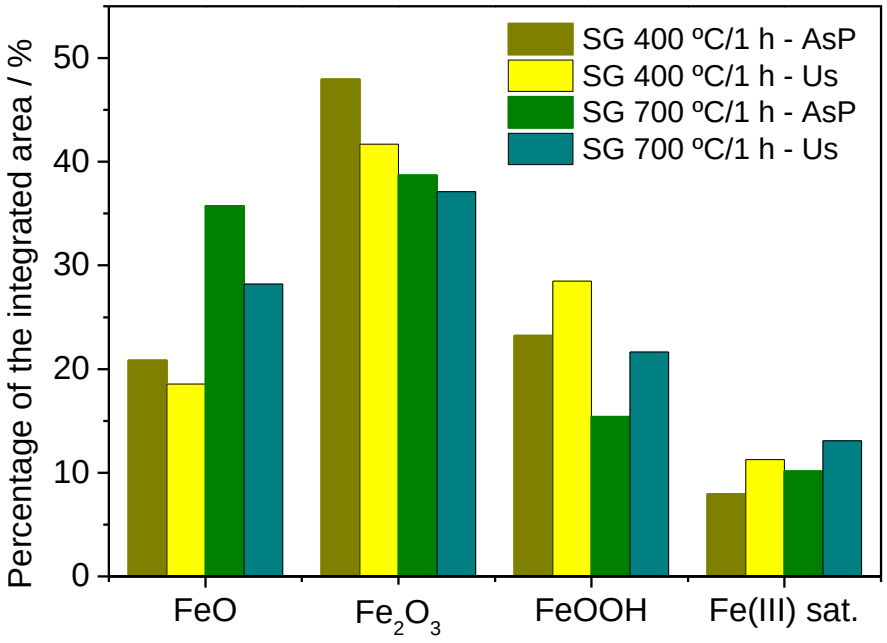

a)

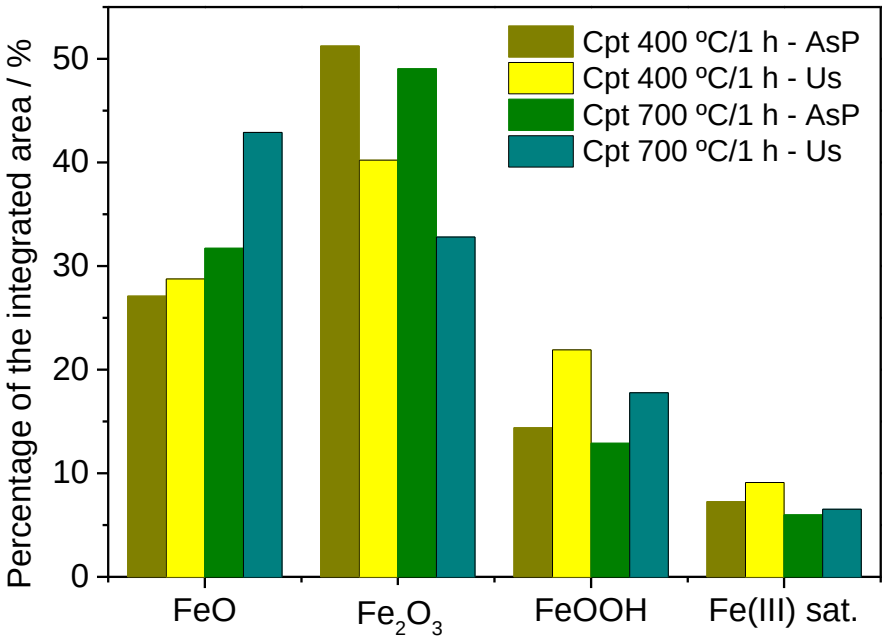

b)

FIGURE 3.32 Peak areas of the surface bonding states obtained from the Fe $2p_{3/2}$ spectra (see Figure A14) using the **a)** sol-gel (SG) and **b)** co-precipitation (Cpt) samples that were thermally treated at 400 ºC or 700 ºC for 1 h.

Considering the reported results on the role of Co(II) ions in the PMS activation and surface changes of the CMF compound, the following mechanism might occur: *i*) Co(II) species on the nanoparticle surface (≡Co(II)) are oxidized and leached (leaving an empty site ≡□) into the solution (Eq. 9) resulting in a homogeneous reaction (Eqs. 10 – 13) [76]; and *ii*) Fe(III) is reduced to Fe(II) (Eq. 14) that is possibly leached into the solution (Eq. 15). As previously discussed, $^1O_2$ was detected and could be produced according to Eq. 16. At neutral solutions (pH 7), the produced $SO_4^{\bullet-}$ radical might be readily converted to $HO^{\bullet}$ (Eq. 17), as detected during UHPLC-QToF MS measurements.

$$\equiv Co(II) + HSO_5^- \rightarrow \equiv\square + Co(III) + SO_4^{\bullet-} + OH^- \quad (9)$$

$$Co(III) + HSO_5^- \rightarrow Co(II) + SO_5^{\bullet-} + H^+ \quad (10)$$

$$Co(II) + H_2O \leftrightarrows CoOH^+ + H^+ \quad (11)$$

$$CoOH^+ + HSO_5^- \rightarrow CoO^+ + SO_4^{\bullet-} + H_2O \quad (12)$$

$$CoO^+ + 2H^+ \leftrightarrows Co(III) + H_2O \quad (13)$$

$$\equiv Fe(III) + HSO_5^- \rightarrow \equiv Fe(II) + SO_5^{\bullet-} + H^+ \quad (14)$$

$$\equiv Fe(II) + HSO_5^- \rightarrow \equiv\square + Fe(III) + SO_4^{\bullet-} + OH^- \quad (15)$$

$$2SO_5^{\bullet-} + H_2O \rightarrow 2HSO_4^- + 1.5\ {}^1O_2 \quad (16)$$

$$SO_4^{\bullet-} + H_2O \rightarrow SO_4^{2-} + HO^{\bullet} + H^+ \quad k[H_2O] < 1.0\times10^3\ L\ mol^{-1}\ s^{-1} \quad (17)$$

H. Li *et al.*, [60] reported that Co(II) ions can complex with PMS leading to Co(II)−$OOSO_3^-$ species (strongly pH dependent) prone to form Co(III) and $SO_4^{\bullet-}$ radical (Eq. 18). The use of a phosphate buffer solution can also result in complexation among PMS, Co(II), and $H_2PO_4^-$ (L) ions forming L−Co(II)−$OOSO_3^-$ of distinct reactivity [77]. However, in the present study, no differences in IMD oxidation were observed in the presence or absence of a buffered solution (except of increased PMS consumption) probably due to the amount of PMS used. The coupling between CMF and PMS was indirectly

observed during OCP measurements carried out using electrodes made with distinctly prepared CMF nanoparticles (see Figure A15). As can be apprehended from that figure, electrode potential increased continuously after PMS addition into solution (*i.e.*, oxidation through surface modification), without interferences from IMD.

$$Co(II) + HSO_5^- \rightarrow Co(II)–OOSO_3^- \rightarrow Co(III) + SO_4^{\bullet -} + OH^- \quad (18)$$

To access the evolution of the charge transfer resistance of the CMF oxide, electrochemical impedance measurements were carried out for the AsP and Us samples synthesized by the SG and Cpt methods. The results are shown in Figures A16 to A19. The equivalent circuit used to obtain the best fits of the experimental data was composed of the solution resistance (R_{sol}), carbon support charge transfer resistance (R_C) in parallel with constant phase elements CPE_C, and the oxide charge transfer resistance (R_{oxide}) in parallel with CPE_{Oxide}. Among these parameters, the values of R_{oxide} before and after testing are shown in Figure A20. An abrupt rise of the R_{oxide} values (see the slope variation at low frequencies, *i.e.*, 0.5 mHz, in Figure 3.28d for the SG samples) was observed after use for the SG 400 ºC/1 h sample (the other Us values also increased but were not determined due to a lack of fit). This behavior could be due to the increased hydroxyl groups on the solid surface [78], which, however, did not affect the oxidation performance of the CMF since the IMD oxidation reaction through PMS activation proceeded by the leached Co(II) ions (Eqs. 10 and 13). Surface hydroxylation can occur on defects of the particle surface, specially at oxygen vacancies, that may lead to important surface reactions [79-81] or at metal sites (Eq. 19) as shown in the work of Lyu *et al.*, [82].

$$\equiv Metal(III/II) + H_2O \rightarrow \equiv Metal(III/II)–OH^- + H^+ \quad (19)$$

Finally, the use of CMF resulted in the dissolution of distinct quantities of Co(II) and Fe(III) ions. Among these ions, Co(II) demonstrated superior effectiveness over the solid material in activating PMS, leading to the generation of both radical and non-radical species.

CONCLUSIONS

Nanometric $CoFe_2O_4$ magnetic ferrite was successfully synthesized and characterized using the sol-gel and co-precipitation methods to activate peroxymonosulfate (PMS) oxidant under neutral conditions. After optimization of the catalyst load and PMS concentration, IMD oxidation rate and levels remained constant showing complete oxidation of IMD within 30 min independently of the preparation procedure. Further experiments showed that this was due to Co(II) ion leaching from the catalyst particles. Efforts to minimize ion leaching were unsuccessful since Co(II) ion concentrations as low as 20 μg L^{-1} were sufficient to activate PMS by the Co(II)/Co(III) redox couple in the presence or absence of a phosphate buffer at pH 7. The effect of Fe(III) ions on PMS activation was observed, but their impact was underestimated in the presence of Co(II) ions. Future studies should therefore apply consistent approaches to determine the effect of ion leaching from any solid oxide catalyst to find out the role or contribution of homogeneous and heterogeneous reactions. In addition, pH monitoring and correction are recommended as well as the correct choice of concentration between buffer (if used) and PMS.

PMS activation by $CoFe_2O_4$ and/or Co(II) ions led to the production of radicals ($HO^{\bullet}$ and $SO_4^{\bullet-}$) and non-radical ($^1O_2$) species as detected and confirmed through UHPLC-QToF MS measurements using DMPO as spin probe and scavenging experiments, particularly 9,10-anthracenediyl-bis(methylene) dimalonic acid for $^1O_2$. The latter led to high oxidation levels even in a complex medium such as simulated municipal wastewater. Concerning the oxidation byproducts of IMD, only five intermediates derived from hydroxylation addition reactions on the imidazolidine ring were detected along with short chain carboxylic acids. Considering the structural and electrochemical analysis carried out on the assayed $CoFe_2O_4$ samples, no significant changes were observed except a decrease in Co(II) and Fe(III) phases and an increase in the oxide charge transfer

resistance. These findings confirm the unique role of $CoFe_2O_4$ nanoparticles as efficient Co(II) ion source.

REFERENCES

1. World Health Organization (WHO). “Drinking-water”. Available in: https://www.who.int/news-room/fact-sheets/detail/drinking-water. Accessed on 12/10/2023.

2. United Nations (UN). “World Population Prospects 2022”. Available in: https://brasil.un.org/pt-br/189756-popula %C3%A 7% C3% A 3o-mundial-chegar%C3%A1-8-bilh%C3%B5es-em-novembro-de-2022. Accessed on 12/11/2023.

3. SAUVÉ, S. & DESROSIERS, M. “A review of what is an emerging contaminant”. Chem. Central J., **8**: 1, 2014.

4. MANZETTI, S.; VANDERSPOEL, E.R. & VANDERSPOEL, D. “Chemical properties, environmental fate, and degradation of seven classes of pollutants”. Chem. Res. Toxicol., **27**: 713, 2014.

5. BILA, D.M. & DEZOTTI, M. “Desreguladores endócrinos no meio ambiente: efeitos e conseqüências”. Quim. Nova, 30 (3): 651, 2007.

6. JURADO, A.; WALTHER, M. & DÍAZ-CRUZ, M.S. “Occurrence, fate and environmental risk assessment of the organic microcontaminants included in the Watch Lists set by EU Decisions 2015/495 and 2018/840 in the groundwater of Spain”. Sci. Total Environ., **663**: 285, 2019.

7. SHARMA, B.M.; BEČANOVÁ, J.; SCHERINGER, M.; SHARMA, A.; BHARAT, G.K.; WHITEHEAD, P.G.; KLÁNOVÁ, J. & NIZZETTO, L. “Health and ecological risk assessment of emerging contaminants (pharmaceuticals, personal care products, and artificial sweeteners) in surface and groundwater (drinking water) in the Ganges River Basin, India”. Sci. Total Environ., **646**: 1459, 2019.

8. SOUSA, J.C.G.; RIBEIRO, A.R.; BARBOSA, M.O.; RIBEIRO, C.; TIRITAN, M.E.; PEREIRA, M.F.R. & SILVA, A.M.T. “Monitoring of the 17 EU Watch List contaminants of emerging concern in the Ave and the Sousa Rivers”. Sci. Total Environ., **649**: 1083, 2019.

9. SIERRA, I.; RODRÍGUEZ, M.; FACCIO, R.; CARRIZO, D.; FORNARO, L. & PÉREZ-PARADA, A. “Identification of microplastics in wastewater samples by means of polarized light optical microscopy”. Environ. Sci. Pollut. Res., **27**: 7409, 2020.

10. CONLEY, K.; CLUM, A.; DEEPE, J.; LANE, H. & BECKINGHAM, B. “Wastewater treatment plants as a source of microplastics to an urban estuary: Removal efficiencies and loading per capita over one year”. Water Res. X, **3**: 100030, 2019.

11. HOUTMAN, C.J.; KROESBERGEN, J.; LEKKERKERKER-TEUNISSEN, K. & VAN DER HOEK, J.P. “Human health risk assessment of the mixture of pharmaceuticals in Dutch drinking water and its sources based on frequent monitoring data”. Sci. Total. Environ., **496**: 54, 2014.

12. SCHWAB, B.W.; HAYES, E.P.; FIORI, J.M.; MASTROCCO, F.J.; RODEN, N.M.; CRAGIN, D.; MEYERHOFF, R.D.; D’ACO, V.J. & ANDERSON, P.D. “Human pharmaceuticals in US surface waters: A human health risk assessment”. Regul. Toxicol. Pharmacol., **42**: 296, 2005.

13. LEE, H.-J.; KIM, K.Y.; HAMM, S.-Y.; KIM, M.; KIM, H.K. & OH, J.-E. “Occurrence and distribution of pharmaceutical and personal care products, artificial sweeteners, and pesticides in groundwater from an agricultural area in Korea”. Sci. Total Environ., **659**: 168, 2019.

14. ARCHER, E.; VOLSCHENK, M.; BROCKER, L. & WOLFAARDT, G.M. “A two-year study of emerging micro-pollutants and drugs of abuse in two Western Cape wastewater treatment works (South Africa)”. Chemosphere, **285**: 131460, 2021.

15. DEERE, J.R.; MOORE, S.; FERREY, M.; JANKOWSKI, M.D.; PRIMUS, A.; CONVERTINO, M.; SERVADIO, J.L.; PHELPS, N.B.D.; HAMILTON, M.C.; CHENAUX-IBRAHIM, Y.; TRAVIS, D.A. & WOLF, T.M. "Occurrence of contaminants of emerging concern in aquatic ecosystems utilized by Minnesota tribal communities". Sci. Total Environ., **724**: 138057, 2020.

16. MONTAGNER, C.C.; SODRÉ, F.F.; ACAYABA, R.D.; VIDAL, C.; CAMPESTRINI, I.; LOCATELLI, M.A.; PESCARA, I.C.; ALBUQUERQUE, A.F.; UMBUZEIRO, G.A. & JARDIM, W.F. "Ten Years-Snapshot of the Occurrence of Emerging Contaminants in Drinking, Surface and Ground Waters and Wastewaters from São Paulo State, Brazil". J. Braz. Chem. Soc., 30 (3): 614, 2019.

17. PERIN, M.; DALLEGRAVE, A.; BARNET, L.S.; MENEGHINI, L.Z.; GOMES, A.A. & PIZZOLATO, T.M. "Pharmaceuticals, pesticides and metals/metalloids in Lake Guaíba in Southern Brazil: Spatial and temporal evaluation and a chemometrics approach". Sci. Total Environ., **793**: 148561, 2021.

18. BLACKBEARD, J.; LLOYD, J.; MAGYAR, M.; MIEOG, J.; LINDEN, K.G. & LESTER, Y. "Demonstrating organic contaminant removal in an ozone-based water reuse process at full scale". Environ. Sci.: Water Res. Technol., **2**: 213, 2016.

19. SUBEDI, B.; LEE, S.; MOON, H.-B. & KANNAN, K. "Emission of artificial sweeteners, select pharmaceuticals, and personal care products through sewage sludge from wastewater treatment plants in Korea". Environ. Int., **68**: 33, 2014.

20. DÍAZ-GARDUÑO, B.; PINTADO-HERRERA, M.G.; BIEL-MAESO, M.; RUEDA-MÁRQUEZ, J.J.; LARA-MARTÍN, P.A.; PERALES, J.A.; MANZANO, M.A.; GARRIDO-PÉREZ, C. & MARTÍN-DÍAZ, M.L. "Environmental risk assessment of effluents as a whole emerging contaminant:

Efficiency of alternative tertiary treatments for wastewater depuration". Water Res., **119**: 136, 2017.

21. LIN, L.; YANG, H. & XU, X. "Effects of Water Pollution on Human Health and Disease Heterogeneity: A Review". Front. Environ. Sci., **10**: 880246, 2022.

22. ZAHOOR, I. & MUSHTAQ, A. "Water Pollution from Agricultural Activities: A Critical Global Review". Int. J. Chem. Biochem. Sci., 23 (1): 164, 2023.

23. HAIROM, N.H.H.; SOON, C.F.; MOHAMED, R.M.S.R.; MORSIN, M.; ZAINAL, N.; NAYAN, N.; ZULKIFLI, C.Z. & HARUN, N.H. "A review of nanotechnological applications to detect and control surface water pollution". Environ. Technol. & Innov., **24**: 102032, 2021.

24. RADJENOVIC, J. & SEDLAK, D.L. "Challenges and opportunities for electrochemical processes as next-generation technologies for the treatment of contaminated water". Environ. Sci. Technol., **49**: 11292, 2015.

25. Nações Unidas Brasil. "Objetivos de Desenvolvimento Sustentável: Água potável e saneamento". Available in: https://brasil.un.org/pt-br/sdgs/6. Accessed on 12/13/2023.

26. SCHWARZENBACH, R.P.; ESCHER, B.I.; FENNER, K.; HOFSTETTER, T.B.; JOHNSON, C.A.; GUNTEN, U.V. & WEHRLI, B. "The challenge of micropollutants in aquatic systems". Science, **313**: 1072, 2006.

27. MIKLOS, D.B.; REMY, C.; JEKEL, M.; LINDEN, K.G.; DREWES, J.E. & HÜBNER, U. "Evaluation of advanced oxidation processes for water and wastewater treatment-A critical review". Water Res., **139**: 118, 2018.

28. HODGES, B.C.; CATES, E.L. & KIM, J.-H. "Challenges and prospects of advanced oxidation water treatment processes using catalytic nanomaterials". Nat. Nanotechnol., **13**: 642, 2018.

29. HASSANI, A.; SCARIA, J.; GHANBARI, F. & NIDHEESH, P.V. “Sulfate radicals-based advanced oxidation processes for the degradation of pharmaceuticals and personal care products: A review on relevant activation mechanisms, performance, and perspectives”. Environ. Res., **217**: 114789, 2023.

30. LEE, J.; GUNTEN, U.V. & KIM, J.-H. “Persulfate-Based Advanced Oxidation: Critical Assessment of Opportunities and Roadblocks”. Environ. Sci. Technol., **54**: 3064, 2020.

31. BRILLAS, E. “Progress of antibiotics removal from synthetic and real waters and wastewaters by persulfate-based advanced oxidation processes”. J. Environ. Chem. Eng., **11**: 111303, 2023.

32. YUAN, Z.; SUI, M.; YUAN, B.; LI, P.; WANG, J.; QIN, J. & XU, G. “Degradation of ibuprofen using ozone combined with peroxymonosulfate”. Environ. Sci. Water Res. Technol., **3**, 960, 2017.

33. NIE, M.; YAN, C.; LI, M.; WANG, X.; BI, W. & DONG, W. “Degradation of chloramphenicol by persulfate activated by Fe^{2+} and zerovalent iron”. Chem. Eng. J., **279**: 507, 2015.

34. POURAN, S.R.; RAMAN, A.A.A. & DAUD, W.M.A.W. “Review on the application of modified iron oxides as heterogeneous catalysts in Fenton reactions”. J. Clean. Prod., **64**: 24, 2014.

35. SUN, P.; LIU, H.; FENG, M.; GUO, L.; ZHAI, Z.; FANG, Y.; ZHANG, X. & SHARMA, V.K. “Nitrogen-sulfur co-doped industrial graphene as an efficient peroxymonosulfate activator: Singlet oxygen-dominated catalytic degradation of organic contaminants”. Applied Catalysis B: Environ., **251**: 335, 2019.

36. GAO, Y.; CHEN, Z.; ZHU, Y.; LI, T. & HU, C. “New Insights into the Generation of Singlet Oxygen in the Metal-Free Peroxymonosulfate Activation Process: Important Role of Electron-Deficient Carbon Atoms”. Environ. Sci. Technol., **54**: 1232, 2020.

37. LIU, Z.; DUAN, X.; SARMAH, A.K.; ZHAO, X.; XIN REN, X. & SUN, B. “A novel 3-dimensional graphene-based cobalt-manganese bimetallic layered double hydroxide: Formation mechanism and performance in photo-assisted permonosulfate-activated degradation of sulfamethoxazole in aqueous solution”. Environ. Pollution, **336**: 122397, 2023.

38. KAKAVANDI, B.; ALAVI, S.; GHANBARI, F. & AHMADI, M. “Bisphenol A degradation by peroxymonosulfate photo-activation coupled with carbon-based cobalt ferrite nanocomposite: Performance, upgrading synergy and mechanistic pathway”. Chemosphere, **287**: 132024, 2022.

39. LI, Y.; ZHU, W.; GUO, Q.; WANG, X.; ZHANG, L.; GAO, X. & LUO, Y. “Highly efficient degradation of sulfamethoxazole (SMX) by activating peroxymonosulfate (PMS) with $CoFe_2O_4$ in a wide pH range”. Sep. Purif. Technol., **276**: 119403, 2021.

40. FONTECHA-CÁMARA, M.A.; MORENO-CASTILLA, C.; LÓPEZ-RAMÓN, M.V. & ÁLVAREZ, M.A. “Mixed iron oxides as Fenton catalysts for gallic acid removal from aqueous solutions”. Applied Catalysis B: Environ., **196**: 207, 2016.

41. ANIPSITAKIS, G.P. & DIONYSIOU, D.D. “Radical generation by the interaction of transition metals with common oxidants”. Environ. Sci. Technol., **38**: 3705, 2004.

42. ZHOU, Y.; ZHANG, Y. & HU, X. “Synergistic coupling Co_3Fe_7 alloy and $CoFe_2O_4$ spinel for highly efficient removal of 2,4-dichlorophenol by activating peroximonosulfate”. Chemosphere, **242**: 125244, 2020.

43. DU, Y.; MA, W.; LIU, P.; ZOU, B. & MA, J. “Magnetic $CoFe_2O_4$ nanoparticles supported on titanate nanotubes ($CoFe_2O_4$/TNTs) as a novel heterogeneous catalyst for peroxymonosulfate activation and degradation of organic pollutants”. J. Hazard. Mater., **308**: 58, 2016.

44. YU, X.-J., QU, J.; YUAN, Z.; MIN, P.; HAO, S.-M.; ZHU, Z.-S.; LI, X.; YANG, D. & YU, Z.-Z. “Anisotropic $CoFe_2O_4$@Graphene hybrid aerogels with high flux and excellent stability as building blocks for rapid catalytic degradation of organic contaminants in a flow-type setup”. ACS Appl. Mater. Interfaces, **11**: 34222, 2019.

45. XU, M.; LI, J.; YAN, Y.; ZHAO, X.; YAN, J.; ZHANG, Y.; LAI, B.; CHEN, X. & SONG, L. “Catalytic degradation of sulfamethoxazole through peroxymonosulfate activated with expanded graphite loaded $CoFe_2O_4$ particles”. Chem. Eng. J., 369: **403**, 2019.

46. GAO, D.; LU, Y.; CHEN, Y.; BAO, M. & XU, N. “Novel $CoFe_2P_x$ derived from $CoFe_2O_4$ for efficient peroxymonosulfate activation: Switching the reaction route and suppressing metal leaching”. Appl. Catal. B Environ., **309**: 121234, 2022.

47. MENG, F.; YU, L.; SONG, B.; ZHAO, Y.; ZHI, Z.; LIN, C. & SONG, M. “Insights into the mechanism of redox pairs and oxygen vacancies of Fe_2O_3@$CoFe_2O_4$ hybrids for efficient refractory organic pollutants degradation”. Chemosphere, **291**: 133069, 2022.

48. LI, X.; LIU, Z.; ZHU, Y.; SONG, L.; DONG, Z.; NIU, S. & LYU, C. “Facile synthesis and synergistic mechanism of $CoFe_2O_4$@three-dimensional graphene aerogels towards peroxymonosulfate activation for highly efficient degradation of recalcitrant organic pollutants”. Sci. Total Environ.,**749**: 141466, 2020.

49. ZHU, S.; WANG, Z.; YE, C.; DENG, J.; MA, X.; XU, Y.; WANG, L.; TANG, Z.; LUO, H. & LI, X. “Magnetic Co/Fe nanocomposites derived from ferric sludge as an efficient peroxymonosulfate catalyst for ciprofloxacin degradation”. Chem. Eng. J., **432**: 134180, 2022.

50. LIU, B.; SONG, W.; WU, H.; XU, Y.; SUN, Y.; YU, Y.; ZHENG, H. & WAN, S. “Enhanced oxidative degradation of norfloxacin using peroxymonosulfate

activated by oily sludge carbon-based nanoparticles $CoFe_2O_4$/OSC". Chem. Eng. J., **400**: 125947, 2020.

51. SRINIVASA RAO, K., RANGA NAYAKULU, S.V., CHAITANYA VARMA, M., CHOUDARY, G.S.V.R.K. & RAO, K.H. "Controlled phase evolution and the occurrence of single domain $CoFe_2O_4$ nanoparticles synthesized by PVA assisted sol-gel method". J. Magn. Magn. Mater., **451**: 602, 2018.

52. BASAK, M.; RAHMAN, MD.L.; AHMED, MD.F.; BISWAS, B. & SHARMIN, N. "Calcination effect on structural, morphological and magnetic properties of nano-sized $CoFe_2O_4$ developed by a simple co-precipitation technique". Mater. Chem. Phys., **264**: 124442, 2021.

53. LI, X.; ZHAO, Z.; LI, H. & QIAN, J. "Degradation of organic contaminants in the $CoFe_2O_4$/peroxymonosulfate process: The overlooked role of Co(II)-PMS complex". Chem. Eng. J. Adv., **8**:100143, 2021.

54. LIANG, C.; HUANG, C.-F.; MOHANTY, N. & KURAKALVA, R.M. "A rapid spectrophotometric determination of persulfate anion in ISCO". Chemosphere, **73**: 1540, 2008.

55. ENTRADAS, T.; WALDRON, S. & VOLK, M. "The detection sensitivity of commonly used singlet oxygen probes in aqueous environments", J. Photochem. Photobiol. B., **204**: 111787, 2020.

56. POWELL, C., "X-ray photoelectron spectroscopy database XPS, Version 4.1". NIST standard reference database 20, 1989.

57. NAJJAR, W.; AZABOU, S.; SAYADI, S. & GHORBEL, A. "Catalytic wet peroxide photo-oxidation of phenolic olive oil mill wastewater contaminants: Part I. Reactivity of tyrosol over (Al–Fe) PILC". Appl. Catal. B Environ., **74**: 11, 2007.

58. ZHANG, T.; ZHU, H. & CROUÉ, J.-P. "Production of Sulfate Radical from Peroxymonosulfate Induced by a Magnetically Separable $CuFe_2O_4$ Spinel in

Water: Efficiency, Stability, and Mechanism". Environ. Sci. Technol., **47**: 2784, 2013.

59. HU, P. & LONG, M. "Cobalt-catalyzed sulfate radical-based advanced oxidation: a review on heterogeneous catalysts and applications". Appl. Catal. B Environ., **181**: 103, 2016.

60. LI, H.; ZHAO, Z.; QIAN, J. & PAN, B. "Are free radicals the primary reactive species in Co(II)-mediated activation of peroxymonosulfate? New evidence for the role of the Co(II)–peroxymonosulfate complex". Environ. Sci. Technol., **55**: 6397, 2021.

61. CHOI, J.; LEE, H.; CHOI, Y.; KIM, S.; LEE, S.; LEE, S.; CHOI, W. & LEE, J. "Heterogeneous photocatalytic treatment of pharmaceutical micropollutants: Effects of wastewater effluent matrix and catalyst modifications". Appl. Catal. B Environ., **147**: 8, 2014.

62. LEE, Y. & GUNTEN, U.V. "Oxidative transformation of micropollutants during municipal wastewater treatment: comparison of kinetic aspects of selective (chlorine, chlorine dioxide, ferrate VI, and ozone) and non-selective oxidants (hydroxyl radical). Emerg. Contam. Water Occur. Fate Remov. Assess. Water Cycle Wastewater Drink". Water Res., **44**: 555, 2010.

63. BOURGIN, M.; VIOLLEAU, F.; DEBRAUWER, L. & ALBET, J. "Ozonation of imidacloprid in aqueous solutions: reaction monitoring and identification of degradation products". J. Hazard. Mater., **190**: 60, 2011.

64. BAGHIRZADE, B.S.; YETIS, U. & DILEK, F.B. "Imidacloprid elimination by O_3 and O_3/UV: kinetics study, matrix effect, and mechanism insight". Environ. Sci. Pollut. Res., **28**: 24535, 2021.

65. CUI, X.; LIU, X.; LIN, C.; HE, M. & OUYANG, W. "Activation of peroxymonosulfate using drinking water treatment residuals modified by

hydrothermal treatment for imidacloprid degradation". Chemosphere, **254**: 126820, 2020.

66. LI, J.; JIANG, Y. & LI, D. "Determination of imidacloprid and its relevant metabolites in tomato using modified QuEChERS combined with ultrahigh-pressure liquid chromatography/Orbitrap tandem mass spectrometry". J. Sci. Food Agric., **99**: 5211, 2019.

67. AHMADI, M.; GHANBARI, F. & MORADI, M. "Photocatalysis assisted by peroxymonosulfate and persulfate for benzotriazole degradation: effect of pH on sulfate and hydroxyl radicals". Water Sci. Technol., **72**: 2095, 2015.

68. LI, X.; JIE, B.; LIN, H.; DENG, Z.; QIAN, J.; YANG, Y. & ZHANG, X. "Application of sulfate radicals-based advanced oxidation technology in degradation of trace organic contaminants (TrOCs): Recent advances and prospects". J. Environ. Manage., **308**: 114664, 2022.

69. OH, W.-D.; DONG, Z. & LIM, T.-T. "Generation of sulfate radical through heterogeneous catalysis for organic contaminants removal: Current development, challenges and prospects". Appl. Catal. B Environ., **194**: 169, 2016.

70. NÚÑEZ-DE LA ROSA, Y.; DURANGO, L.G.C.; FORIM, M.R.; NASCIMENTO, O.R.; HAMMER, P. & AQUINO, J.M. "Unraveling the time evolution and post mortem changes of nanometric MnOOH during in situ oxidation of ciprofloxacin by activated peroxymonosulfate". Appl. Catal. B Environ., **327**: 122439, 2023.

71. LIANG, C. & SU, H.-W. "Identification of sulfate and hydroxyl radicals in thermally activated persulfate". Ind. Eng. Chem. Res., **48**: 5558, 2009.

72. ZHU, S.; LI, X.; KANG, J.; DUAN, X. & WANG, S. "Persulfate activation on crystallographic manganese oxides: mechanism of singlet oxygen evolution for nonradical selective degradation of aqueous contaminants". Environ. Sci. Technol., **53**: 307, 2019.

73. MOHAMMADI, S.; MOUSSAVI, G.; SHEKOOHIYAN, S.; MARÍN, M.L.; BOSCÁ, F. & GIANNAKIS, S. “A continuous-flow catalytic process with natural hematite-alginate beads for effective water decontamination and disinfection: Peroxymonosulfate activation leading to dominant sulfate radical and minor non-radical pathways”. Chem. Eng. J., **411**: 127738, 2021.

74. WANG, L.; LI, J.; LIU, X.; ZHANG, J.; ZENG, P. & SONG, Y. “Overestimation of $^1O_2$ role in N-doped carbon materials/peroxymonosulfate system: The misleading of furfuryl alcohol quenching effect”. Chemosphere, **324**: 138264, 2023.

75. YANG, Y.; BANERJEE, G.; BRUDVIG, G.W.; KIM, J.-H. & PIGNATELLO, J.J. “Oxidation of organic compounds in water by unactivated peroxymonosulfate”. Environ. Sci. Technol., **52**: 5911, 2018.

76. ZHANG, Z. & EDWARDS, J.O. “Chain lengths in the decomposition of peroxomonosulfate catalyzed by cobalt and vanadium. Rate law for catalysis by vanadium”. Inorg. Chem., **31**: 3514, 1992.

77. GOO, Y.R.; MAITY, A.C.; CHO, K.-B.; LEE, Y.-M.; SEO, M.S.; PARK, Y.J.; CHO, J. & NAM, W. “Tuning the reactivity of chromium (III)-superoxo species by coordinating axial ligands”. Inorg. Chem., **54**: 10513, 2015.

78. PINTO, T.T., NÚÑEZ-DE LA ROSA, Y., HAMMER, P. & AQUINO, J.M. “On the performance of self-organized TiO_2 nanotubes@MnO_x as supercapacitor: Influence of the heat treatment, cathodic treatment, water aging, and thermal oxides”. Electrochimica Acta, **408**: 139898, 2022.

79. MENG, L.; RAO, D.; TIAN, W.; CAO, F.; YAN, X. & LI, L. “Simultaneous manipulation of O-doping and metal vacancy in atomically thin $Zn_{10}In_{16}S_{34}$ nanosheet arrays toward improved photoelectrochemical performance”. Angew. Chem. Int. Ed., **57**: 16882, 2018.

80. ZHAO, X.; WANG, J.; LIAN, L.; ZHANG, G.; AN, P.; ZENG, K.; HE, H.; YUAN, T.; HUANG, J.; WANG, L. & LIU, Y.-N. “Oxygen vacancy-reinforced water-assisted proton hopping for enhanced catalytic hydrogenation”. ACS Catal. **13**: 2326, 2023.

81. ZHONG, Y.; WANG, R.; CHEN, J.; DUAN, C.; HUANG, Z.; YU, S.; GUO, H. & ZHOU, Y. “Surface-terminated hydroxyl groups for deciphering the facet-dependent photocatalysis of anatase TiO_2”. ACS Appl. Mater. Interfaces, **14**: 17601, 2022.

82. LYU, C.; ZHANG, L.; HE, D.; SU, B. & LYU, Y. “Micrometer-sized NiOOH hierarchical spheres for enhanced degradation of sulfadiazine via synergistic adsorption and catalytic oxidation in peroxymonosulfate system”. Chin. Chem. Lett., **33**: 930, 2022.

APPENDIX

TABLE A1 Instrumental parameters optimized during ICP-OES analyses.

Parameters	Values
Integration time for the emission line (s)	5
Sample flow rate (mL min^{-1})	4.2
Sample flow rate during analysis (mL min^{-1})	2.1
Peristaltic pump stabilization time (s)	25
Applied radio frequency power (W)	1200
Auxiliary gas flow rate (L min^{-1})	0.25
Nebulizing gas flow rate (L min^{-1})	0.83
Cooling gas flow rate (L min^{-1})	16
Co emission line used (nm) and signal observation	228.616 (Axial)
Fe emission line used (nm) and signal observation	259.940 (Axial)

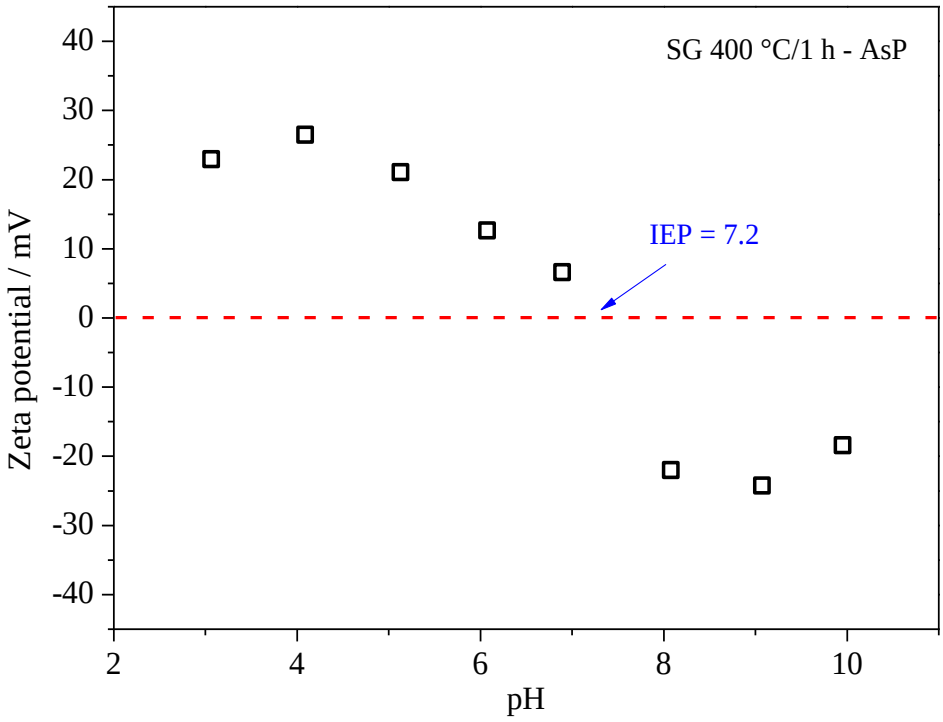

FIGURE A1 Evolution of the zeta potential values as a function of the solution pH for the as-prepared (AsP) $CoFe_2O_4$ magnetic ferrite (CMF) synthesized by the sol-gel (SG) method and thermally treated at 400 ºC for 1 h.

Ion composition of tap water and some of its physicochemical parameters can be seen below.

TABLE A2 Chemical composition of tap H_2O.

Parameters	Experimental values
pH	6.14 – 6.20 (21.6 ºC)
Conductivity / mS cm^{-1}	32 µS cm^{-1} (21.2 ºC)
TOC (mg L^{-1})*	0.0
$[Na^+]$ / mg L^{-1}	1.85
$[K^+]$ / mg L^{-1}	2.96
$[Mg^{2+}]$ / mg L^{-1}	1.47
$[Ca^{2+}]$ / mg L^{-1}	2.61
$[Br^-]$ / mg L^{-1}	5.32
$[Cl^-]$ / mg L^{-1}	0.58
$[F^-]$ / mg L^{-1}	Traces (not quantified)
$[SO_4^{2-}]$ / mg L^{-1}	0.28

*Total organic carbon (TOC) measurement carried out as described in [2].

TEXT A1

Simulated municipal wastewater (SMWW)

The SMWW was used as wastewater model for a secondary effluent matrix. The composition of SMWW was prepared considering the work of Sánchez-Montes *et al.*, [3], as well as receipts described in Zhang *et al.*, [4], and in APHA Standard Methods [5] with modifications. The following chemicals were used:

i) inorganics salts: $NaHCO_3$ (96 mg L^{-1}), $MgSO_4$ (60 mg L^{-1}), NaCl (580 mg L^{-1}), K_2HPO_4 (7.0 mg L^{-1}), $CaSO_4 \bullet 2H_2O$ (60 mg L^{-1}), $(NH_4)_2SO_4$ (23.6 mg L^{-1}) and KCl (4 mg L^{-1}).

ii) organic matter: beef extract (1.8 mg L^{-1}), peptone (2.7 mg L^{-1}), humic acid (4.2 mg L^{-1}), sodium lignin sulfonate (2.4 mg L^{-1}), sodium lauryl sulphate (0.9 mg L^{-1}), tannic acid (4.2 mg L^{-1}) and acacia gum powder (4.7 mg L^{-1}).

Some of the physicochemical parameters of the produced SMWW can be seen below:

TABLE A3 Physicochemical parameters of SMWW effluent.

Parameters	Experimental values
pH	7.43 – 7.50 (21.6 ºC)
Conductivity / mS cm^{-1}	1,309 µS cm^{-1} (20.8 ºC)
TOC (mg L^{-1})*	2.76 ±0.33

*Total organic carbon (TOC) measurement carried out as described in [1].

TEXT A2

UHPLC chromatographic conditions and Q-TOF/MS analyses for elucidation of IMD oxidation byproducts

Samples at varying treating times were analyzed using an Agilent 1290 Infinity II Ultra High-Performance Liquid Chromatograph (UHPLC – from Agilent Technologies, Santa Clara, CA, USA). Chromatographic separation was performed using a Zorbax Eclipse Plus C18 column (50 mm × 2.1 mm i.d., 1.8 µm, Agilent, USA). The mobile phase consisted of 0.1% formic acid solution (solvent A) and acetonitrile (solvent B). The chromatographic gradient used was as follows: 0-2 min, 20% B; 2.1-2.5 min, from 20 to 50% B; 2.5-7.0 min, from 50%-90% B. Column oven and autosampler temperatures were both set to 25 °C. The mobile phase flow and injection volume were 0.40 $mL \cdot min^{-1}$ and 0.20 µL, respectively.

Mass spectra were obtained using an Agilent 6545B Q-ToF MS system (Agilent Technologies, Santa Clara, CA, USA) equipped with an ESI Jet interface and operated in the positive ion mode using a capillary voltage that varied from 2.0 to 3.0 kV. Table A4 shows the parameter values used during MS experiments that were optimized for the IMD standard.

TABLE A4 Q-ToF MS parameter values.

Parameters	Value
Desolvation gas flow rate	10 L min^{-1}
Gas temperature	250 ºC
Nebulizer pressure	30 psi
Sheath gas temperature	275 ºC
Sheath gas flow rate	10 L min^{-1}
Nozzle voltage	115 V
Fragmentor voltage	60 V
Skimmer voltage	30 V
Octopole RF peak voltage	250 V
Collision energy	2 to 5 V

Molecular ions were simultaneously obtained by the MS^E acquisition mode. Data were collected in a range of 50 to 600 Da, with a sweep rate of 3.0 spectrum s^{-1} and processed by MassHunter Workstation Software, version B.08.00.

TEXT A3

UHPLC chromatographic conditions and Q-TOF/MS analyses for elucidation of DMPO oxidation byproducts

The presence of radical (mainly HO•) oxidizing species were confirmed by UHPLC-Q-ToF MS and ESR measurements and using DMPO as spin probe. All experiments were performed using 10 mL of deionized H_2O (pH 7). In a typical experiment, 1.25 mg of $CoFe_2O_4$ and 1.54 mg of PMS (corresponding to 0.125 g L^{-1} of $CoFe_2O_4$ and 500 µM of PMS) were transferred to a 20 mL glass vial. Then, 10 mL of ultrapure H_2O (pH 7) was added to the flask to start the reaction under vigorous stirring. After 1 min reaction, 125 µL of a 4 M DMPO solution (final concentration of 100 mM) were added to a 5 mL of the resultant solution and the mixture was left under stirring for an additional 1 min. After this time, 1 mL of sample was transferred to a plastic vial that was centrifuged for 15 s at 8000 rpm. For the homogeneous process, *i.e*., when using Co(II) ions, 10 mL of a $Co(NO_3)_2•6H_2O$ solution (replacing 10 mL of ultrapure H_2O) was used (corresponding to a final concentration of 200 µg L^{-1} of Co(II) ions). Then, the same procedure (including PMS amount) was adopted, except the centrifugation step to remove the solid material. More experimental details can be seen in [6].

UHPLC analyses were carried out using a Zorbax Eclipse Plus C18 column (50 mm × 2.1 mm i.d., 1.8 µm, Agilent, USA) as stationary phase. The mobile phase consisted of 0.1% formic acid solution (solvent A) and acetonitrile (solvent B). A gradient elution mode at 0.350 mL min^{-1} was used to separate the main products according to the following sequence: 0-1 min, 5% B; 1-10 min, 95% B; 10-10.1 min, 95-5% B; and 10.5-13 min, 5% B. The injection volume, column, and autosampler temperatures were set to 1.0 µL and 35 ºC, respectively. Qualitative analyses were performed using an Agilent 6545B Q-ToF MS system (Agilent Technologies, Santa Clara, CA, USA) equipped with an ESI Jet interface, operated in positive ion mode using a capillary voltage of 2.0 kV. The desolvation gas flow and gas flow in the cone were 11 and 10 L min^{-1}, respectively. For the mass confirmation of the detected byproducts, the collision energies ranged from 5 V to 16 V. Other variables such as source temperature, fragmentation voltage, skimmer voltage, and nozzle voltage were set to 300 ºC, 40 V, 35 V and 225 V, respectively. Molecular and fragment ions were simultaneously obtained by the MS^E acquisition mode. Data collected were analyzed ranging from 50 to 600 Da and processed by the MassHunter Workstation Software version B.08.00 (Agilent Technologies, Santa Clara, CA, USA).

ESR measurements were performed on a Varian E-109 X-band spectrometer, using a rectangular cavity at room temperature. A 200 µL flat quartz cell was used to analyze samples from the test experiments.

TEXT A4

Use of 9,10-anthracenediyl-bis(methylene)dimalonic acid to quench $^1O_2$

The adopted procedure was similar to the one described in Text A3. In a typical experiment, 1.25 mg of $CoFe_2O_4$ was transferred to a 20 mL glass vial. Then, 10 mL of ultrapure H_2O (pH ~8.3 spiked with 125 mM NaOH solution) was added to the flask under vigorous stirring. After 1 min reaction, 40 µL of a 100 mM ABDA solution (final concentration of 0.4 mM) were added and the mixture was left under stirring for an additional 1 min. The UV vis spectra corresponding to this point was set to "$t = 0$ min". Then, 1.54 mg of PMS (corresponding to 500 µM of PMS and to a final pH value close to 7) was added to start reaction. UV vis spectra were obtained every 5 min. For the homogeneous process, the same procedure was adopted except for the 10 mL of a $Co(NO_3)_2 \bullet 6H_2O$ solution (replacing 10 mL of ultrapure H_2O) corresponding to a final concentration of 200 µg L^{-1} of Co(II) ions). No pH corrections were carried out during measurements, since it resulted in variations in the UV vis spectra of ABDA.

The reaction between ABDA and produced $^1O_2$ species, with gradual attenuation of the UV vis bands, is [7]:

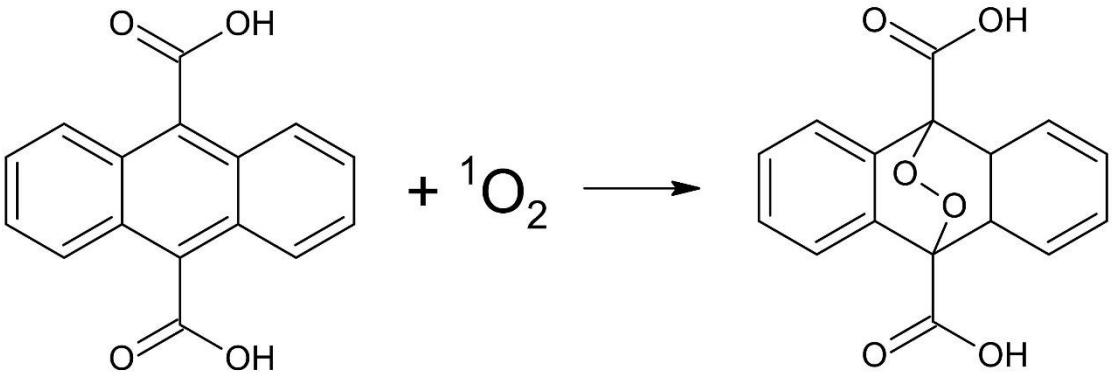

TEXT A5

The short-chain carboxylic acids were determined by HPLC. For such, a Rezex™ ROA-H column (300 mm × 7.8 mm i.d., 8 µm particle size, from Phenomenex®) as the stationary phase and a 2.5 mM H_2SO_4 solution as the mobile phase were used at 0.5 mL min^{-1}. The carboxylic acids were identified by comparing their retention times with those of previously analyzed standards. The injection volume, detection wavelength, and the temperature of the column were 25 µL, 210 nm, and 23 °C, respectively.

Inorganic ions were also analyzed by HPLC with a conductivity detector (Shimadzu CDD-10A SP). For anion determination, a Shodex SI-52 4E column at 45 °C and 3.6 mM Na_2CO_3 solution at 0.8 mL min^{-1} was used as the stationary and mobile phases, respectively. For this analysis, a chemically suppressor system (Thermo Scientific™ ACRS 500) pumping a regenerating solution of 3.6 mM H_2SO_4 at 0.8 mL min^{-1} was used. Concerning cation determination, a Shodex YS-50 column at 40 °C and a mixture of 4.0 mM oxalic acid and 6.0 $mmol^{-1}$ tartaric acid solution at 1.0 mL min^{-1} was used, as the stationary and mobile phase, respectively, without the suppressor system.

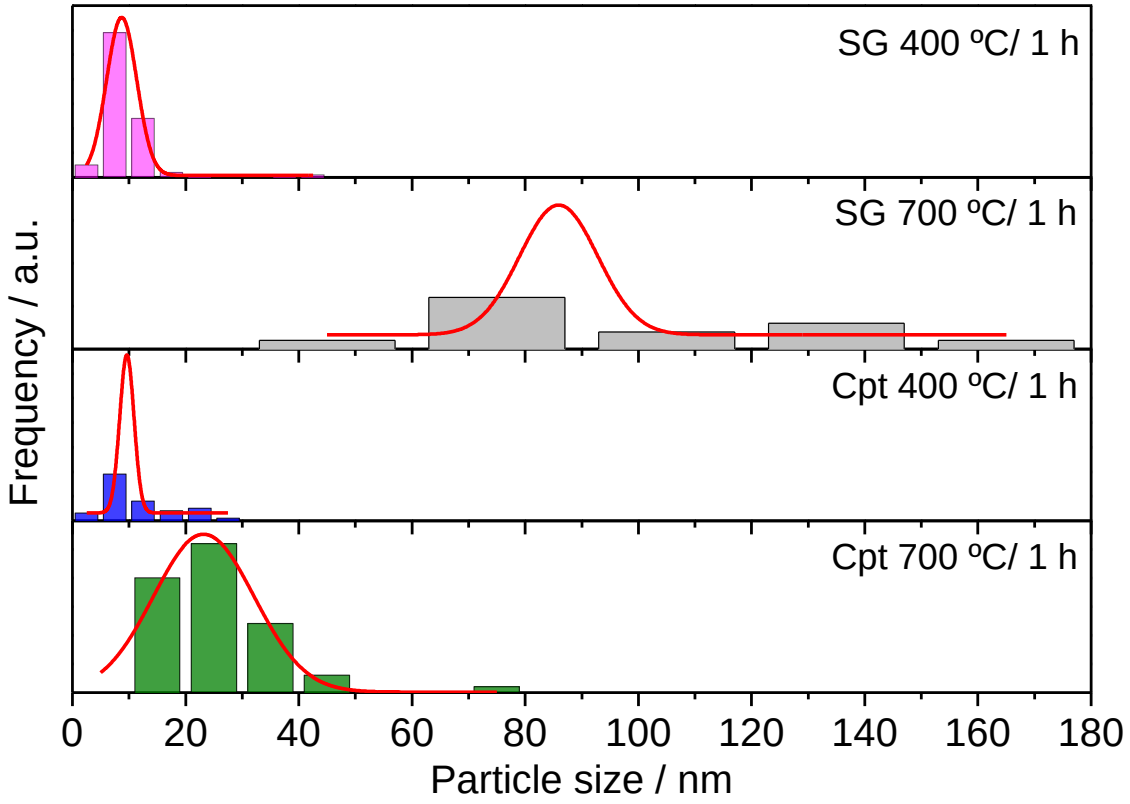

FIGURE A2 Histogram of the as-prepared $CoFe_2O_4$ magnetic ferrite (CMF) nanoparticles prepared by the sol-gel (SG) and co-precipitation (Cpt) methods and thermally treated at 400 ºC and 700 ºC for1 h (see inset).

TABLE A5 Mean particle size of the as-prepared $CoFe_2O_4$ magnetic ferrite (CMF) nanoparticles obtained from Figure A2.

Material	**Mean particle size / nm**
SG 400 ºC/1 h - AsP	9 ±3
SG 400 ºC/1 h - Us	7 ±2
SG 700 ºC/1 h – AsP	86 ±7
Cpt 400 ºC/1 h – AsP	10 ±1
Cpt 700 ºC/1 h – AsP	23 ±9

TABLE A6 Pseudo first order kinetic constants (k_{1st}) for the experiments in Figures 3.13 and 3.16 (see below).

Conditions	k_{1st} / min^{-1}	R^2
SG 400 ºC/1 h: w/buffer – pH 7	0.53	0.99
SG 400 ºC/1 h: w/o buffer – pH 7	0.14	0.99
SG 400 ºC/1 h: w/o buffer – no pH control	0.020	0.97
[Co(II)] = 20 µg L^{-1}: w/ buffer – pH 7	0.26	0.99
[Co(II)] = 50 µg L^{-1}: w/o buffer – pH 7	0.11	0.97
[Co(II)] = 50 µg L^{-1}: w/o buffer – no pH control	0.039	0.97

TABLE A7 Concentration of Co and Fe ions determined by the ICP-OES technique in degradation experiments of Figure 3.12 using the $CoFe_2O_4$ magnetic ferrite.

Samples ID	[Co] / mg L^{-1}	[Fe] / mg L^{-1}
SG 400 ºC/1 h, t = 0 h (after 2 h adsorption)	0.097	0.043
SG 400 ºC/1 h, t = 2 h (4 h in total)	0.19	0.057
SG 700 ºC/1 h, t = 0 h (after 2 h adsorption)	0.05	0.032
SG 700 ºC/1 h, t = 2 h (4 h in total)	0.049	0.036
Cpt 400 ºC/1 h, t = 0 h (after 2 h adsorption)	0.098	0.281
Cpt 400 ºC/1 h, t = 2 h (4 h in total)	0.128	0.159
Cpt 700 ºC/1 h, t = 0 h (after 2 h adsorption)	0.172	0.306
Cpt 700 ºC/1 h, t = 2 h (4 h in total)	0.117	0.13

QL = Quantification limit for both metals: 10 µg L^{-1}

DL = Detection limit for both metals: 4 µg L^{-1}

TEXT A6

Carbonization of $CoFe_2O_4$ magnetic ferrite (CMF) nanoparticles using glucose and polyvinyl alcohol (PVA)

CMF nanoparticles previously prepared by the Cpt method (thermally treated at 700 ºC for 1 h) were mixed and ground with glucose using two different proportions (CMF to glucose, in mass: 1:0.25 (Cpt: 700 ºC/1 h : glucose (1:0.25)) and 1:1 (Cpt: 700 ºC/1 h : glucose (1:1)) – see below). After grinding and homogenizing in an Agata mortar, the powder was transferred to a Al_2O_3 crucible that was placed inside a quartz tube. Then, the latter was connected to gas hoses and put inside a tube furnace. The treating temperature and time were adjusted to 600 ºC during 30 min.

Concerning the samples that were previously prepared by the sol-gel method and using PVA, the obtained powder from the sol-gel synthesis were ground (not previously heat treated) in an Agata mortar and transferred to a Al_2O_3 crucible. Then, the latter was placed in a quartz tube that was connected to gas hoses and put inside a tube furnace. The treating time was set to 1 h and the target temperature was adjusted to 400 ºC and 700 ºC. Thus, two samples were prepared and labeled as SG400 ºC/1 h@C and SG700 ºC/1 h@C.

In all reported procedures and before the heating program, the system was left under a constant N_2 flow for 20 min (purging step). The same N_2 gas flow was set also during the heating and cooling steps. The heating rate was set to 15 ºC min^{-1}.

TABLE A8 Concentration of Co and Fe ions determined by the ICP-OES technique for the degradation experiments of Figures 3.17 and 3.18 using the $CoFe_2O_4$ magnetic ferrite.

Samples ID	**[Co] / mg L^{-1}**	**[Fe] / mg L^{-1}**
Cpt 700 ºC/1 h, *t* = 0 h (after 2 h adsorption), without glucose	0.273	0.0669
Cpt 700 ºC/1 h, *t* = 2 h (4 h in total), without glucose	0.313	0.0450
Cpt 700 ºC/1 h, *t* = 0 h (after 2 h adsorption), 1:0.25 (glucose) *m*/*m*	1.19	0.704
Cpt 700 ºC/1 h, *t* = 2 h (4 h in total), 1:0.25 (glucose) *m*/*m*	5.03	1.25
Cpt 700 ºC/1 h, *t* = 0 h (after 2 h adsorption), 1:1 (glucose) *m*/*m*	0.769	0.141
Cpt 700 ºC/1 h, *t* = 2 h (4 h in total), 1:1 (glucose) *m*/*m*	0.828	0.139
SG 400 ºC/1 h@C (after 2 h adsorption)	0.103	0.0748
SG 400 ºC/1 h@C (4 h in total)	0.175	0.0918
SG 700 ºC/1 h@C (after 2 h adsorption)	0.0384	0.0635
SG 700 ºC/1 h@C (4 h in total)	0.0559	0.0653

QL = Quantification limit for both metals: 10 µg L^{-1}

DL = Detection limit for Co and Fe ions were 6 and 4 µg L^{-1}, respectively.

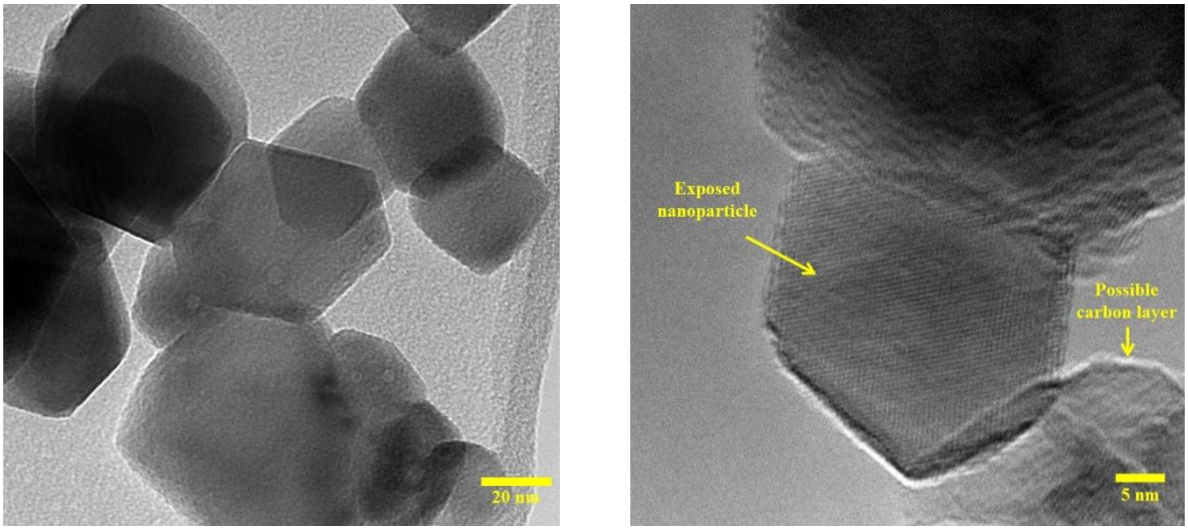

a) **b)**

FIGURE A3 **a)** TEM images of the resulting powder of the SG synthesis that was carbonized at 700 ºC for 1 h (SG 700 ºC/1 h@C) and **b)** HRTEM image of a selected area showing a nanoparticle that is *i)* completely exposed; and *ii*) possibly exhibiting a carbon layer (see details in the micrograph).

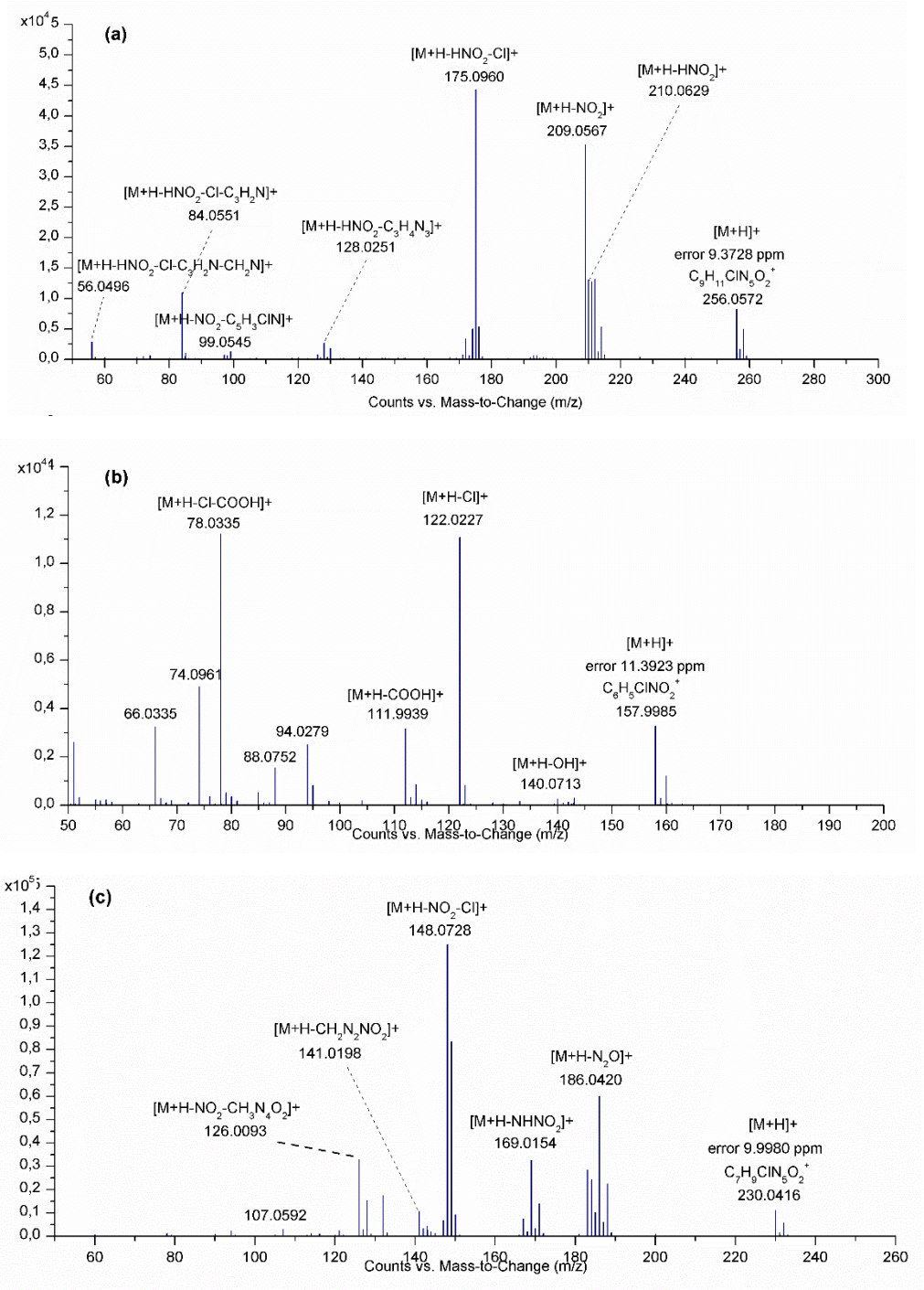

FIGURE A4 MS/MS spectra of the main detected byproducts (5 in total) resulting from IMD oxidation by radical species resulting from PMS activation by $CoFe_2O_4$ (SG 400 ºC/1 h sample): **a)** IMD, **b)** P1, **c)** P2, **d)** P3, **e)** P4, and **f)** P5. **Conditions:** 50 mg L^{-1} IMD, 500 µM PMS, pH 7.0, 10 mM KH_2PO_4, 25 °C and 0.125 g L^{-1} of the SG 400 ºC/1 h sample.

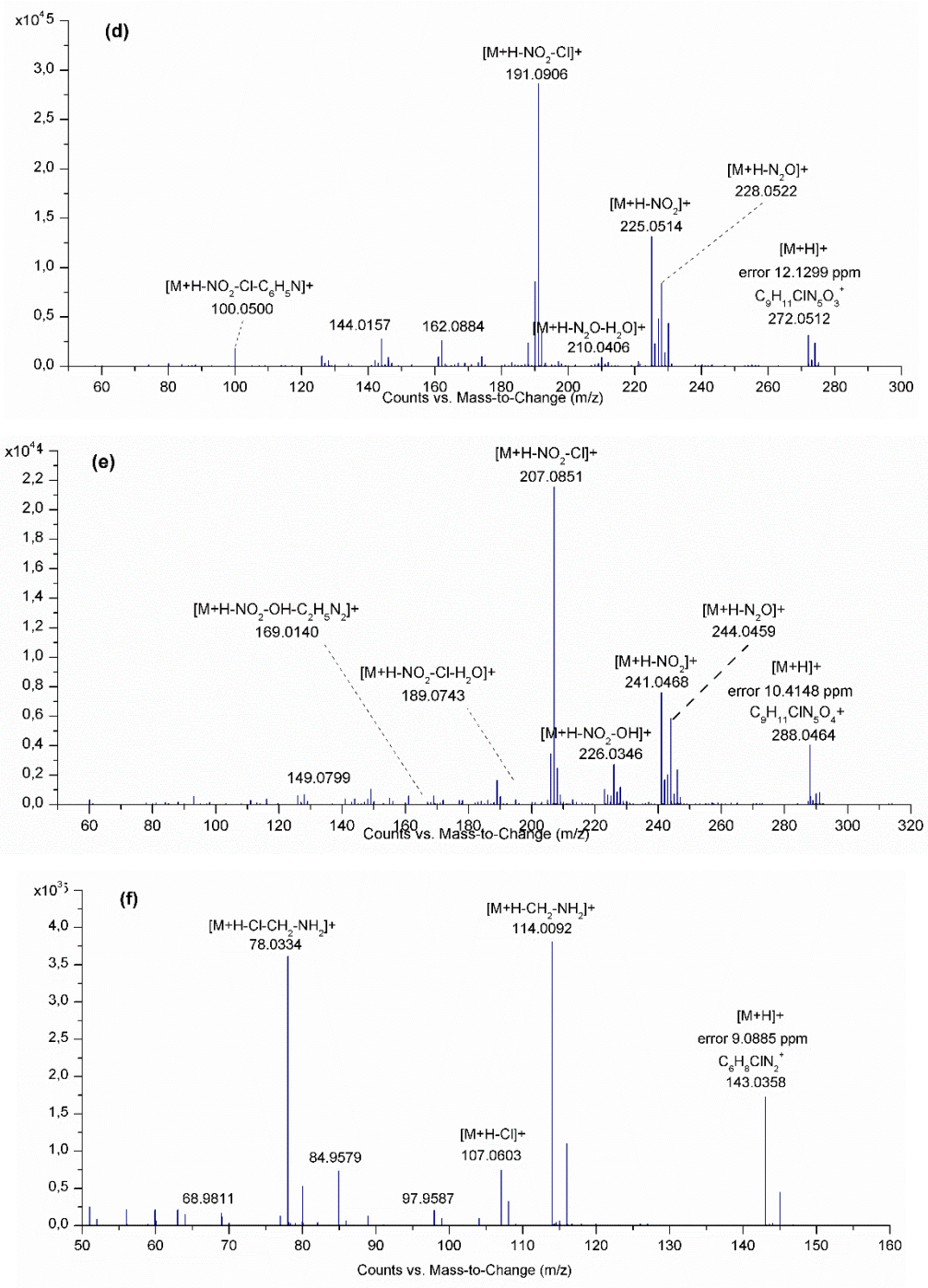

FIGURE A4 (*continuation*) MS/MS spectra of the main detected byproducts (5 in total) resulting from IMD oxidation by radical species resulting from PMS activation by $CoFe_2O_4$ (SG 400 ºC/1 h sample): **a)** IMD, **b)** P1, **c)** P2, **d)** P3, **e)** P4, and **f)** P5. **Conditions:** 50 mg L^{-1} IMD, 500 µM PMS, pH 7.0, 10 mM KH_2PO_4, 25 °C and 0.125 g L^{-1} of the SG 400 ºC/1 h sample.

TABLE A9 Retention time, main detected intermediates (*m/z*) and error of the main detected byproducts resulting from IMD oxidation by radical species resulting from PMS activation by $CoFe_2O_4$ (SG 400 ºC/1 h sample).

#	Compound	t_r (min)	ESI mode		
			m/z	Attribution (ESI+)	Error (ppm)
1	**P5**	1.841	143.0358	$[M+H]^+$	9.0885
			114.0092	$[M+H-CH_2-NH_2]^+$	
			107.0603	$[M+H-Cl]^+$	
			78.0334	$[M+H-Cl-CH_2-NH_2]^+$	
2	**P2**	6.139	230.0416	$[M+H]^+$	9.9980
			186.0420	$[M+H-N_2O]^+$	
			169.0154	$[M+H-NHNO_2]^+$	
			148.0728	$[M+H-NO_2-Cl]^+$	
			141.0198	$[M+H-CH_2N_2NO_2]^+$	
			126.0093	$[M+H-CH_3N_4O_2]^+$	
3	**P3**	6.246	272.0512	$[M+H]^+$	12.1299
			225.0514	$[M+H-NO_2]^+$	
			228.0522	$[M+H-N_2O]^+$	
			210.0406	$[M+H-N_2O-H_2O]^+$	
			191.0906	$[M+H-NO_2-Cl]^+$	
			100.0500	$[M+H-NO_2-Cl-C_6H_5N]^+$	
4	**P4**	6.414	288.0464	$[M+H]^+$	10.4148
			244.0459	$[M+H-N_2O]^+$	
			241.0468	$[M+H-NO_2]^+$	
			226.0346	$[M+H-NO_2-OH]^+$	
			207.0851	$[M+H-NO_2-Cl]^+$	
			189.0743	$[M+H-NO_2-Cl-H_2O]^+$	
			169.0140	$[M+H-NO_2-OH-C_2H_5N_2]^+$	
5	**IMD**	6.762	256.0572	$[M+H]^+$	9.3728
			210.0629	$[M+H-HNO_2]^+$	
			209.0567	$[M+H-NO_2]^+$	
			175.0960	$[M+H-HNO_2-Cl]^+$	
			128.0251	$[M+H-HNO_2-C_3H_4N_3]^+$	
			99.0545	$[M+H-NO_2-C_5H_3ClN]^+$	
			84.0551	$[M+H-HNO_2-Cl-C_3H_2N]^+$	
			56.0496	$[M+H-HNO_2-Cl-C_3H_2N-CH_2N]^+$	
6	**P1**	7.130	157.9985	$[M+H]^+$	11.3923
			140.0713	$[M+H-OH]^+$	
			122.0227	$[M+H-Cl]^+$	
			111.9939	$[M+H-COOH]^+$	
			78.0334	$[M+H-Cl-COOH]^+$	

Experimental conditions: 50 mg L^{-1} IMD, 500 µM PMS, pH 7.0, 10 mM KH_2PO_4, 25 °C and 0.125 g L^{-1} of the SG 400 ºC/1 h sample.

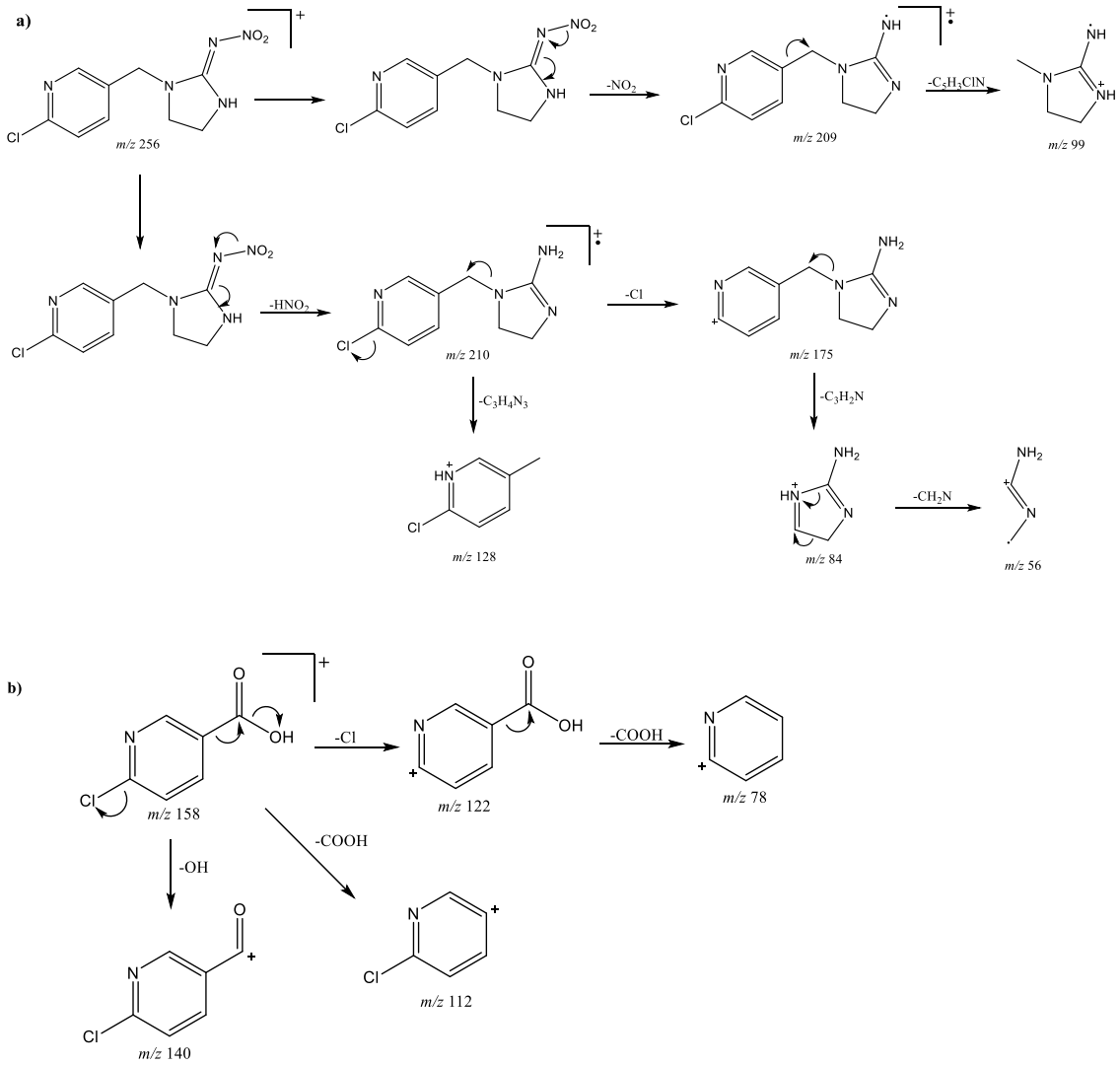

FIGURE A5 Proposed fragmentation route of the main detected intermediates showed in Table A4: **a)** IMD (*m/z* 256.0572), **b)** P1 (*m/z* 157.9985), **c)** P2 (*m/z* 230.0416), **d)** P3 (*m/z* 272.0512), **e)** P4 (*m/z* 288.0464), and **f)** P5 (*m/z* 143.0358).

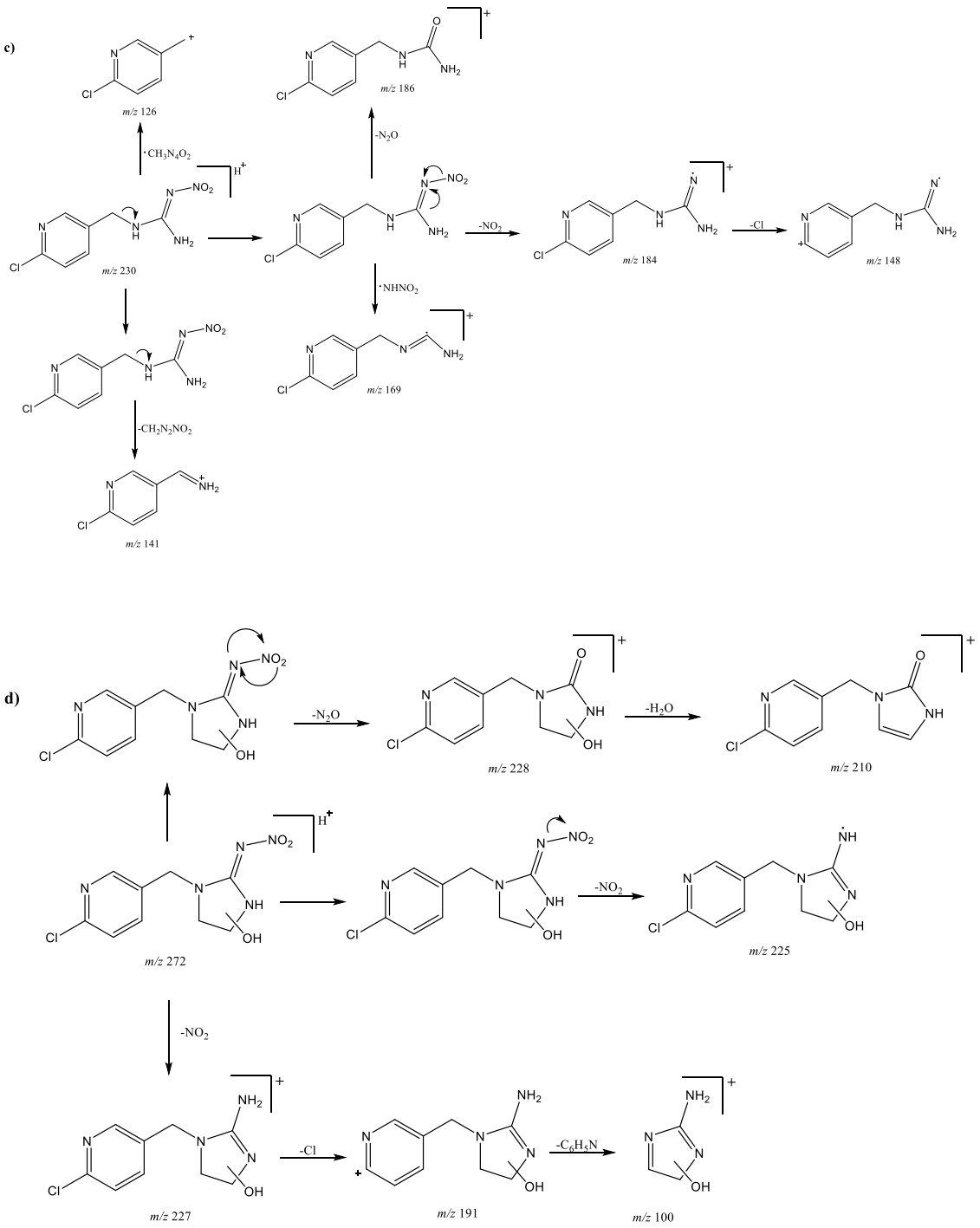

FIGURE A5 (*continuation*) Proposed fragmentation route of the main detected intermediates showed in Table A4: **a)** IMD (*m/z* 256.0572), **b)** P1 (*m/z* 157.9985), **c)** P2 (*m/z* 230.0416), **d)** P3 (*m/z* 272.0512), **e)** P4 (*m/z* 288.0464), and **f)** P5 (*m/z* 143.0358).

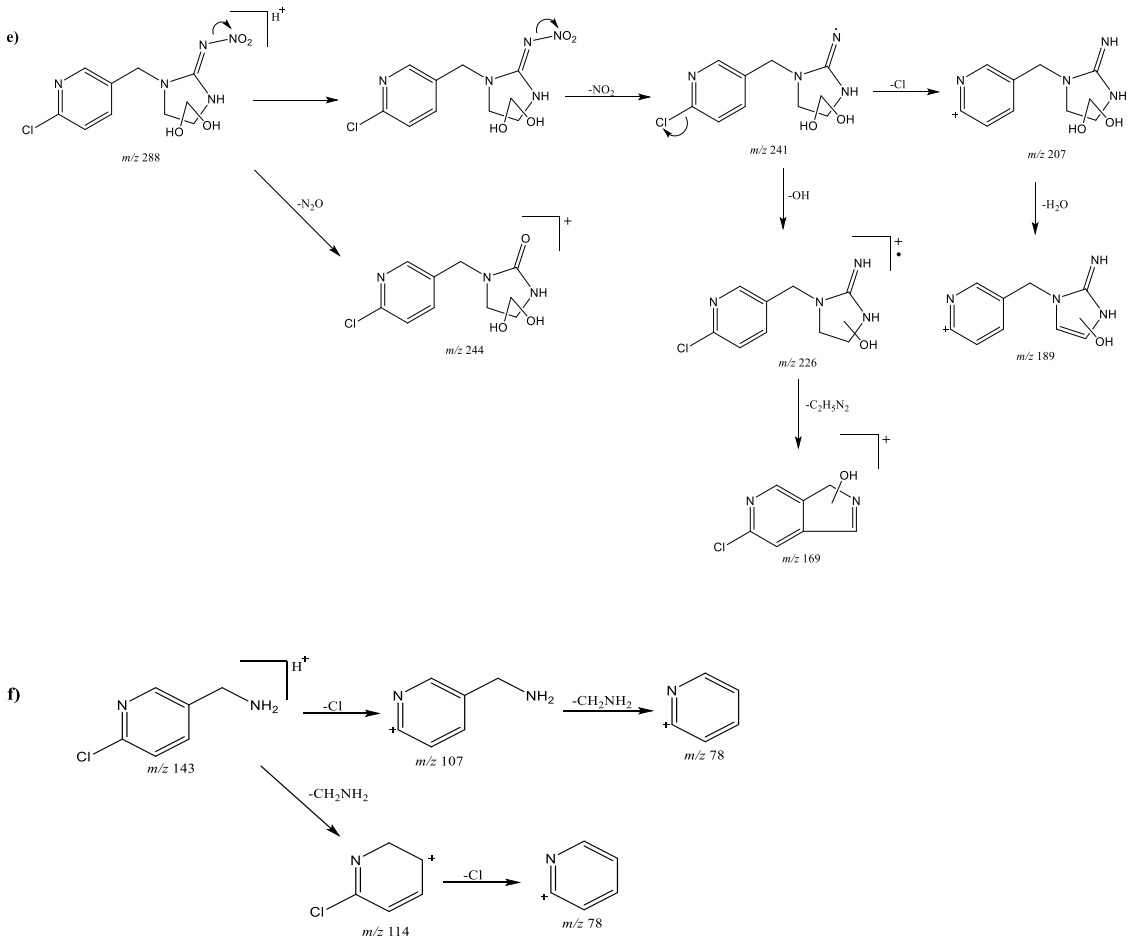

FIGURE A5 (*continuation*) Proposed fragmentation route of the main detected intermediates showed in Table A4: **a)** IMD (*m/z* 256.0572), **b)** P1 (*m/z* 157.9985), **c)** P2 (*m/z* 230.0416), **d)** P3 (*m/z* 272.0512), **e)** P4 (*m/z* 288.0464), and **f)** P5 (*m/z* 143.0358).

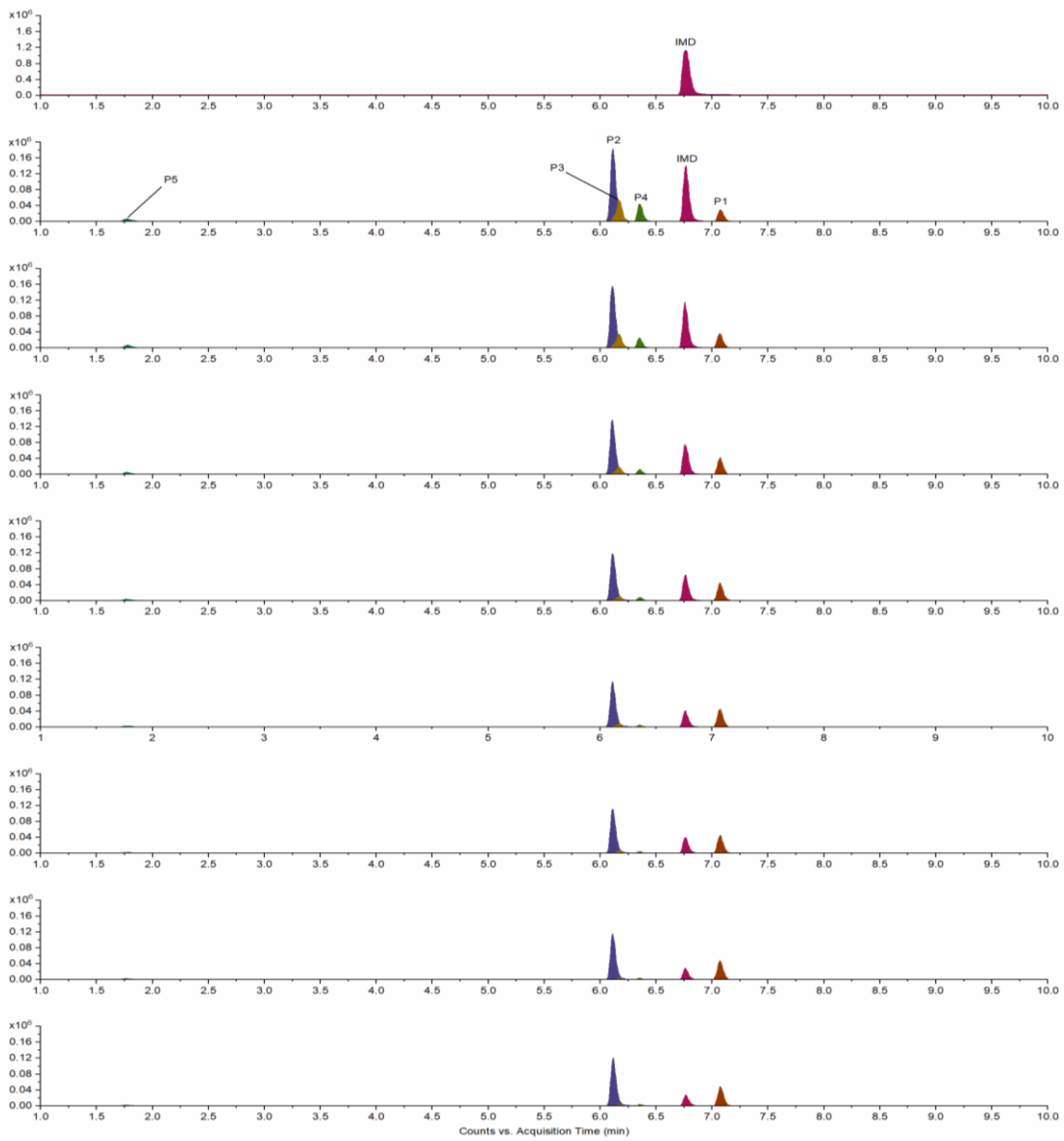

FIGURE A6 Extracted ion chromatogram of the main detected intermediates showed in Table A4 and at distinct treatment time 0, 5, 10, 20, 30, 45, 60, 90, and 120 min (from top to bottom). **Conditions:** 50 mg L^{-1} IMD, 500 µM PMS, pH 7.0, 10 mM KH_2PO_4, 25 °C and 0.125 g L^{-1} of the SG 400 ºC/1 h samples.

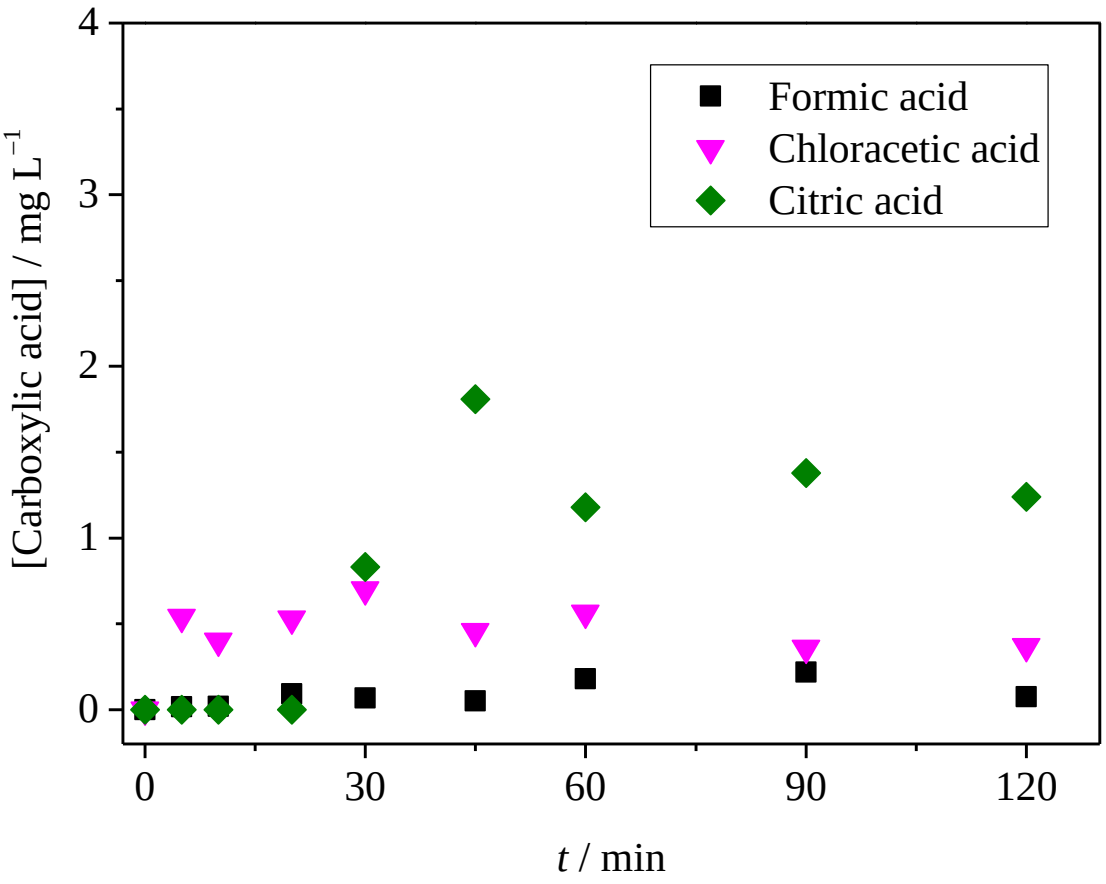

FIGURE A7 Time evolution of the main detected carboxylic acids resulting from IMD oxidation by radical species resulting from PMS activation by $CoFe_2O_4$ (SG 400 ºC/1 h sample). **Conditions:** 50 mg L^{-1} IMD, 500 µM PMS, pH 7.0, 10 mM KH_2PO_4, 25 °C and 0.125 g L^{-1} of the SG 400 ºC/1 h sample.

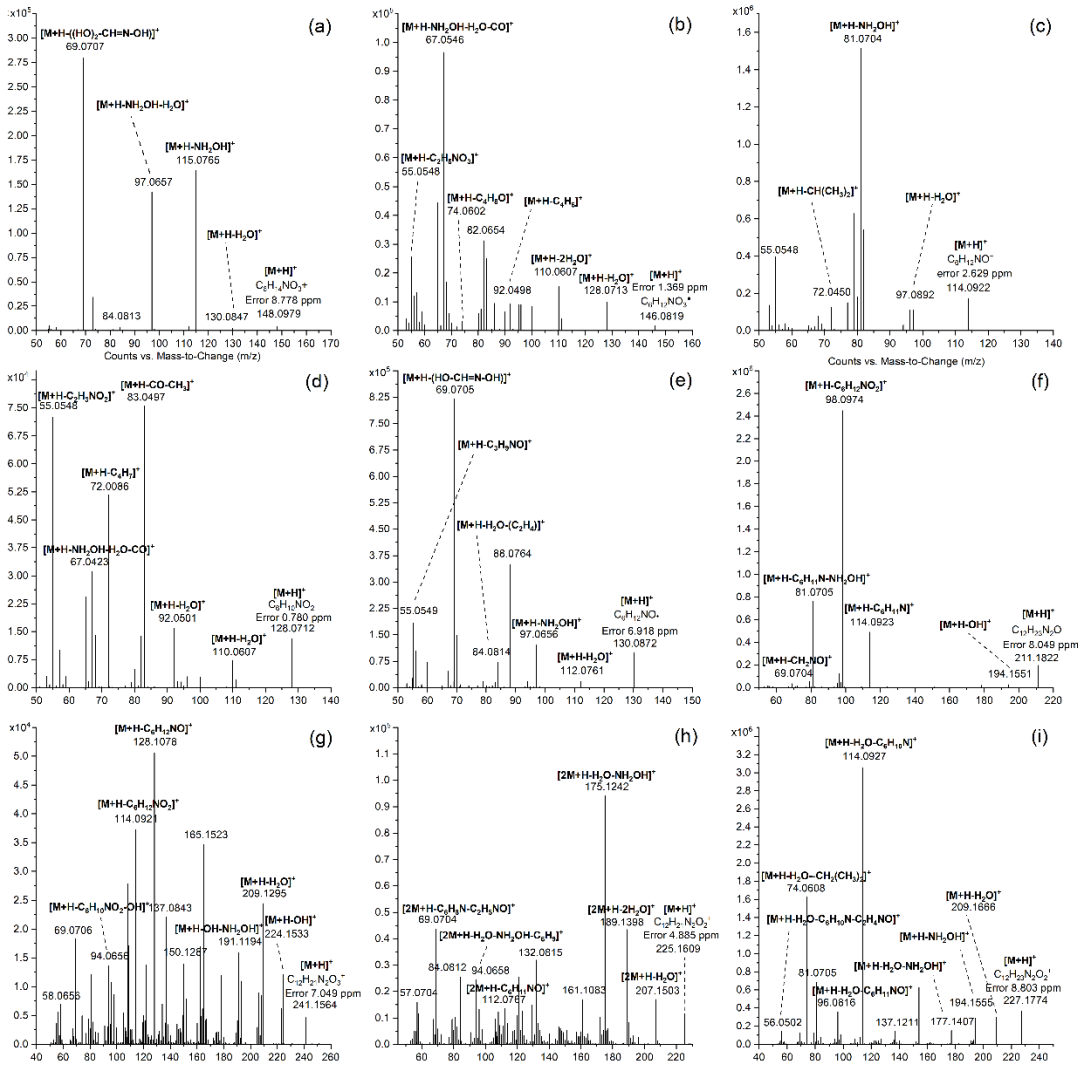

FIGURE A8 MS/MS spectra of the main detected byproducts resulting from reaction between DMPO and oxygen radical species (produced by the reaction between $CoFe_2O_4$/Co(II) ions with PMS oxidant): **a)** DMPO/2OH, **b)** DMPO$^{\bullet}$/2OH, **c)** DMPO, **d)** DMPO$^{\bullet}$/O, **e)** DMPO/OH, **f)** 2DMPO/-OH, **g)** 2DMPO/O-3H, **h)** 2DMPO/-H, and **i)** DMPO/-3H. CMF = cobalt magnetic ferrite ($CoFe_2O_4$ – SG 400 ^{o}C/1 h sample).

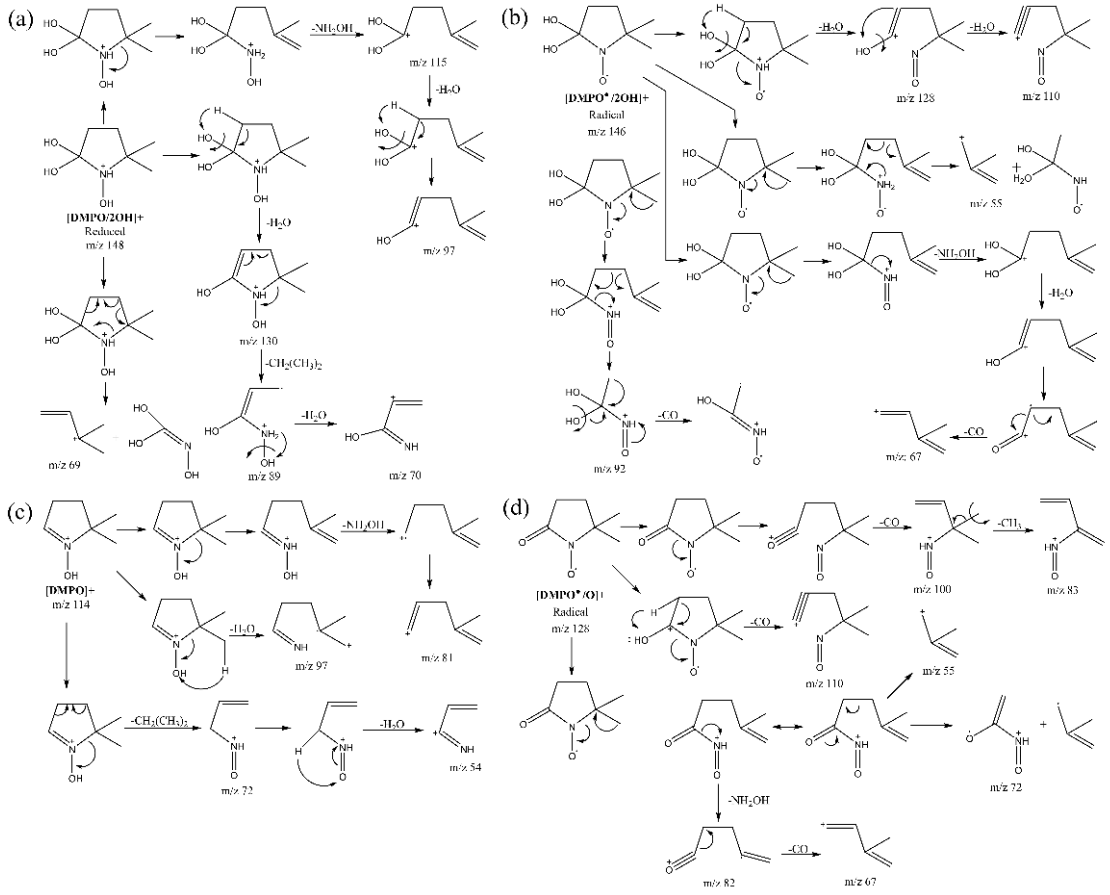

FIGURE A9 Proposed fragmentation route for the main detected DMPO byproducts resulting from reaction between DMPO and oxygen radical species (produced by the reaction between $CoFe_2O_4$/Co(II) ions with PMS oxidant): **a)** DMPO/2OH, **b)** DMPO$^{\bullet}$/2OH, **c)** DMPO, **d)** DMPO$^{\bullet}$/O, **e)** DMPO/OH, **f)** 2DMPO/-OH, **g)** 2DMPO/O-3H, **h)** 2DMPO/-3H, and **i)** 2DMPO/-H. CMF = cobalt magnetic ferrite ($CoFe_2O_4$ – SG 400 ^{o}C/1 h sample).

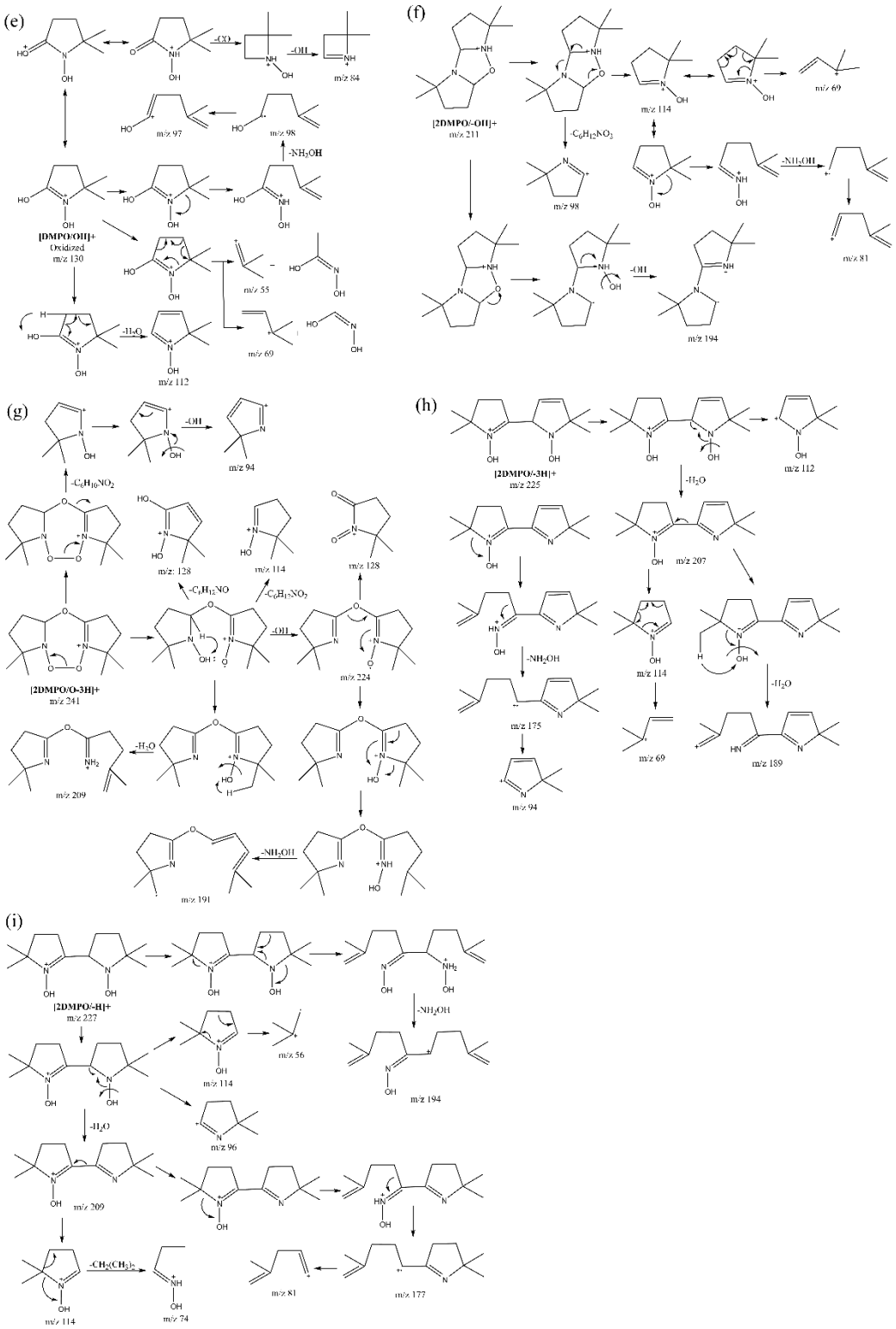

FIGURE A9 (*continuation*) Proposed fragmentation route for the main detected DMPO byproducts resulting from reaction between DMPO and oxygen radical species (produced by the reaction between $CoFe_2O_4$/Co(II) ions with PMS oxidant): **a)** DMPO/2OH, **b)** DMPO$^{\bullet}$/2OH, **c)** DMPO, **d)** DMPO$^{\bullet}$/O, **e)** DMPO/OH, **f)** 2DMPO/-OH, **g)** 2DMPO/O-3H, **h)** 2DMPO/-3H, and **i)** 2DMPO/-H. CMF = cobalt magnetic ferrite ($CoFe_2O_4$ – SG 400 ^{o}C/1 h sample).

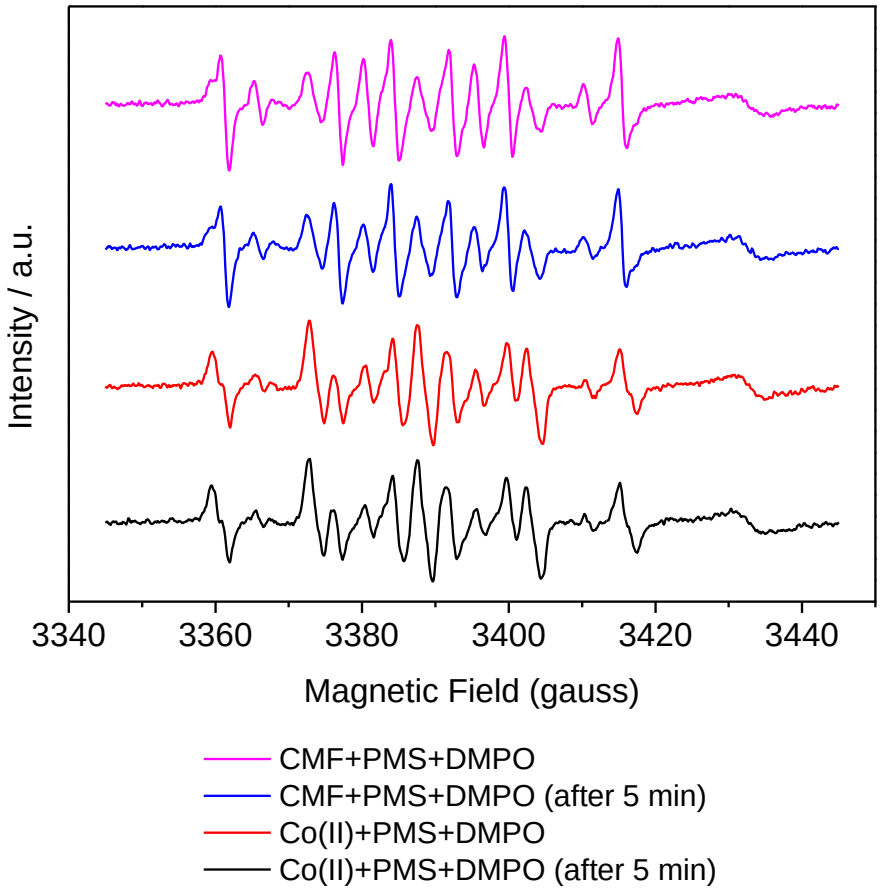

FIGURE A10 Intensity as a function of magnetic field for distinct experiments using CMF nanoparticles (0.125 g L^{-1}) and 200 µg L^{-1} of Co(II) in the presence of PMS (500 µM) and DMPO. CMF = cobalt magnetic ferrite ($CoFe_2O_4$ – SG 400 ºC/1 h sample). See Text A3 for further details.

TABLE A10 Percentage of CMF recovery after each experiment of the recycling test of Figure 3.27.

Experiment number	Mass percentage recovery / %
1st run	67
2nd run	75
3rd run	65
4th run	68
5th run	69

Conditions: 0.125 g L^{-1} CMF, 50 mg L^{-1} IMD, 500 μM PMS, pH 7.0, 10 mM KH_2PO_4, 1000 mL of treating solution at 25 °C. CMF = cobalt magnetic ferrite ($CoFe_2O_4$ – SG 400 °C/1 h sample). All experiments were carried out in the dark. The CMF solid was separated from the treating solution using a neodymium magnet. The resulting powder was washed (one time) with ultrapure H_2O followed by vacuum drying.

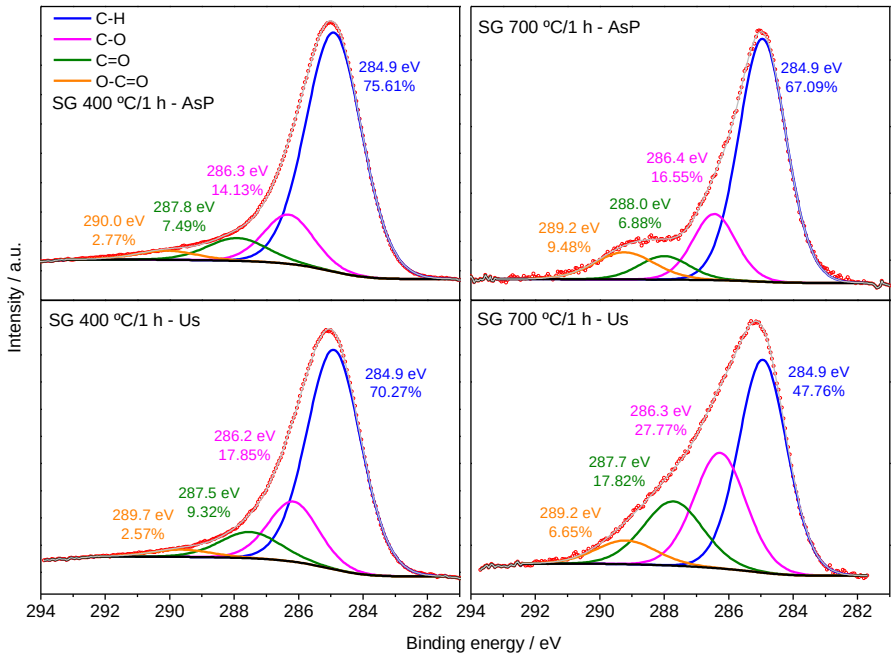

a)

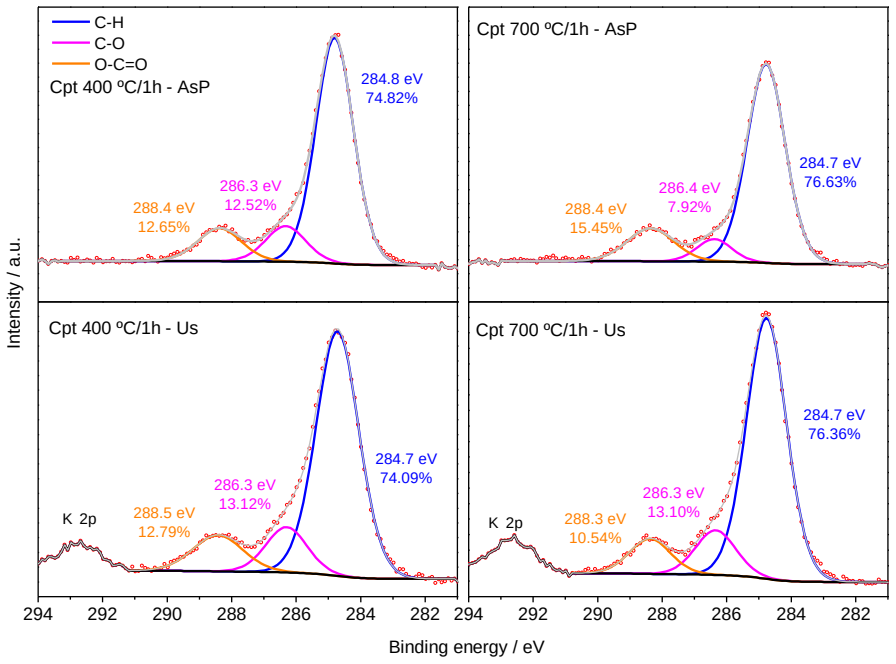

b)

FIGURE A11 High-resolution spectra of C 1s for the as-prepared (AsP) and used (Us) $CoFe_2O_4$ magnetic ferrite samples obtained by the **a)** sol-gel (SG) and **b)** co-precipitation (Cpt) methods and thermally treated at 400 ºC or 700 ºC for 1 h.

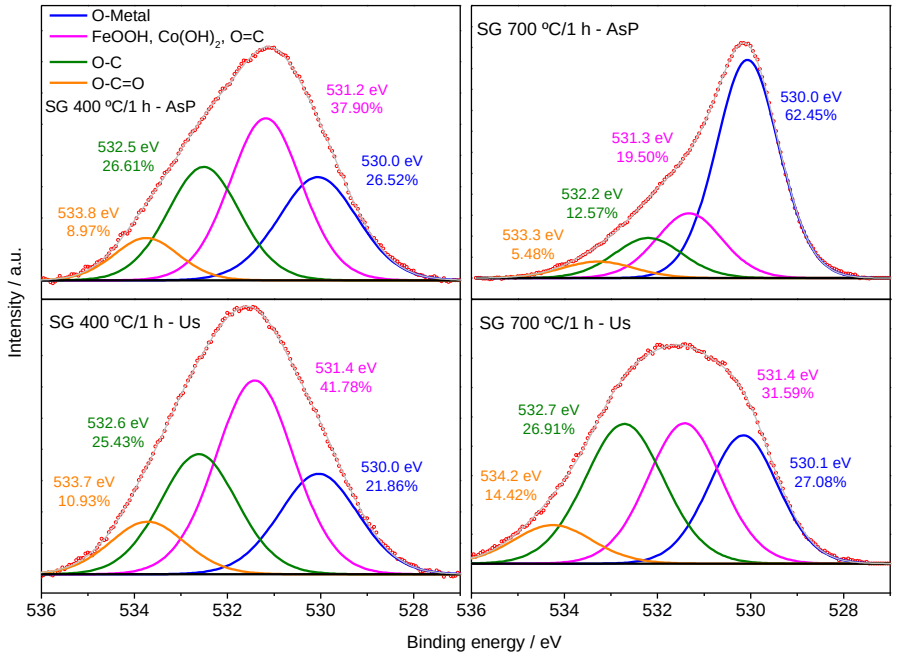

a)

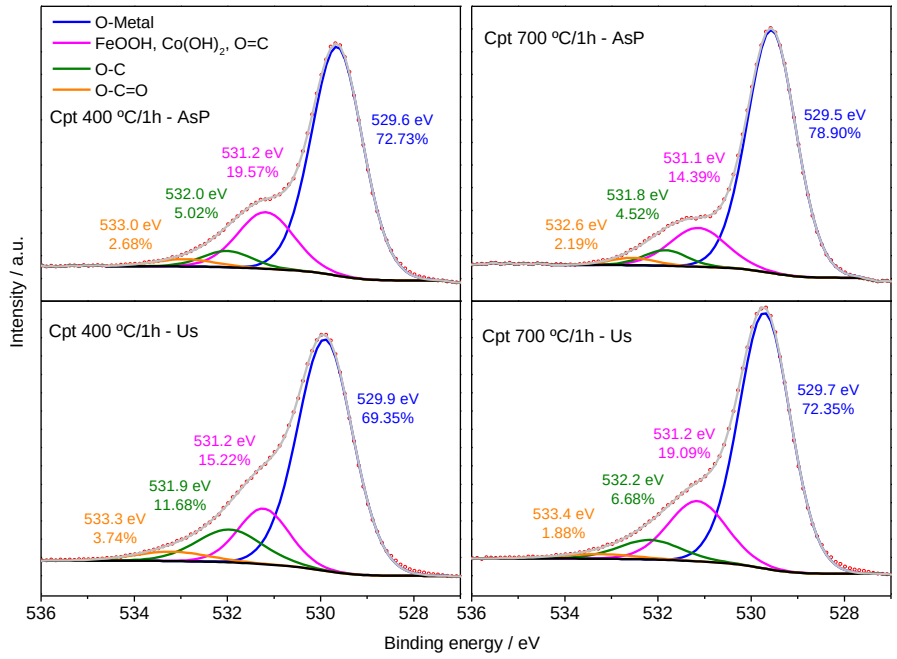

b)

FIGURE A12 High-resolution spectra of O 1s for the as-prepared (AsP) and used (Us) $CoFe_2O_4$ magnetic ferrite samples obtained by the **a)** sol-gel (SG) and **b)** co-precipitation (Cpt) methods and thermally treated at 400 ºC or 700 ºC for 1 h.

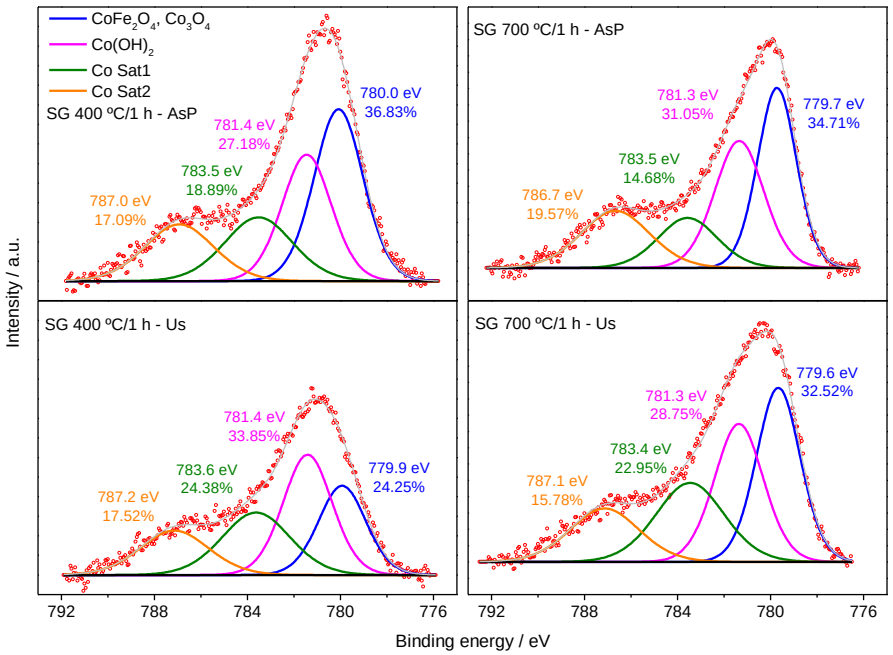

a)

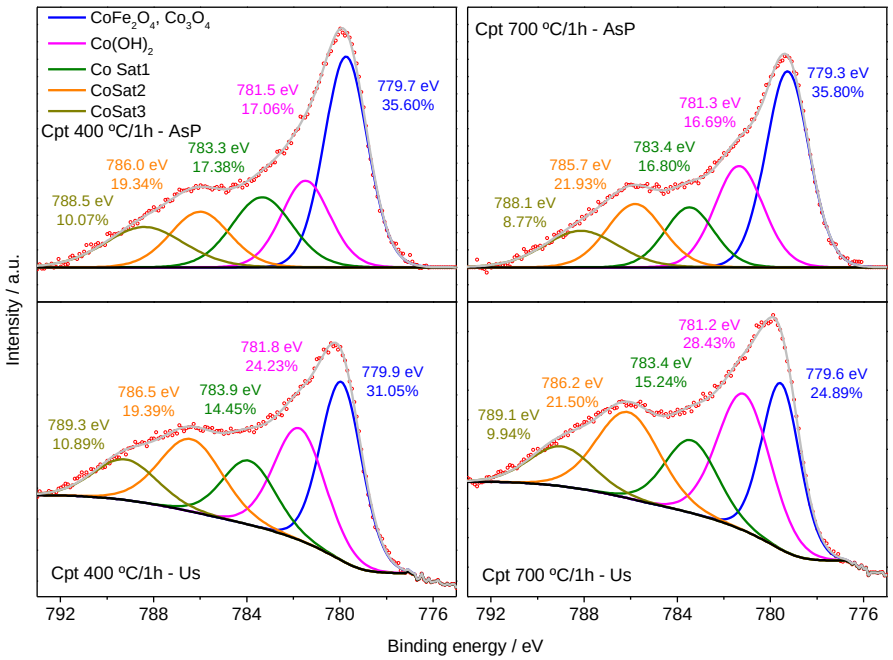

b)

FIGURE A13 High-resolution spectra of Co $2p_{3/2}$ for the as-prepared (AsP) and used (Us) $CoFe_2O_4$ magnetic ferrite samples obtained by the **a)** sol-gel (SG) and **b)** co-precipitation (Cpt) methods and thermally treated at 400 ºC or 700 ºC for 1 h.

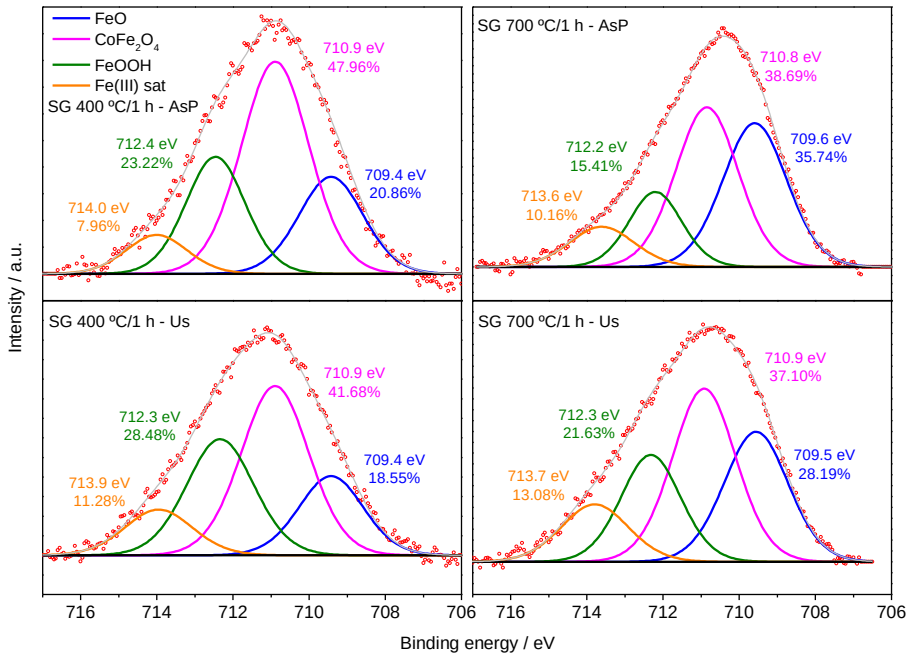

a)

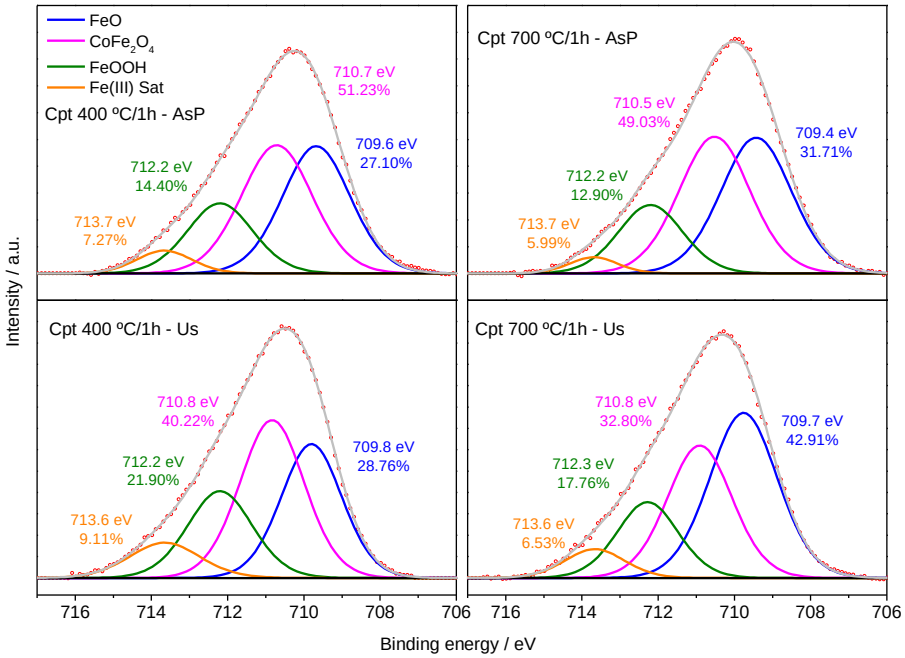

b)

FIGURE A14 High-resolution spectra of Fe $2p_{3/2}$ for the as-prepared (AsP) and used (Us) $CoFe_2O_4$ magnetic ferrite samples obtained by the **a)** sol-gel (SG) and **b)** co-precipitation (Cpt) methods and thermally treated at 400 ºC or 700 ºC for 1 h.

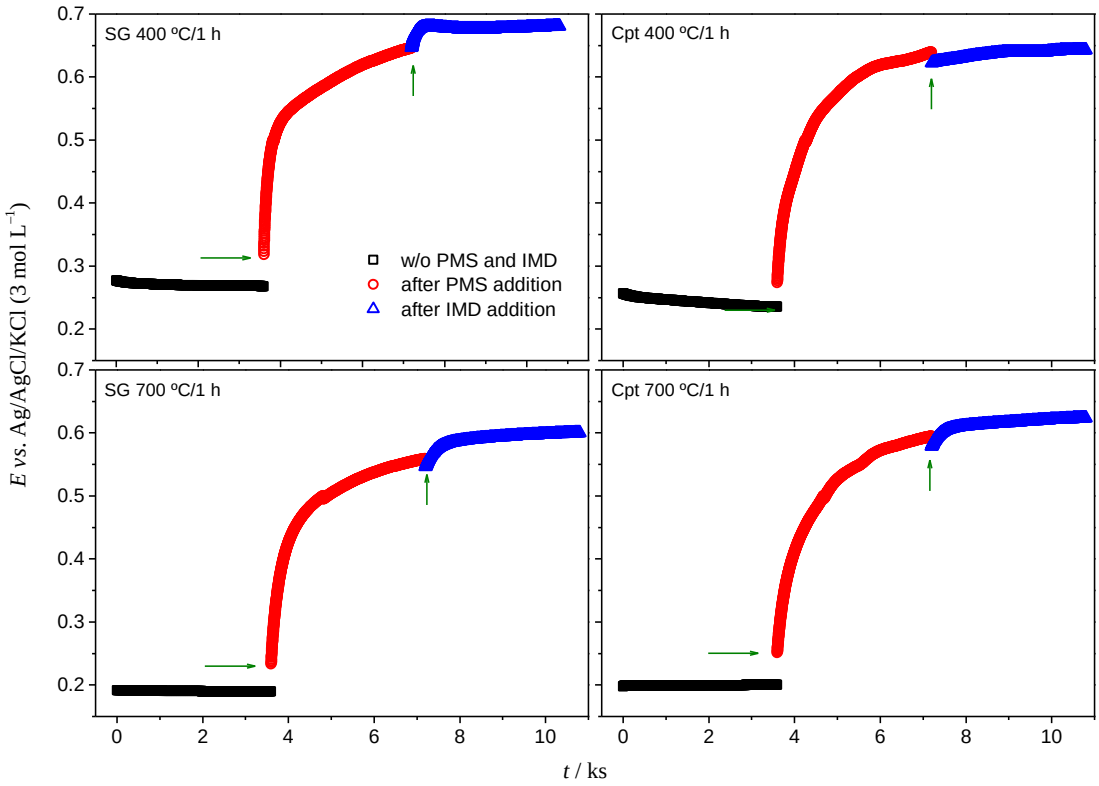

FIGURE A15 Electrode potential (*vs*. Ag/AgCl/KCl 3 M) as a function of time for distinctly prepared CMF nanoparticles (see inset for further details). A 0.5 M Na_2SO_4 (corrected to pH ~7) solution at ambient conditions was used. The arrows indicate the moment (after 1 h) when PMS and IMD were added into solution.

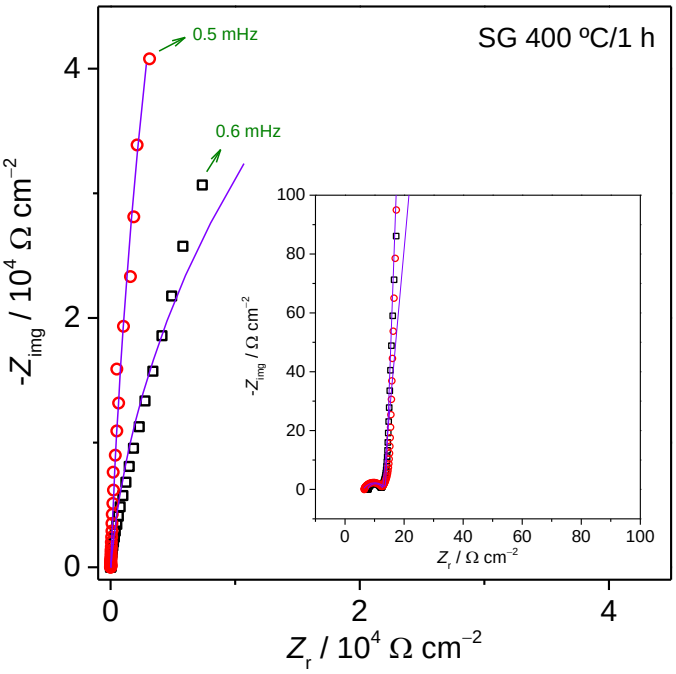

a)

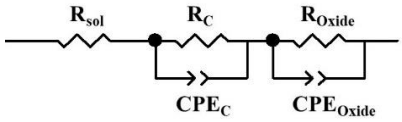

c)

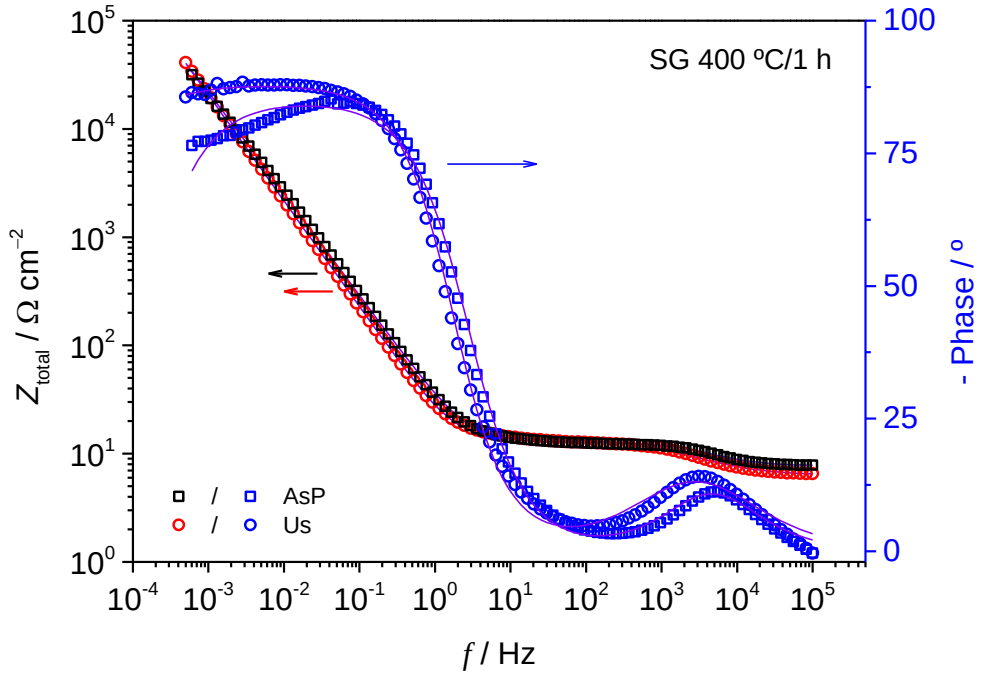

b)

FIGURE A16 **a)** Complex plane, **b)** Bode plots for the $CoFe_2O_4$ magnetic ferrite samples (in the as-prepared (AsP) and after use (Us) – see legend in the inset) obtained by the sol-gel (SG) method and heat treated at 400 ºC for 1 h, and **c)** the equivalent circuit used to fit data generated (see continuous line) by electrochemical impedance. A 0.5 M Na_2SO_4 (no pH correction) solution at ambient conditions was used.

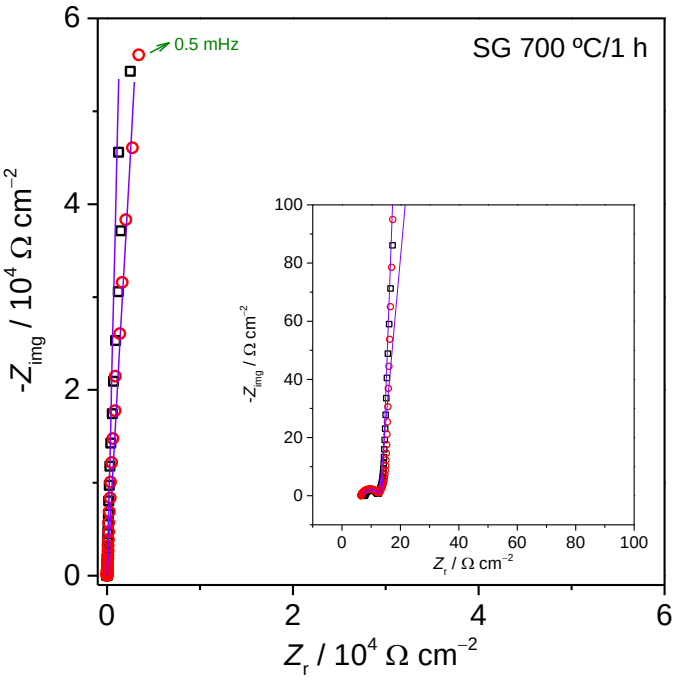

a)

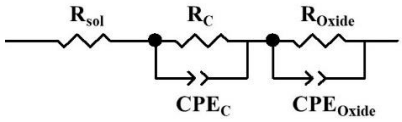

c)

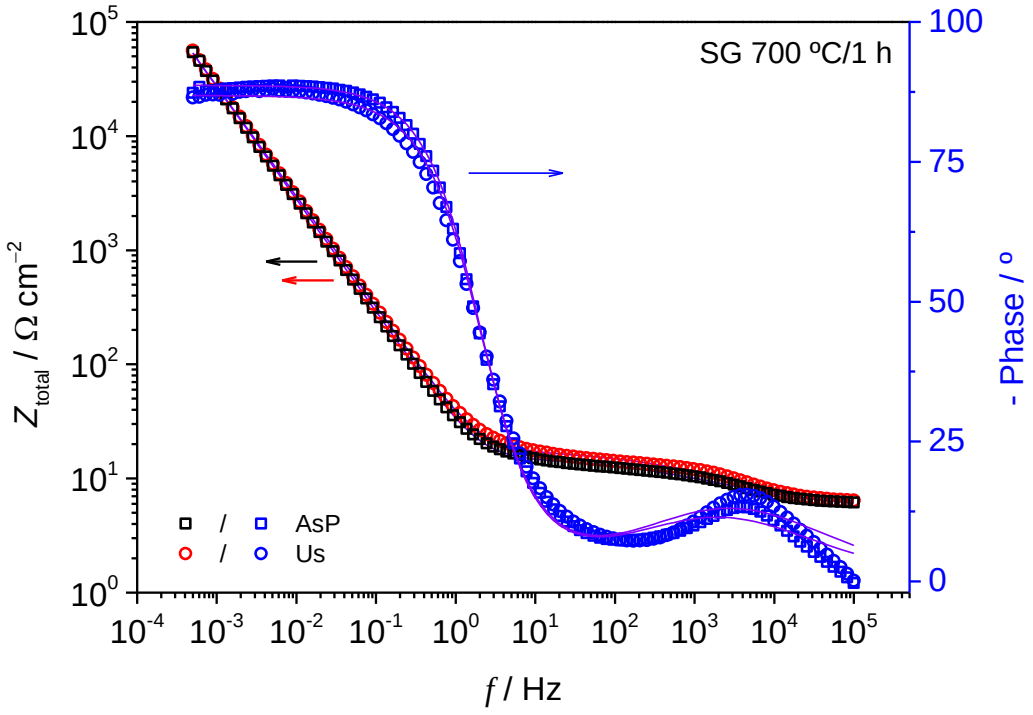

b)

FIGURE A17 **a)** Complex plane, **b)** Bode plots for the $CoFe_2O_4$ magnetic ferrite samples (in the as-prepared (AsP) and after use (Us) – see legend in the inset) obtained by the sol-gel (SG) method and heat treated at 700 ºC for 1 h, and **c)** the equivalent circuit used to fit data generated (see continuous line) by electrochemical impedance. A 0.5 M Na_2SO_4 (no pH correction) solution at ambient conditions was used.

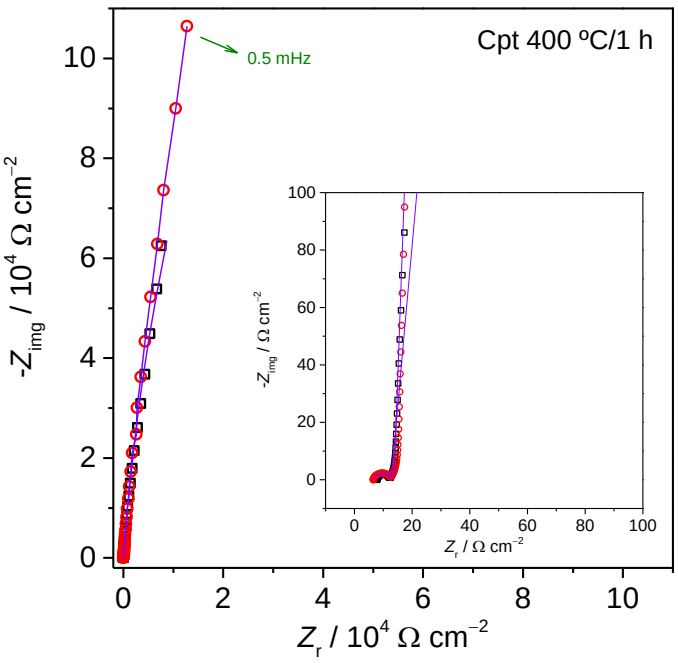

a)

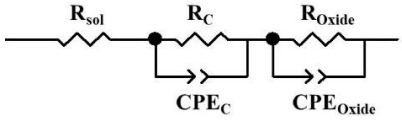

c)

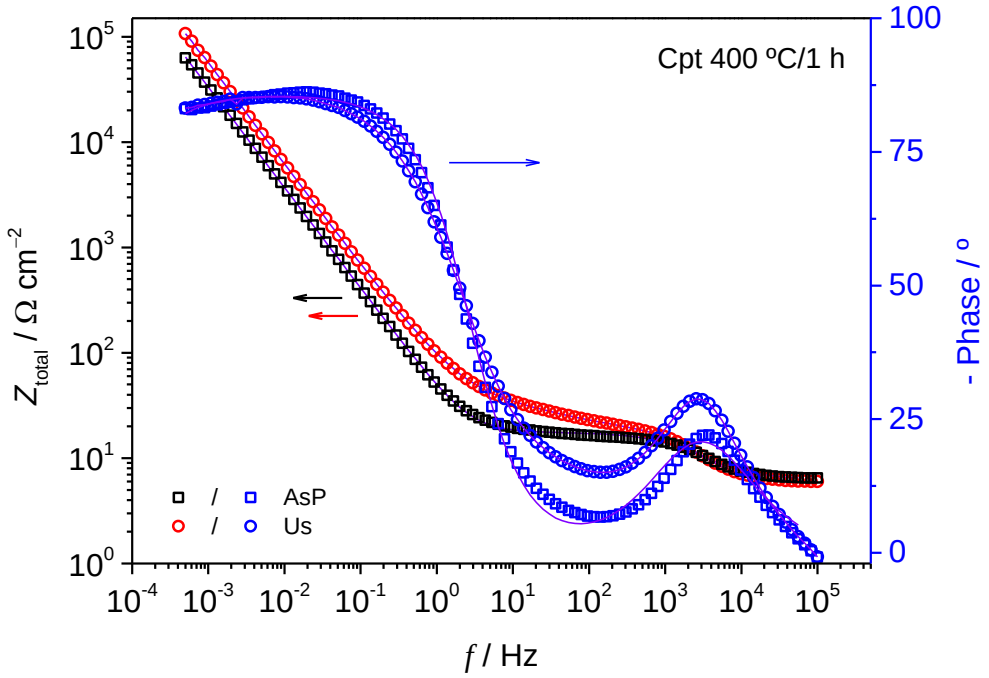

b)

FIGURE A18 **a)** Complex plane, **b)** Bode plots for the $CoFe_2O_4$ magnetic ferrite samples (in the as-prepared (AsP) and after use (Us) – see legend in the inset) obtained by the co-precipitation (Cpt) method and heat treated at 400 ºC for 1 h, and **c)** the equivalent circuit (see above) used to fit data generated (see continuous line) by electrochemical impedance. A 0.5 M Na_2SO_4 (no pH correction) solution at ambient conditions was used.

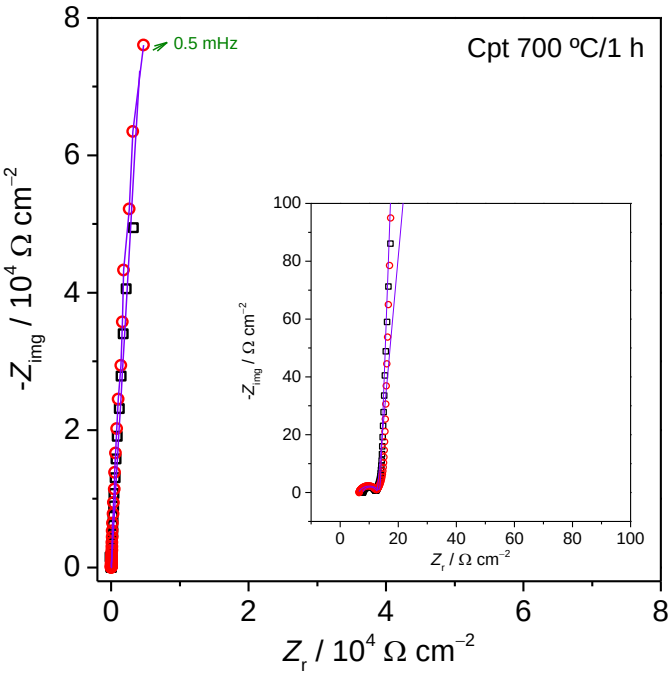

a)

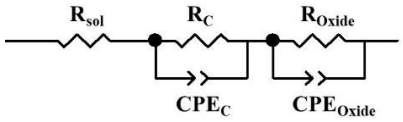

c)

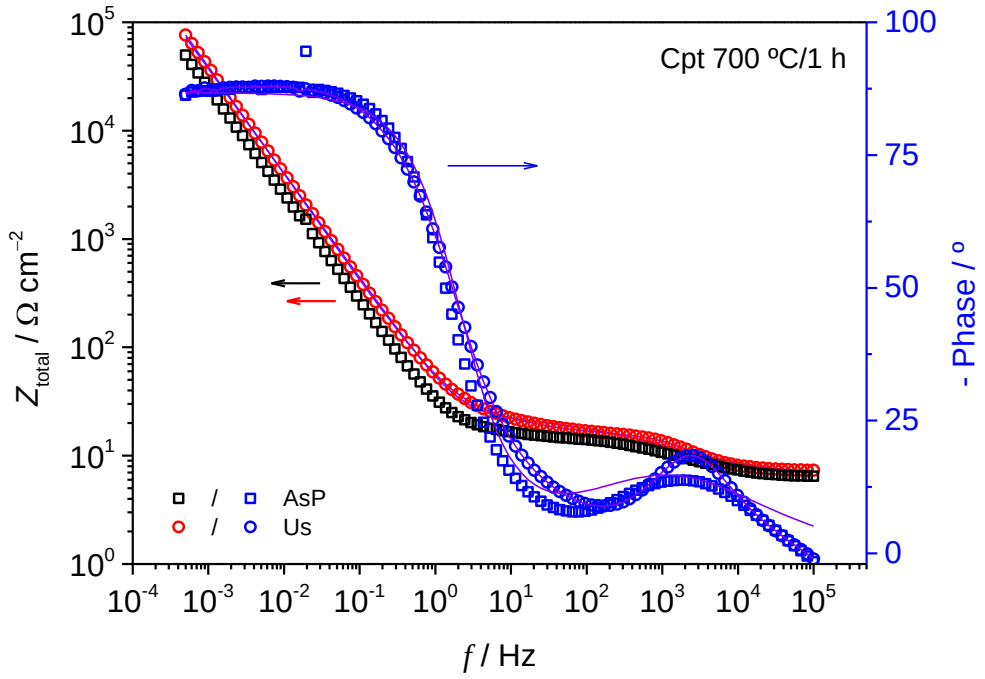

b)

FIGURE A19 **a)** Complex plane, **b)** Bode plots for the $CoFe_2O_4$ magnetic ferrite samples (in the as-prepared (AsP) and after use (Us) – see legend in the inset) obtained by the co-precipitation (Cpt) method and heat treated at 700 ºC for 1 h, and **c)** the equivalent circuit used to fit data generated (see continuous line) by electrochemical impedance. A 0.5 M Na_2SO_4 (no pH correction) solution at ambient conditions was used.

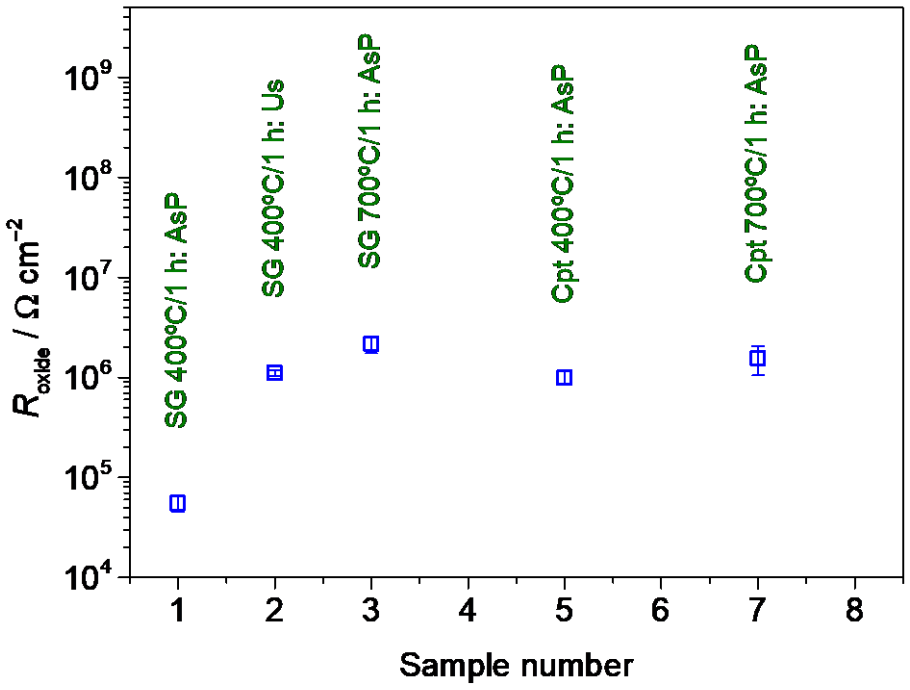

FIGURE A20 Oxide charge transfer resistance (R_{oxide}) for the as-prepared (AsP) and after use (Us) samples of the $CoFe_2O_4$ magnetic ferrite. The exposed area was close to 1 cm^2. Error bars refer to three repetitions. The R_{oxide} values for the SG 700 ºC/1 h, Cpt 400 ºC/1 h, and Cpt 400 ºC/1 h conditions after use (Us) were not determined due to lack of fit.

References

[1] DU, Y.; MA, W.; LIU, P.; ZOU, B. & MA, J. “Magnetic $CoFe_2O_4$ nanoparticles supported on titanate nanotubes ($CoFe_2O_4$/TNTs) as a novel heterogeneous catalyst for peroxymonosulfate activation and degradation of organic pollutants”. J. Hazard. Mater., **308**: 58, 2016.

[2] FERNANDES, C.H.M.; SILVA, B.F. & AQUINO, J.M. “On the performance of distinct electrochemical and solar-based advanced oxidation processes to mineralize the insecticide imidacloprid”. Chemosphere, **275**: 130010, 2021.

[3] SÁNCHEZ-MONTES, I.; SALMERÓN GARCÍA, I.; RIVAS IBAÑEZ, G.; AQUINO, J.M.; POLO-LÓPEZ, M.I.; MALATO, S. & OLLER, I. “UVC-based advanced oxidation processes for simultaneous removal of microcontaminants and pathogens from simulated municipal wastewater at pilot plant scale”. Environ. Sci. Water Res. Technol., **6**: 2553, 2020.

[4] ZHANG, R.; VIGNESWARAN, S.; NGO, H. & NGUYEN, H. “A submerged membrane hybrid system coupled with magnetic ion exchange (MIEX®) and flocculation in wastewater treatment”. Desalination, **216**: 325, 2007.

[5] EATON, A.D. & GREENBERG, A.E. "Standard Methods for the Examination of Water and Wastewater". 20th ed., Maryland, USA, n.d.

[6] NÚÑEZ-DE LA ROSA, Y.; DURANGO, L.G.C.; FORIM, M.R.; NASCIMENTO, O.R.; HAMMER, P. &. AQUINO, J.M. “Unraveling the time evolution and post mortem changes of nanometric MnOOH during in situ oxidation of ciprofloxacin by activated peroxymonosulfate”. Appl. Catal. B Environ., **327**: 122439, 2023.

[7] ENTRADAS, T.; WALDRON, S. & VOLK, M. “The detection sensitivity of commonly used singlet oxygen probes in aqueous environments”. J. Photochem. Photobiol. B., **204**: 111787, 2020.